METHODS FOR LIGAND SCREENING

BY DISSOLUTION DNP ASSISTED NMR SPECTROSCOPY

A Dissertation

by

YAEWON KIM

Submitted to the Office of Graduate and Professional Studies of
Texas A&M University
in partial fulfillment of the requirements for the degree of

DOCTOR OF PHILOSOPHY

Chair of Committee,	Christian Hilty
Committee Members,	David Russell
	Karen Wooley
	Mary McDougall
Head of Department,	Simon North

December 2018

Major Subject: Chemistry

ABSTRACT

NMR spectroscopy is one of the front-line techniques in drug screening for binding identification and affinity determination. A critical issue that limits the scope of NMR in screening applications is low detection sensitivity. A solution can be provided by the hyperpolarization technique of dissolution dynamic nuclear polarization (D-DNP). With a several thousand-fold enhancement of NMR signals, the need for signal averaging and the problems arising due to low protein or ligand solubility can be avoided.

^{19}F-NMR relaxometry for ligand screening using D-DNP is demonstrated. With a well polarizable reporter ligand containing ^{19}F atoms, binding affinities of non-fluorinated ligands can be determined under competitive binding through transverse relaxation (T_2) measurements. The enhanced sensitivity by the D-DNP method allows lowering the protein and ligand concentrations to the micromolar to sub-micromolar range.

Despite the substantial signal enhancement by DNP, the achievable throughput is limited because the most commonly available instrumentation for D-DNP provides a single hyperpolarized sample after each polarization process. We demonstrate that multiplexed NMR detection can improve the throughput of D-DNP experiments by permitting parallelized screening experiments with a single hyperpolarized aliquot of ligand. In combination with a flow injection system capable of mixing the hyperpolarized sample with several different secondary samples, T_2 relaxation times of the reporter ligand can be obtained from multiple channels simultaneously at desired concentration ratios of the reporter to competitive ligand concentrations. This method extends the range of

binding affinity detectable in a single experiment to three orders of magnitude. It greatly reduces the chance of missing the binding detection due to non-optimal sample concentrations in every individual experiment. This multiplexed D-DNP approach may be more broadly applied to chemical or biochemical problems requiring variable-dependent measurements.

ACKNOWLEDGEMENTS

First and foremost, I would like to thank my advisor, Dr. Christian Hilty for giving me the opportunity to complete my Ph.D. dissertation under his supervision. His enthusiasm for research and not to mention his expertise in the field of NMR spectroscopy inspired me all the time. None of my accomplishments would have been possible without his patience, helpful suggestions, and those of numerous days that he stayed late in the lab for me to solve problems.

I would like to address my full respect and gratitude for my committee members, Dr. David Russell, Dr. Karen Wooley, and Dr. Mary McDougall for their guidance and support throughout the course of this work. I also wish to thank Dr. Wenshe Liu for his willingness to act as a substitute committee member.

I would like to thank Hilty group members. I was grateful to have discussions with these talented people. I am especially thankful to Mengxiao Liu for collaborations on the multi-channel NMR project. Thanks also go to Jihyun Kim and Dr. Youngbok Lee for taking their time on numerous discussions and supporting on my project.

Additionally, I cannot forget to thank my friends I met in College Station for their encouragement and prayers that helped me stay positive during the tough times.

I would I like to thank Dr. Hangil Lee, my undergraduate academic advisor for his encouragement to pursue my dreams.

Last but not least, I would like to thank my family for being there for me and supporting me in both good times and bad.

NOMENCLATURE

1D	One Dimensional
2D	Two Dimensional
BBO	Broadband Observe
CSA	Chemical Shift Anisotropy
CPMG	Carr-Purcell Meiboom-Gill
D-DNP	Dissolution Dynamic Nuclear Polarization
DMSO	DiMethyl SulfOxide
DNP	Dynamic Nuclear Polarization
ESR	Electron Paramagnetic Resonance
n-FABS	n-Fluorinated Atoms for Biochemical Screening
FAXS	Fluorine chemical shift Anisotropy and eXchange for Screening
FBDD	Fragment Based Drug Discovery
FID	Free Induction Decay
HTS	High Throughput Screening
HSQC	Heteronuclear Single Quantum Coherence
INEPT	Insensitive Nuclear Enhanced Polarization Transfer
INPHARMA	Interligand Noes for PHARmacophore Mapping
MRI	Magnetic Resonance Imaging
MW	MicroWave
NMR	Nuclear Magnetic Resonance
NOE	Nuclear Overhauser Effect

NOESY	Nuclear Overhauser Effect SpectroscopY
PEEK	PolyEther Ether Ketone
ppm	Parts Per Million
PRE	Paramagnetic Resonance Effect
RF	Radio Frequency
RX	Receiver
SNR	Signal to Noise Ratio
SLAPSTIC	Spin Labels Attached to Protein Side chains as a Tool to Identify interacting Compounds
STD	Saturation Transfer Difference
TINS	Target Immobilized NMR Screening
TEMPOL	4-hydroxy-(2,2,6,6-TEtraMethylPiperidin-1-yl)Oxy
TFA	TriFluoroAcetic acid
TFE	TriFluoroEthanol
TFBC	4-(TriFluoromethyl)Benzene-1-Carboximidamide
TROSY	Transverse Relaxation-Optimized SpectroscopY
UV-VIS	UltraViolet-VISible
WaterLOGSY	Water-Ligand Observed via Gradient SpectroscopY

CONTRIBUTORS AND FUNDING SOURCES

Contributors

This work was supported by a dissertation committee consisting of Dr. Christian Hilty, Dr. David Russell, and Dr. Karen Wooley of the Department of Chemistry as well as Dr. Mary McDougall of the Department of Biomedical Engineering.

The work shown in Chapters 4 and 5 was the result of collaboration with Mengxiao Liu (M.L.), a graduate student of the Department of Chemistry. M.L. developed a multi-channel NMR spectrometer used in this work. Yaewon Kim (Y.K.) fabricated a multi-channel NMR probe. M.L. and Y.K. designed and performed the experiments. Chia-Hsiu Chen (C-H.C.), a graduate student of the Department of Chemistry contributed to the design of the experiment described in Appendix B and prepared catalyst samples for the experiments. Y.K. completed all other work including data processing and analysis under the advisement of Professor Dr. Christian Hilty.

Funding Sources

TABLE OF CONTENTS

LIST OF FIGURES

LIST OF TABLES

1.   INTRODUCTION

1.1.   Drug discovery and development

The search for medicines to treat diseases dates back thousands of years, over the course of which numerous traditional medicines were found and experiences were passed down through generations.[1] The history of modern drug discovery, which is based on knowledge of the biological target, however, is not older than a half of a century.[2] Advances in analytical chemistry, molecular biology, human genomics, and other related fields have driven a remarkable progress in identifying specific macromolecular targets responsible for the disease and understanding underlying processes at a molecular level.[3] These achievements have enabled a knowledge-based approach, in which the drug discovery begins with a rational design of drugs, and which stands in contrast to the reliance on serendipity.[4]

The drug discovery and development is a lengthy and expensive process. To research and develop a new drug, it takes an average of 10 to 15 years and costs $ 1.5 billion on average.[5] This extensive process initiates with identifying a potential drug target. Once the target is chosen, two steps are followed to find ligands that elicit a medicinal effect on the target.[6] An initial screening step involves identifying compounds that show affinity to the target and then validating the presence of binding interactions. The identified compounds are often called "hits". The following step is the lead optimization, where chemical modifications are made to the structures of the hits to improve drug associated properties such as potency, specificity, selectivity, metabolic stability, and

bioavailability. The optimized compounds then become drug candidates that undergo pre-clinical and clinical trials to determine drug efficacy and safety.

There are two distinct approaches to screening for drug candidates. One is a high-throughput screening (HTS) approach where large chemical libraries of compounds (typically on the order of 10^6) with a molecular weight of 500 Da on average are screened against the target protein to detect high-affinity hits.[7] With robotic systems, the speed of HTS has been greatly accelerated, permitting to screen more than ten thousand samples per day.[8,9] Later, a complementary approach called fragment-based drug discovery (FBDD) emerged, which aims to identify weakly binding compounds of less than 300 Da molecular weight from a smaller chemical library (about 10^3 compounds). Small fragments typically have low affinities due to low molecular weight but demonstrate a high affinity per atom to the target. The fragments identified with high binding efficiency can serve as the starting compound to build a potent drug. It has been shown that screening for fragments can increase success rates for ultimately discovering strongly binding compounds, compared to HTS.[10] This advantage is in part because compounds in fragment libraries are usually more soluble than larger compounds screened by HTS, and thus FBDD is less likely to produce false results caused by low solubility or compound aggregates, that often occur in assay-based HTS screening. Also, diverse structural and functional modifications can be made on the identified fragments to tune the affinity, in contrast to the limited diversity in compound libraries for HTS.[11,12]

The first experimental demonstration of FBDD was performed with nuclear magnetic resonance (NMR) spectroscopy in 1996.[13] Nanomolar high-affinity ligands were discovered for FK506 binding protein by tethering two fragments that were identified to

bind to neighboring protein binding sites with micromolar affinities. Various analytical methods such as X-ray crystallography[14] and surface plasmon resonance[15] have been developed to adopt the fragment approach as well. NMR spectroscopy generally is still one of the most robust and reliable techniques to detect weakly binding ligands.[16] Various NMR screening methods have been developed, which rely on changes in NMR observable parameters such as chemical shift, signal intensity or spin relaxation upon ligand binding.[17,18] Methods to determine the structure of the pharmacophore have been described that are based on magnetization transfer between adjacent spins in the protein-ligand complex.[19] With the advances in the analytical techniques, the FBDD approach has become increasingly popular during the last two decades, holding promise to discover drugs for even challenging targets such as protein-protein interfaces based on better understanding on the structure of targets and ligands.[12] Two medicines have to date been successfully derived from FBDD, and dozens of compounds have entered clinical trials.[20,21]

1.2. NMR spectroscopy in drug screening

1.2.1. Equilibrium of protein-ligand interactions

Protein-ligand interactions occur by forming a protein-ligand complex under a dynamic equilibrium. These interactions are essential for biological processes to function properly. For a protein with a single binding site, the binding equilibrium can be defined as:

$$P + L \underset{k_{off}}{\overset{k_{on}}{\rightleftharpoons}} PL$$

3
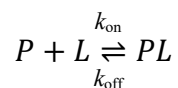
where P is a protein, L is a ligand, and PL is a protein-ligand complex. The parameters k_{on} and k_{off} are the association and dissociation rate constants, respectively. The association rate constant is mostly governed by the rate of diffusion of the ligand, typically in the range between 10^7 and 10^9 M^{-1}s^{-1}. The interaction is commonly characterized by measuring the dissociation constant, K_D:

$$K_D = \frac{[P][L]}{[PL]} = \frac{k_{off}}{k_{on}} \tag{1.1}$$

which is the ratio of equilibrium concentrations of protein and ligand to protein-ligand complex ($[P]$, $[L]$ and $[PL]$, respectively) or the ratio of k_{off} and k_{on}. Given that k_{on} is often diffusion-limited, the dissociation constant is mostly determined by k_{off}.

When the value of K_D and the total concentrations of protein and ligand ($[P]_t$ and $[L]_t$, respectively) are known, the concentration of the protein-ligand complex at equilibrium $[PL]$ can be found.[22]

$$[PL] = \frac{[L]_t + [P]_t + K_D - \sqrt{([L]_t + [P]_t + K_D)^2 - 4[L]_t[P]_t}}{2} \tag{1.2}$$

Figure 1.1 shows simulations of bound fraction of ligand ($X_b^L = [PL]/[L]_t$) and protein ($X_b^P = [PL]/[P]_t$) as a function of ligand concentration $[L]_t$ for three different K_D values. It is shown that a decrease in K_D (strongly binding ligand) generates higher X_b^L and X_b^P. In addition, X_b^L increases with decreasing $[L]_t$, while the opposite trend occurs for X_b^P. When $[L]_t = K_D$, half of the protein binding sites become occupied ($X_b^P = 0.5$).
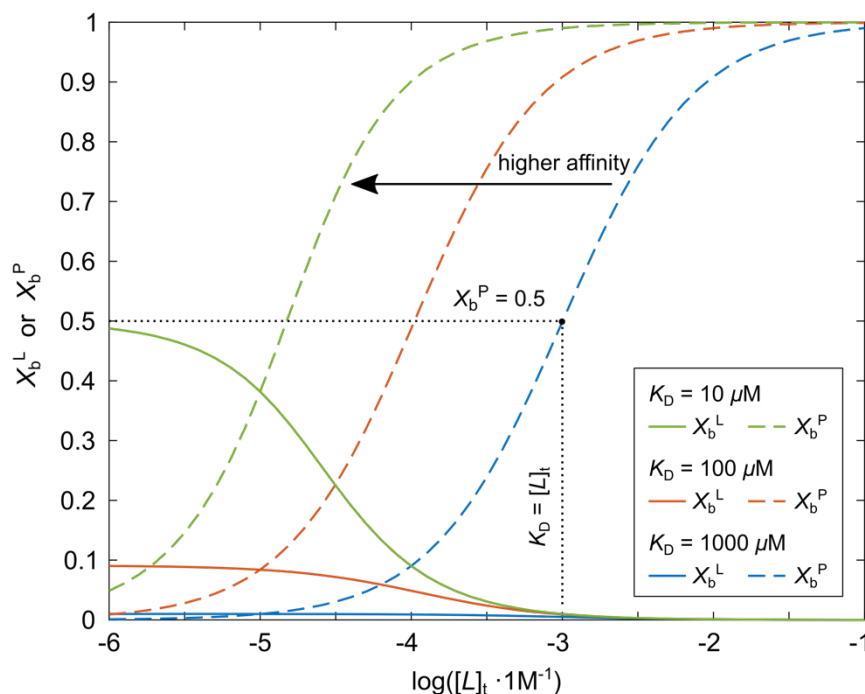
Figure 1.1: Fraction of bound ligand (X_b^L) and that of bound protein (X_b^P) as a function of the total ligand concentration $[L]_t$ for three K_D values (10, 100, and 1000 μM), calculated using Equation (1.2), are shown on a logarithmic scale. Solid and dashed lines are used to represent X_b^L and X_b^P, respectively. The protein concentration used in the calculations is $[P]_t = 10\ \mu$M.

When $[L]_t \gg K_D$, the protein binding sites are nearly saturated ($X_b^P \approx 1$), while the majority of ligand is in free form. In this context, if the detection technique for binding is based on X_b^P, such as in SPR, fluorescence-based, or protein-observed NMR methods, the measurement requires a ligand concentration comparable to its K_D in order to produce sufficiently high X_b^P. A limitation due to solubility may arise if weakly binding ligands are to be identified. In contrast, the ligand-observed NMR experiments, which rely on X_b^L, can show a larger change in observables with low ligand concentrations. This observation explains the strength of NMR spectroscopy for identifying weakly binding ligands by ligand-observed methods.

1.2.2. *Effect of ligand binding on NMR observable parameters*

Under equilibrium, ligands repeatedly bind and unbind from proteins, experiencing two environments that are magnetically distinct. This dynamic process, referred to as *chemical exchange*, gives rise to detectable changes in NMR properties such as chemical shift, spin relaxation, and line broadening. Depending on how fast the chemical exchange rate is compared to the difference in the nuclear spin precession frequencies of free and bound ligands ($\Delta v = |v_f - v_b|$), the chemical exchange can be classified into three basic regimes. For the simplest two-state model comprising free and bound ligands, the apparent association rate can be expressed as $[P]k_{on}$. The exchange rate (k_{ex}), which quantifies the average number of ligand exchange events per unit time, can thus be written as $[P]k_{on} + k_{off}$. The regime called as *slow exchange regime* is identified when k_{ex} is smaller than Δv. Tightly binding ligands fall into this category. Two resolved signals from each state appear close to v_f and v_b. Due to the slow exchange, the signals become broader as well. The linewidths of the free and bound ligands are determined by Equation (1.3):[23]

$$R_{2,obs} = R_{2,f} + [P]k_{on} = R_{2,f} + X_b{}^L k_{ex} \quad \text{(free ligand)}$$

$$(1.3)$$

$$R_{2,obs} = R_{2,b} + k_{off} = R_{2,b} + X_f{}^L k_{ex} \quad \text{(bound ligand)}$$

Here, $R_{2,f}$ and $R_{2,b}$ are the transverse relaxation rates of free and bound ligands, respectively, in the absence of exchange. These R_2 relaxation rates are the inverse of transverse relaxation time constant T_2. $R_{2,obs}$ represents the observed transverse relaxation rate, which determines the signal linewidth in the NMR spectrum (the width at half height $\Delta v_{1/2} = |R_{2,f} - R_{2,b}|/\pi$). If the populations of the two forms are highly asymmetric, it is

difficult to observe the bound ligand signal due to severe line broadening in practice. Only a sharp signal may be observed from the free ligand, which could be misinterpreted as that of a weakly binding ligand. In the *intermediate exchange regime*, k_{ex} is comparable to Δv. In this case, the two signals merge into a single peak. Under the *fast exchange regime* where k_{ex} far exceeds Δv, a sharp peak appears at a frequency $X_f^L v_f + X_b^L v_b$. This frequency is the population-weighted average of v_f and v_b. Further, if the exchange is on a faster time scale than the spin relaxation, the linewidth is determined by Equation (1.4):[24]

$$R_{2,obs} = X_f^L R_{2,f} + X_b^L R_{2,b} + X_b^L X_f^{L^2} (2\pi\Delta v)^2 / k_{off} \tag{1.4}$$

The third term in Equation (1.4) describes some amount of additional line broadening due to $k_{ex} \neq \infty$. It also indicates that this exchange contribution is field-dependent. When $X_b^L X_f^{L^2} = X_b^L (1 - X_b^L)^2 \approx X_b^L$, $R_{2,obs}$ becomes proportional to $R_{2,b}$ as described by

$$R_{2,obs} = X_f^L R_{2,f} + X_b^L (R_{2,b} + (2\pi\Delta v)^2 / k_{off}) \tag{1.5}$$

A complete description of the chemical exchange affecting the evolution of magnetization has been derived by McConnell using the modified Bloch equations. From the Bloch-McConnell equations, numerical solutions for the relaxation rate and chemical shift can be obtained.[25] In the case of $X_f^L \gg X_b^L$, the analytical expression for $R_{2,obs}$ can be simplified, which is applicable to all time regimes of chemical exchange, known as the Swift-Connick equation.[26]

$$R_{2,obs} = X_f^L R_{2,f} + X_f^L X_b^L k_{ex} \frac{R_{2,b}(R_{2,b} + X_b^L k_{ex}) + (2\pi\Delta v)^2}{(R_{2,b} + X_f^L k_{ex})^2 + (2\pi\Delta v)^2} \tag{1.6}$$

1.2.3. Overview of NMR screening methods

The methods for NMR screening can be classified into two categories depending on the NMR signals observed in the experiment: *target-detected* and *ligand-detected methods*.[22] In the following paragraphs, the different features of the two methods are described.

The target-detected methods are based on chemical shift perturbation of protein resonances induced by intermolecular interactions and chemical exchange between the protein and ligand. This approach requires isotopically labeled proteins (^{15}N or both ^{13}C and ^{15}N) to acquire two-dimensional correlation spectra such as heteronuclear single quantum coherence (HSQC) spectrum. The measurement of this type of data requires a protein concentration of 20 ~ 200 μM which is an order of magnitude higher than that typically used in the ligand-detected methods. It is most suitable for proteins with a molecular weight not larger than 30 kDa. Proteins of larger molecular weight exhibit rapid T_2 relaxation, which causes serve line broadening. This size limit has been extended to over 100 kDa by transverse relaxation-optimized spectroscopy (TROSY), where the T_2 relaxation is partially suppressed by destructive interference of dipole-dipole and chemical shift relaxation in specific molecular geometries, enabling the acquisition high-resolution correlation spectra even with larger molecules.[27,28] Despite the potentially demanding requirements on the preparation of suitable protein samples, the target-detected approach is of interest because it allows for characterizing the binding sites structurally. This information is essential for improving the binding affinity of lead compounds in the lead optimization step. If protein resonance assignments are available, the protein residues interacting with a ligand can be identified, and the accurate orientation of the bound ligand

on the protein can be determined. Even without a complete resonance assignment, limited but useful structural information can be obtained from HSQC measurements using selectively labeled proteins.[29] Another benefit of the target-detected approach is that it does not rely on fast exchange, and thus it can detect strongly binding ligands with K_D in nM.

Ligand-detected methods are generally applicable to ligands in fast exchange. These approaches often rely on one-dimensional ^{1}H and ^{19}F NMR spectra aiming at the identification of changes in ligand signal relaxation rates or chemical shifts. In contrast to the target-detected methods, there is no size limit of the target protein, as well as no requirement for isotope labeled protein. A typical concentration of protein is $5 \sim 50~\mu$M, and ligands are added at 10- to 200-fold excess to the protein. A relatively high concentration of the ligand may cause false positives occurring from non-specific interactions or false negatives for high-affinity ligands ($K_D < 1~\mu$M). These issues can be circumvented by exploiting competitive binding using a reporter ligand that weakly binds to the target protein. Apart from simple identification of binders, structural information on the pharmacophore can be obtained by utilizing intra-ligand NOEs, inter-ligand NOEs between competitive ligands, or NOEs between the protein and ligand in the presence of chemical exchange between the free and bound ligands.

1.2.4. Ligand-detected NMR screening

Ligand compounds are usually smaller than 500 Da, whereas proteins have masses greater than 10 kDa. When a ligand binds to a protein, the apparent molecular weight of the ligand increases dramatically. Binding results in a large difference in timescales for

the rotational tumbling motion of the ligand, which affects NMR relaxation. Assuming that the molecule is spherical, the correlation time for rotational motion (τ_c), which is defined as the time required for the molecule to rotate one radian, decreases linearly with increasing molecular weight. This decrease is described by Stokes-Einstein relationship. The spectral density function, describing the frequency distribution of molecular tumbling, can be used to express the measurable relaxation rates

$$J(\omega, \tau_c) = \frac{\tau_c}{1 + (\omega\tau_c)^2} \tag{1.7}$$

When frequency components match to the nuclear Larmor frequency, NMR transitions can be induced, and thus relaxation occurs. At a given τ_c, $J(0) = \tau_c$ is the maximum possible value for J. Thus, the NMR observables that depend on $J(0)$ can provide an excellent contrast upon binding. For example, the dipolar [^{1}H, ^{1}H] R_2 relaxation and cross relaxation rates fall into this category:[30]

$$R_{2,DD} = \frac{1}{20} b^2 \big(5J(0) + 9J(\omega_0) + 6J(2\omega_0)\big) \tag{1.8}$$

$$R_{cross} = \frac{1}{10} b^2 \big(J(0) - 6J(2\omega_0)\big) \tag{1.9}$$

Here, ω_0 is the Larmor frequency and $b = \mu_0 \hbar \gamma_H^2 / (4\pi r^3)$, μ_0 is the vacuum permeability, $\hbar$ is the Plank constant, γ_H is the gyromagnetic ratio of ^{1}H spins, and r is the distance between two nuclei. Free ligands which have very short correlation times ($\tau_c \omega \ll 1$), exhibit slow R_2 relaxation and negative R_{cross} which yields negative NOE cross peaks in a 2D nuclear Overhauser spectroscopy (NOESY) spectrum (the opposite sign of the diagonal peaks). In contrast, the ligands in complex with macromolecules experience long correlation times ($\tau_c \omega_0 \gg 1$). As a result, fast R_2 relaxation and positive R_{cross}, and thus

macromolecule (bound)		small molecule (free)
slow	*tumbling*	fast
slow	*diffusion*	fast
fast	T_2 *relaxation*	slow
strong negative	*NOE*	weak positive
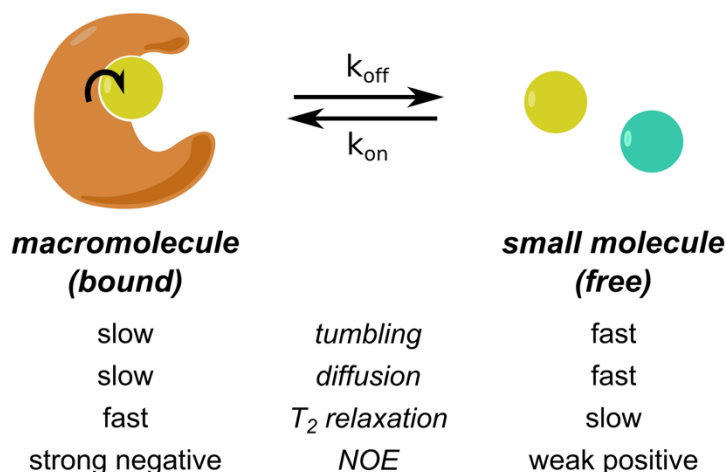
Figure 1.2: NMR properties of macromolecules and small molecules. Yellow and green balls represent a ligand of a target macromolecule and a non-interacting compound, respectively. The ligand-detected NMR methods for screening rely on a large difference in the tumbling rates of free and bound ligands, which gives rise to contrasting NMR properties.

positive NOE cross peaks can be observed. Figure 1.2 summarizes the difference in NMR observables between small molecules and macromolecules. Various types of ligand-detected experiments have been developed utilizing this difference. The following paragraphs describe the experiments that are commonly carried out in drug screening, exploiting the relaxation-based and magnetization transfer-based methods. The former specifically include ^{19}F-R_2 methods, which are discussed separately to emphasize the advantages of using ^{19}F NMR for screening.

Relaxation-based methods

The transverse magnetization decays because of a loss of phase coherence caused by dipolar and chemical shift anisotropy (CSA) interactions, and the rate of the decay is called the R_2 relaxation rate. The decoherence of the magnetization can also occur by

magnetic field inhomogeneity. This external contribution can be eliminated by creating spin echoes. The intrinsic R_2 can be obtained by measuring the intensity decay of multiple echoes over time. Carr Purcell Meiboom Gill (CPMG)[31] pulse sequences for generating spin echoes consist of $p1 - [\tau - p2 - \tau]_{x\,n}$. The first RF pulse (p1) is a $\pi/2$ pulse with pulse x, and the following p2 is a refocusing π pulse with phase y. A spin echo is produced during the delays 2τ. The rate of R_2 relaxation can be determined from an exponential fit to the intensities from the spin echoes.

Ligand binding can be identified from a difference in the measured R_2 rates or linewidths of ligand signals with and without introducing a target. Further, the thermodynamic dissociation constant (K_D) can be determined by titration experiments as a function of ligand or protein concentration, with the use of Equations (1.2) and (1.5). While not often required for ligand screening, kinetics of chemical exchange in the protein-ligand interactions can further be obtained from the R_2 relaxation dispersion measurements.[32–34] When Δv is not negligibly small compared to k_{ex}, the R_2 relaxation rates are modulated by the delay between the two consecutive π pulses (τ_{cp}) in the CPMG pulse scheme. The R_2 dependence on τ_{cp} can be explicitly described by Equation (1.10):[32,35]

$$R_{2,obs}^{CPMG} = p_f R_{2,f} + p_b\left(1/R_{2,b} + \tau_b\right) + p_b p_f \tau_b \Delta\omega^2 \left(1 - \frac{2\tau_b \tanh\left(\tau_{cp}/(2\tau_b)\right)}{\tau_{cp}}\right) \quad (1.10)$$

where p_f and p_b are the fraction of free and bound ligands, respectively, and $\tau_b = 1/k_{ex}$ is the lifetime of the protein-ligand complex.

There are several strategies to amplify the contrast between the R_2 relaxation rates of free and bound ligands. By these strategies, the detection sensitivity for binding can be

improved, and the required amount of protein for measurements can be reduced. A method called spin labels attached to protein side chains as a tool to identify interacting compounds (SLAPSTIC)[36] is based on a paramagnetic relaxation enhancement (PRE) effect that causes a significant increase in R_2 relaxation rates of the ligand signals due to dipolar interactions between the unpaired electrons and the nucleus. To exploit the PRE effect, a spin-label or a paramagnetic metal ion is bound to protein near the ligand binding site. This method has been used for searching ligands that bind to a second binding site nearby the primary site.[37] Additionally, distances between the atoms of interest can be evaluated utilizing the distance dependence of the PRE. An enhancement of R_2 contrast can be also achieved by immobilizing the protein on a solid support and screening for ligands with a flow-NMR technique. This method, known as target immobilized NMR screening (TINS),[38] additionally reduces the overall protein consumption for high-throughput measurements. Finally, the use of long-lived spin states has been proposed for increasing the sensitivity of observable relaxation parameters to binding.[39]

NOE-based methods

Examples of the most commonly used NOE-based screening methods are saturation transfer difference (STD),[40] water-ligand observed via gradient spectroscopy (WaterLOGSY),[41] transferred NOE,[42] interligand NOEs for pharmacophore mapping (INPHARMA).[43] The STD experiment exploits the magnetization transfer from the pre-saturated proton spins of protein to those of bound ligand. The protein proton spins can be saturated by selectively irradiating at a frequency where only the protein resonances are present. The saturation propagates to the entire protein by spin diffusion. If the ligand is

in fast exchange, the intensity of the ligand signal becomes attenuated due to the transfer of saturated proton magnetization of protein by dipole-dipole interactions, which distinguishes the binders from non-binders. The STD method can also be used to determine binding epitope structures by measuring the saturation time dependence of signal buildup. In the WaterLOGSY experiment, water protons are used as a source of magnetization transfer to the ligand. A difference in the tumbling rates of water in bulk and in the binding pocket gives rise to opposite signs of the NOE cross peaks for binders and non-binders. The binders experience a strong negative NOE, resulting in positive NMR signals (conventionally, the initial water magnetization is negative). Multiple ways are possible for the water magnetization to be transferred to the protein; It can be achieved through exchanging labile protons of protein with water protons, intermolecular NOE, and spin diffusion. When compared to the STD experiment, these transfer pathways make this method especially efficient for target proteins that have a low proton density such as RNA. In the transferred-NOE experiment, intra-ligand NOEs are measured. The NOE signals from a proton pair of a ligand yield opposite signs in free and bound forms. Based on the changes of NOE signal at varying NOE mixing time, conformational information of the bound ligand can be obtained, which is necessary for optimizing the lead properties. When NOEs between protein and ligand are measured, the contact sites in a protein-ligand complex can be identified as well. The INPHARMA experiment involves a two-step polarization transfer from one ligand to another competing ligand, mediated by the protein protons. When the orientation of one ligand in the binding site is known, this method allows mapping the binding epitope for the second ligand. The NOE methods described here and others allow for obtaining structural information without measuring protein

resonances as well as binding identification, long experimental time is required because the intensity of NOE signals is typically below 10% of the source peak intensity.

^{19}F R_2-based methods

A dominant contribution from CSA to the R_2 relaxation of ^{19}F nuclei provides a highly sensitive method for the ligand binding. The CSA-dominated R_2 relaxation gives rise to a dramatically increased R_2 relaxation rate of the bound form, allowing for detecting even weaker affinity ligands and with a small bound fraction of ligands (less than 1%). ^{19}F NMR provides a detection sensitivity comparable to that of protons (83% of proton sensitivity) since the natural abundance of the ^{19}F isotope is 100 % and the gyromagnetic ratio close to that of ^{1}H. Other than ^{1}H NMR, ^{19}F detection is free of background signals from typical solvents or biological molecules, and thus no solvent suppression is required. A large chemical shift dispersion of ^{19}F over 300 ppm minimizes signal overlap, allowing for testing multiple compounds simultaneously. Non-fluorinated ligands can be screened indirectly with ^{19}F detection, by competitive binding using an appropriate fluorinated reporter ligand. This method, referred to as fluorine chemical shift anisotropy and exchange for screening (FAXS), was first demonstrated by Dalvit *et al.*[44] It requires a suitable reporter ligand that is in fast exchange and preferably includes -CF$_3$ functional group for high sensitivity. The binding of a non-fluorinated ligand can be detected by the decrease in the R_2 relaxation rate or restoration of the signal intensity of the reporter ligand under binding competition due to a (partial) displacement of bound reporter ligand by the ligand of interest. ^{19}F NMR can also be used for an enzymatic activity assay by competition with a -CF$_3$ tagged known substrate of the target protein. The activity towards

this known substrate is measured in the absence and presence of ligand under investigation. This method, reported as n-fluorinated atoms for biochemical screening (n-FABS) by Dalvit *et al*, effectively identifies a ligand that binds to the active site of the target protein by observing for distinct -CF$_3$ signals from the substrate and the product.[45]

1.3. NMR sensitivity

A critical issue that limits the scope of NMR in drug screening applications is an intrinsically low detection sensitivity. The NMR signal intensity in part is determined by nuclear spin polarization, *i.e.*, the relative population difference of Zeeman levels. For a spin ½ system such as ^{1}H, ^{19}F, and ^{13}C, two Zeeman energy levels are generated in a magnetic field corresponding to the nuclear spin states defined as $|\alpha\rangle$ = ½ and $|\beta\rangle$ = - ½. The α state, where the magnetic moments of nuclear spins align parallel to the applied magnetic field, is lower in energy than the β state by

$$\Delta E = \hbar \gamma B_0 \qquad (1.11)$$

Here, $\hbar$ is a Plank constant, γ is the gyromagnetic ratio, and B_0 is the magnetic field strength. Thus, the nuclear spin polarization is calculated as

$$P = \frac{n_\alpha - n_\beta}{n_\alpha + n_\beta} = \frac{1 - e^{-\Delta E/kT}}{1 + e^{-\Delta E/kT}} = tanh\left(\frac{\gamma \hbar B_0}{2k_B T}\right) \qquad (1.12)$$

where n_α and n_β are the number of spins in the α and β states, respectively, k_B is Boltzmann's constant, and T is the temperature in Kelvin. The equation indicates that the spin polarization is dependent on the type of nucleus through its dependence on γ, and increases with increasing B_0 and decreasing T. In Figure 1.3, the spin polarization of electron spins is plotted along with that of ^{1}H and ^{13}C nuclei as a function of T. At T = 300
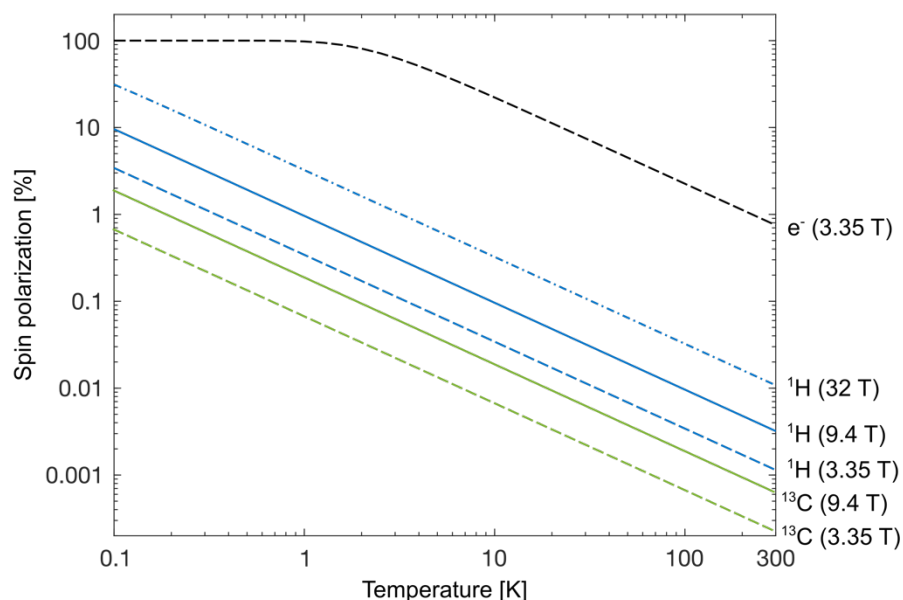
Figure 1.3: Spin polarization levels calculated for electron (e⁻), proton (^{1}H) and carbon (^{13}C) as a function of temperature at different magnetic fields (3.35, 9.4, and 32 T) using Equation (1.12).

K and $B_0 = 9.4$ T (corresponding to a ^{1}H Larmor frequency of 400 MHz), the polarization is only 0.003% for proton, the nucleus with the highest γ among common NMR nuclei. Under the same condition, ^{13}C nuclei attain about one-fourth of the ^{1}H spin polarization. By increasing B_0 to from 9.4 to 32 T, the world's most powerful superconducting magnet for NMR currently,[46] or by decreasing the temperature to 100 K, a 3-fold increase (~ 0.01%) in ^{1}H spin polarization can be achieved. In contrast, the electron spin gives rise to 1% of spin polarization even at $B_0 = 3.35$ T and $T = 300$ K. This difference is because the gyromagnetic ratio of electrons is 660 times larger than that of protons.

Over the past few decades, remarkable technological advances have been made to increase the NMR signal as well as to reduce noise, which improves the overall detection sensitivity described by the signal-to-noise ratio (SNR). The parameters related to the

signal intensity include the static magnetic field strength (B_0), the gyromagnetic ratio of excited and detected nuclei (γ_e and γ_n, respectively), the number of observed nuclei in the sample (n), and a factor dependent on a coil design (K). Those associated with the noise include $T_{N,probe}$ and $T_{N,preamp}$ which are the temperature of probe (referring to RF coil and sample) and preamplifier, respectively, and Δf is the receiver bandwidth. The effect of these parameters on the SNR is described as[47,48]

$$\frac{S}{N} \propto \frac{n\gamma_e K \sqrt{B_0{}^3 \gamma_d{}^5}}{\sqrt{4k(\Delta f)\left(T_{N,probe} + T_{N,preamp}\right)}} \tag{1.13}$$

As the equation indicates, the SNR increases proportionally to $B_0{}^{\frac{3}{2}}$. Compared to the first commercial 30 MHz NMR spectrometer in the 1950's,[49] the magnetic field has been increased by almost 50 times with the advance in superconducting magnet technology. Besides the increased sensitivity, a stronger magnetic field provides a higher spectral resolution. In addition to magnet technology, other methods have been developed to increase the SNR. Several NMR pulse schemes have been devised to increase the sensitivity for detecting low γ spins such as ^{13}C and ^{15}N by transferring polarization from a high γ spin, ^1H. Using this method, the intensity of ^{13}C signal can be enhanced by 4 times ($\gamma_H/\gamma_C \sim 4$).[50] The transferred polarization can be reverted back to ^1H spin for detection as well.[51] The geometry of the RF coil can affect the signal intensity. For example, the sensitivity of a solenoidal coil is known to be more than 3 times higher than a saddle coil which is used for conventional NMR tubes. The high sensitivity of the solenoidal coil is due to a large filling factor (related to the closeness between the coil and the sample) and a quality factor.[47,52] At a constant length-to-diameter ratio, solenoidal coils with a smaller

diameter deliver higher the mass sensitivity (SNR per unit sample volume),[53] which is the basis of high-resolution microcoil NMR spectroscopy that is useful for mass-limited samples.[54–56] Isotope labeling techniques have allowed increasing n, which is in general required for measuring high-resolution NMR spectra of biological macromolecules.[57,58]

The major contributing factor to the noise is thermal noise from the detector circuits as shown in Equation (1.13). NMR cryoprobe technologies have made it possible to increase the SNR by 4 times compared to a room temperature probe by cooling the electronic circuits and preamplifiers to ~ 20 K with a flow of He gas while keeping the samples at room temperature.[59]

Largest improvements of signals have been achieved by "hyper" polarizing nuclear spins. A variety of methods have been developed to prepare hyperpolarized nuclear spin states through dynamic nuclear polarization (DNP) by electron spins,[60–62] optical excitation of electronic transitions,[63–66] and enrichment of parahydrogen at low temperature.[67,68] Among hyperpolarization techniques, dissolution dynamic nuclear polarization (D-DNP) can enhance NMR signals by 10^3~10^4 times in liquids, making it well suited for studying biological molecules and interactions. Hyperpolarization by DNP is based on the transfer of a high electron spin polarization to nuclear spins via hyperfine coupling. This transfer occurs by microwave irradiation near the electron resonance frequency in a magnetic field. In the D-DNP method, hyperpolarized nuclear spin states are prepared at low temperature (~1 K) while NMR measurements are performed in the liquid state by dissolving a frozen, hyperpolarized sample pellet with a superheated solvent in a fraction of a second. Three mechanisms are involved in the DNP process in solids; the solid effect, the cross effect, and thermal mixing.[69–73] The solid effect is

explained by a hyperfine coupled electron and nuclear spin pair that results in mixing of nuclear spin states, and thus allowing formally forbidden electron-nuclear transitions upon microwave irradiation at $\omega_e \pm \omega_n$, where ω_e is the electron resonance frequency and ω_n is the nuclear resonance frequency. The cross effect is based on a coupled electron-electron-nuclear spin system where the polarization transfer can occur when the resonance frequencies of two dipolar coupled electrons are separated by the value of ω_n. When the linewidth of EPR signal at half height (δ) is comparable to or larger than ω_n, the polarization transfer can occur by microwave irradiation at $\omega_e \pm \delta$ via thermal mixing. Since the first demonstration of the D-DNP method by Ardenkjær-Larsen in 2003,[74] it has been applied to the field of in *vivo* metabolic imaging[75] as well as in high-resolution NMR spectroscopy.[76] Among the latter applications, D-DNP NMR has been proposed for kinetic studies of chemical and biochemical reactions by measuring NMR signals from reactants and products in real-time.[77–79] Transient signals such as those from reaction intermediates have been also detected in diverse reactions, which has permitted to gain insights into the reaction mechanisms.[80–83] Several pulse schemes have been developed as well to characterize a transient signal that appears in hyperpolarized NMR spectra.[77,80,81,84] One of them that utilizes a continuous saturation method to follow the passage of the selected atom during the measurement of real-time D-DNP NMR has been developed in this thesis and described in Appendix C. Also, the D-DNP method has been successfully applied for characterizing protein-solvent interactions[85–87] and protein-ligand interactions with hyperpolarized small molecules[88–92] and water[93] to investigate binding affinity as well as binding epitope.

2.   DISSOLUTION DNP NMR EXPERIMENTS AND

HYPERPOLARIZATION OF ^{19}F

2.1.   Experimental procedures for D-DNP NMR experiments

Figure 2.1 illustrates a general procedure for carrying out D-DNP NMR experiments. The sequence of the experiment is listed in the caption. In the following, each step is described from a practical point of view for performing ligand-detected NMR screening experiments, although most parts apply to other types of experiments as well.
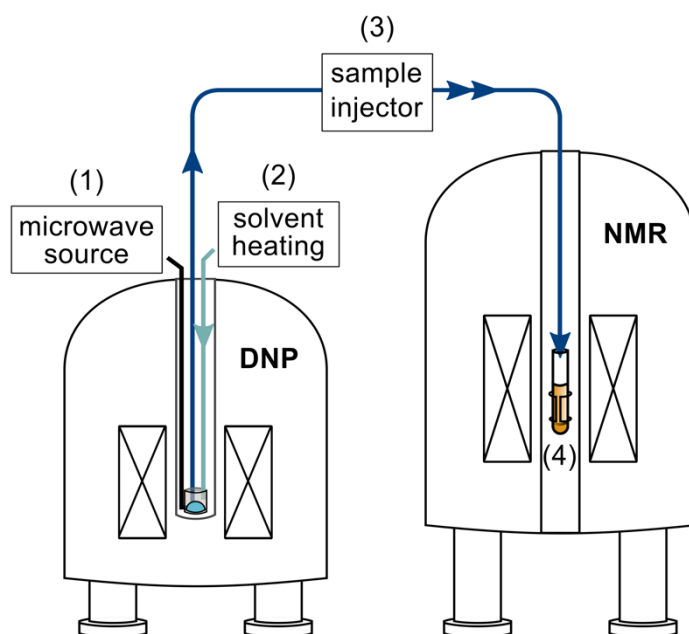
Figure 2.1: Schematic of experimental setup for D-DNP NMR experiments. The numbering indicates the order of procedures for conducting the experiments. (1) creating hyperpolarization by microwave irradiation to a sample prepared with radical in glassy matrix at ~1 K; (2) heating a dissolution solvent to quickly thaw the frozen, hyperpolarized sample; (3) injecting the sample into the NMR spectrometer by means of pressurized gas using a rapid sample injector and mixing the hyperpolarized sample with a preloaded solution of a second reagent (for example protein); followed by (4) NMR measurements.

2.1.1. Hyperpolarization

The required components of a sample for hyperpolarization include a ligand (analyte), a free radical, and a matrix, typically a liquid at room temperature, which forms an amorphous glass when frozen at $\sim$ 1 K. When choosing a ligand, the spin-lattice relaxation time (T_1) of the target nucleus in the molecule should be considered. This relaxation property is important because the hyperpolarization decays at a rate governed by T_1 during the sample transfer from a DNP polarizer to an NMR spectrometer for the measurement. Typically, molecules with low molecular weight (< 300 Da) have long T_1 of several seconds and show highest signal enhancement after dissolution. The radical is the source of electrons required for the DNP process. Multiple nitroxyl-based radicals have been reported for polarizing ^{1}H and ^{19}F nuclei, and among those 4-hydroxy-2,2,6,6-tetramethylpiperidine-1-oxyl (TEMPOL) is the most frequently used for preparing an aqueous solution.[94] The concentration of radial is typically between 15 $\sim$ 30 mM for optimal polarization enhancement.[95] A high radical concentration results in faster polarization buildup with a lower plateau and the loss of polarization during the sample transfer can be more severe. To avoid the latter problem, several different methods to remove the radical in the dissolved hyperpolarized sample have been described.[96–101] The stock solutions of ligand and radical should be prepared in the glassy matrix to disperse the radicals homogenously, enabling an efficient hyperfine coupling between the free electrons and nuclei. Possible solvents for water-soluble samples polarized with TEMPOL are D_2O/dimethyl sulfoxide-d_6 (DMSO-d_6) (v/v 1:1, 3:2), D_2O/glycerol-d_8 (v/v 1:1, 2:1) and D_2O/ethanol-d_6 (v/v 2:1). The prepared sample needs to be sonicated to remove any residual gas that may interfere with forming a glass. An aliquot of the prepared sample is

then loaded into a DNP polarizer. The volume of the loaded sample can range over 0.1 ~ 100 μL. With the sample injection procedure described below, smaller loaded volumes typically result in a higher percentage of the total substance to be injected into the NMR active volume, whereas larger samples result in a higher overall concentration.[102]

The microwave source is enabled after loading of the sample into the DNP polarizer. Parameters such as microwave frequency and power or polarization time depend on the type of radical and nucleus. The optimal values for the parameters can be determined by measuring the microwave frequency dependence and time dependence of NMR signal in the solid state, also known as a solid-state microwave sweep and polarization build-up curve, respectively.

2.1.2. Sample dissolution

For dissolution, a buffer solution (about 4 mL) is heated up to > 100°C in a closed vessel until a vapor pressure on the order of 10 bar is achieved (Figure 2.1(2))With a burst of the heated water or buffer, the frozen, hyperpolarized sample is then quickly brought to the liquid state, while preserving the polarization. Some buffer components may precipitate upon heating, in which case they should be avoided.

2.1.3. Sample transfer and mixing

The dissolved hyperpolarized sample is subsequently transferred into the NMR tube through a thin Teflon tubing. Some loss of hyperpolarization is inevitable during this time. It is critical to delivering the sample with hyperpolarized ^{1}H or ^{19}F nuclei as rapidly as possible into the NMR spectrometer since its T_1 relaxation time is typically on the order

of seconds. In order to minimize polarization loss, the sample transfer can be assisted with an additional sample injector, which can drive the sample by pressurized N_2 or Ar gas and complete the transfer within $1 \sim 2$ s. As most of the hyperpolarized sample is dissolved in the front end of the stream, the first $\sim 400~\mu L$ of the dissolved sample exiting from the DNP polarizer is injected into the NMR tube. For ligand screening experiments, a protein solution should be preloaded into the NMR tube placed in the NMR spectrometer before the dissolution process starts. An aliquot of $25 \sim 50~\mu L$ protein solution is typically loaded in a 5 mm NMR tube, corresponding to approximately $1/20 \sim 1/10$ of the final volume after the hyperpolarized sample is injected. The concentration of the preloaded protein solution needs to be adjusted based on the sample dilution during mixing. For quantitative and reproducible measurements, it is important that the hyperpolarized and non-hyperpolarized samples are mixed homogeneously inside the NMR tube through turbulent mixing.

Instead of using a standard 5 mm NMR probe, it is also possible to use a flow-NMR probe to increase a throughput for NMR screening, in which a multiplexing NMR probe and spectrometer are necessary.[103] By means of a liquid-driven injection using pressurized water, the time efficiency of D-DNP experiments can be improved.[104] In Figure 2.2, an exemplary schematic of liquid-driven sample transfer that enables to admix the hyperpolarized sample and the second reagent either (a) before or (b) after splitting the stream of dissolved hyperpolarized sample into two sub-streams. The flow is stopped, as soon as the sample mixtures arrive in the sample cells inside the flow-NMR probe. These configurations have been developed in this dissertation. The configuration (a) has been used for multiplexed ligand screening experiments, described in detail later in Chapters 4

and 5. The configuration (b) can be used in experiments where independent measurements are desired in different channels.[105] Apart from the possibility of multiplexing, the use of flow injection can be beneficial if one desires to increase the ratio of the second reagent in the sample mixture. Also, residual fluid motions can be suppressed during the NMR measurement. One challenge that may be of concern using this method is that it is inconvenient to retrieve the samples from the cells without further dilution, should they be needed for further analysis.
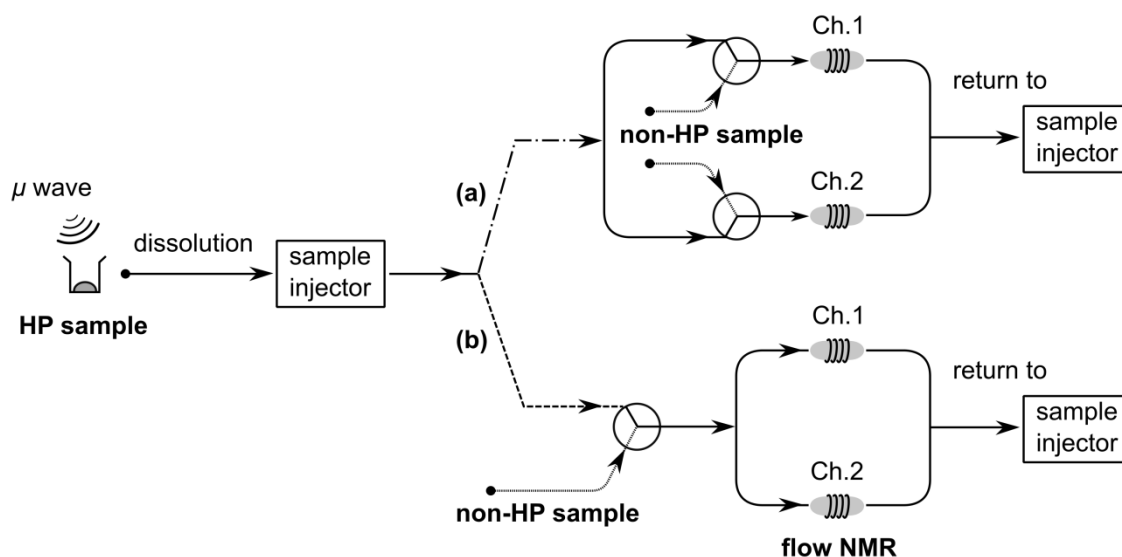
Figure 2.2: Schematic of liquid-driven sample transfer for dual-channel NMR measurements. Either path (a) or (b) can be utilized depending on the experimental design. For example, the path (a) enables to split the hyperpolarized (HP) sample into two streams and mix each stream with a different non-HP sample, allowing for sample-dependent measurements. The path (b) enables to mix the HP sample with non-HP sample first and split it into two streams. As the samples injected into two channels are equivalent, two independent NMR measurements can be performed.

2.1.4. NMR measurements

A desired NMR pulse program should be started before the sample transfer and set to wait for a trigger from the dissolution apparatus. An extra time delay of several hundreds of milliseconds may be used to allow the injected sample to settle before the NMR measurement starts. This time delay should be long enough for the protein and ligand to reach kinetic equilibrium, but not too long to cause a significant loss of polarization. The temperature of the NMR spectrometer should be set to that of the injected solution inside the NMR tube to avoid a temperature change during the NMR measurements. The temperature of the injected solution can be adjusted within limits by optimizing the temperature of the originally heated dissolution solvent. The final temperature should be determined with a thermocouple or other suitable means.

2.1.5. Technical advances in D-DNP NMR experiments

A major shortcoming of D-DNP experiment is that the hyperpolarization cannot be renewed or preserved once the sample is ejected from the polarizer, which limits the time available for NMR measurements. To increase the signal intensity, several techniques have been devised that include a rapid sample injection using high-pressure gas,[102,106,107] a magnetic tunnel over long distances,[108] a radical-free hyperpolarized sample using a radical scavenger,[96] filterable radicals,[97–99] or photo-induced radical,[100,101] and others. In addition, efforts have been made to develop pulse sequences that permit 2D or pseudo-2D NMR spectroscopy within the allowed time, such as sequential 2D NMR,[109] ultrafast COSY/HSQC NMR,[110] ultrafast D-T_2 correlation,[111] and off-resonance decoupling experiments.[112]

Hyperpolarization of low γ nuclei such as ^{13}C or ^{15}N is favored for D-DNP experiments because of their long T_1 relaxation times relative to those of ^{1}H or ^{19}F. However, it comes at the price of long polarization times typically on the order of hours. Different methods have been developed to improve the time efficiency of the DNP process, increasing the throughput for multiple measurements. Those include simultaneous polarization of multiple samples,[113,114] enlargements of sample volume for polarization,[115] and simultaneous NMR measurements from a single hyperpolarized sample aliquot.[116] A cross-polarization method has been also developed, which reduces polarization times for low γ nuclei such as ^{13}C. This method exploits short polarization times for protons. Hyperpolarization is first generated on ^{1}H, followed by polarization transfer to the low γ nuclei under Hartmann-Hahn conditions.[117–119]

2.2.   Solid-state polarization of ^{19}F

2.2.1. Introduction

Dynamic nuclear polarization (DNP) exploits a high polarization of electron spins at low temperature (almost unity at ~ 1 K) to polarize nuclear spins. The nuclear spin polarization can be enhanced when electron spin transition is saturated by microwave irradiation. The hyperpolarization by DNP can be generated on almost any type of molecule and nuclei. A number of nuclei have been successfully hyperpolarized by DNP including ^{1}H, ^{2}H, ^{6}Li/^{7}Li, ^{13}C, ^{15}N, ^{19}F, ^{29}Si, ^{31}P, ^{89}Y, and ^{107}Ag/^{109}Ag.[120–123] The DNP efficiency is often described by two factors, the maximum achievable polarization and the polarization build-up time constant. These performances are not only dependent on the target nuclei but also the electron spin resonance (ESR) properties of free electrons which

are provided by free radicals in most DNP experiments. Thus, several systematic studies have been performed both theoretically and experimentally to understand the effect of radical properties on DNP efficiency and underlying DNP mechanisms,[124–126] which help develop an optimized radical or a method for improving the DNP efficiency. For example, various biradicals have been developed with a precisely tuned orientation of the two electrons to achieve large enhancements in high field DNP (> 5 T) where the DNP efficiency is highly governed by dipolar coupling of electrons.[127,128] It has been reported that deuteration of the glassy matrix can result in a larger signal enhancement from ^{1}H and ^{13}C hyperpolarization when the radical has a broad linewidth of ESR signal such as and nitroxide radicals TEMPO (2,2,6,6-tetramethyl-1-piperdinyloxy) and 4-oxo-TEMPO.[121,126] The opposite result has been obtained using radicals with a sharp EPR signal such as trityl OX063[129] ((tris-(8-carboxyl-2,2,6,6-tetrakis(2-hydroxyethyl)-1,3,5,7-tetrathia-2,6-dihydro-s-indacene-4-yl)methyl sodium salt) and BDPA[130] (α,γ-bisdiphenylene-β-phenylallyl).[126] The radical concentration affording the highest polarization has been examined that it is typically in a range of 20 ~ 40 mM.[95,121] A majority of these previous studies have focused on ^{13}C and ^{1}H polarization as these nuclei are the most frequently detected in NMR measurements.

Hyperpolarization of ^{19}F has not been exploited much so far despite the advantages of ^{19}F NMR in general for biological applications. Thus, no literature is yet available that describes the efficiency of ^{19}F DNP in different experimental conditions. Since ^{19}F nuclei have a similar Larmor frequency as ^{1}H, the experiments have been performed using the same experimental parameters typically used for ^{1}H hyperpolarization. Here, hyperpolarization of ^{19}F with TEMPOL (4-hydroxy-TEMPO) has been performed to

examine the dependence of polarization time on substrate concentration. TEMPOL was chosen for this experiment since it has high aqueous solubility and compatibility with biological compounds, which makes it suitable for biological applications. The results obtained in these experiments provide experimental parameter values for efficient ^{19}F polarization with TEMPOL radical for further applications with ^{19}F-DNP NMR spectroscopy.

2.2.2. Materials and methods

The sample used for the measurement of microwave frequency dependence was 25 μL 0.1 M trifluoroacetic acid (TFA) with 15 mM TEMPOL, prepared in D$_2$O/DMSO-d$_6$ (v/v 1:1). The samples prepared to observe the dependence of polarization time were 25 μL of 1, 0.1, and 0.05 M trifluoroethanol (TFE) with 30 mM TEMPOL in D$_2$O/DMSO-d$_6$ (v/v 1:1).

The measurements were performed by using a home-built NMR probe that fits into the insert of a HyperSense DNP polarizer (Oxford Instruments, Abingdon, U.K.). The probe body consisted of a stainless-steel tube attached to a coaxial cable (UT-085B-SS, Microcoax) that extended from an RF port at the top of the probe to a solenoidal RF coil at the bottom. For the coil, a bare copper wire of 0.812 mm diameter was used. The coil was wound along threads made on the surface of a sample chamber. The sample chamber, containing a volume of ~ 40 µL, was constructed of polyether ether ketone (PEEK). The resonance frequency of the coil was pre-tuned to the ^{19}F NMR frequency at 3.35 T by using a fixed capacitor (1000 pF) attached to the coil lead in series. Fine frequency adjustments were performed outside of the probe using a remote tuning circuit[131]

consisting of variable tuning and matching capacitors. Double-shielded flexible coaxial cables were used to connect the remote tuning circuit to the probe, and to a spectrometer console (Bruker Biospin, Billerica, MA).

The microwave frequency dependence of DNP was measured by sequentially acquiring NMR signals after 1 min of microwave irradiation at a frequency specified in a frequency list (93.71 GHz ~ 94.31 GHz with an interval of 0.015 GHz) at temperature of 1.4 K. A residual signal from the prior scan was removed by applying multiple pulses in series (see Figure 2.3a).

For solid-state polarization build-up measurements, a series of small flip angle pulses (5° flip angle) were used to acquire NMR signals with an acquisition delay of 1 min during microwave irradiation at the optimal microwave frequency for positive enhancement (94.01 GHz) with 100 mW at 1.4 K (see Figure 2.3b). The same
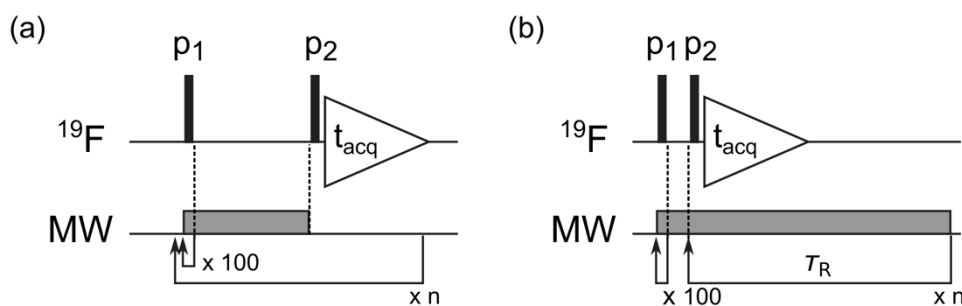
Figure 2.3: (a) Pulse sequence for measuring microwave (MW) sweep. p1 and p2 are small flip angle RF pulses (both 38°) applied to ^{19}F nuclei. The former is for destroying the residual magnetization and the latter is for signal detection. A list of n different MW frequencies is required. After 1 min of microwave irradiation, the p2 pulse is applied and a FID is acquired. As a loop repeats, a subsequent MW frequency in the list is applied. (b) Pulse sequence for measuring polarization build-up curve. The p1 and p2 pulses (38° and 5°, respectively) are used for the same purpose as described in (a). The measurements repeat n times with an acquisition delay of 1 min, which is denoted as τ_R. The pulse flip angles are based on the pulse strength $\gamma B_1/(2\pi) = 35$ kHz.

measurements were conducted without hyperpolarization to measure the polarization build-up at thermal condition. Polarization build-up signals from the background were measured without loading any sample into the sample chamber. Three repetitions were performed for all measurements. The probe was removed from the magnet of the DNP polarizer between the experiments in order to eliminate residual hyperpolarization from ^{1}H nuclei, which can be polarized at the same time.

From the polarization build-up curves, the polarization build-up time constant (τ_b) and the maximum intensity (I_M) were found by fitting the measured intensities to Equation (2.1):[132]

$$I(n) = I_M \left(1 - e^{-\tau_R/\tau_b}\right) \left(\frac{1 - \cos^n(\alpha)\, e^{-n\tau_R/\tau_b}}{1 - \cos(\alpha)\, e^{-\tau_R/\tau_b}}\right) \tag{2.1}$$

Here, $I(n)$ is the intensity of the nth scan, α is the pulse flip angle used for detection, and τ_R is the acquisition delay. This equation accounts for the signal loss by the RF pulses applied.

2.2.3. ^{19}F microwave sweep

The microwave frequency profile of DNP for was measured for the free radical TEMPOL used to hyperpolarize ^{19}F nuclei. As shown in Figure 2.4, the NMR signal was maximally positive at a microwave frequency of 94.01 GHz, and thus it was determined as the optimal microwave frequency for positive enhancement. The minimally negative NMR signal was observed at the edge of the attainable frequency range, near 94.30 GHz. This frequency could be used for achieving negative hyperpolarization. The difference between the two peak frequencies is ~290 MHz which is more than 2 times larger than the
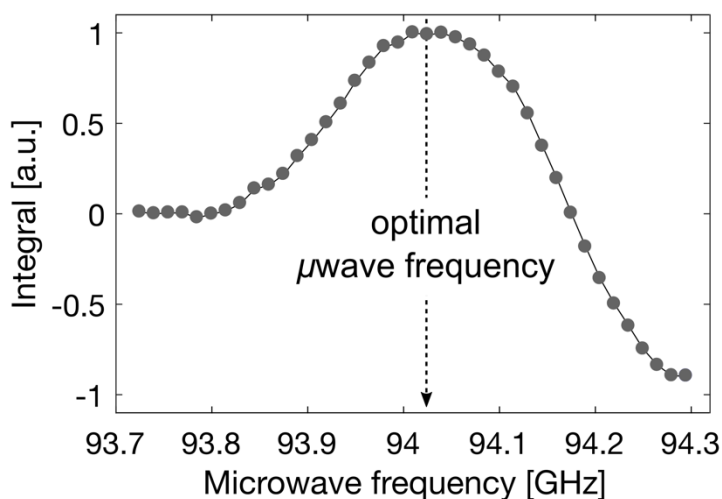
Figure 2.4: Microwave frequency dependence ("sweep") of DNP (3.35 T, 1.4 K) for ^{19}F nuclei from a sample containing of 0.1 M TFA with 15 mM TEMPOL in D_2O/DMSO-d_6 (v/v 1:1). Each data point was obtained after 1 min of microwave irradiation using 100 mW. The maximum NMR signal was observed at the microwave frequency of 94.01 GHz.

Larmor frequency of ^{19}F at the magnetic field of the polarizer (134.14 MHz at 3.35 T), which is indicative of thermal mixing as the prevailing DNP mechanism over the others. This large separation of positive and negative peak frequencies compared to the magnitude of the nuclear Larmor frequency has been observed for ^{1}H and ^{13}C using TEMPO and 4-oxo-TEMPO as well.[121,126,133]

2.2.4. Solid-state polarization build-up

^{19}F solid-state NMR signals measured of a sample of 1 M TFE doped with 30 mM TEMPOL are shown in Figure 2.5a. The spectra in the figure are from the 10th scan in a multi-scan experiment for measuring signal buildup, measured 9 minutes after the start of the experiment. At this time, the signal intensity of the spectra with microwave irradiation at 94.01 GHz is > 95% than the maximum that was reached. It can be seen that the
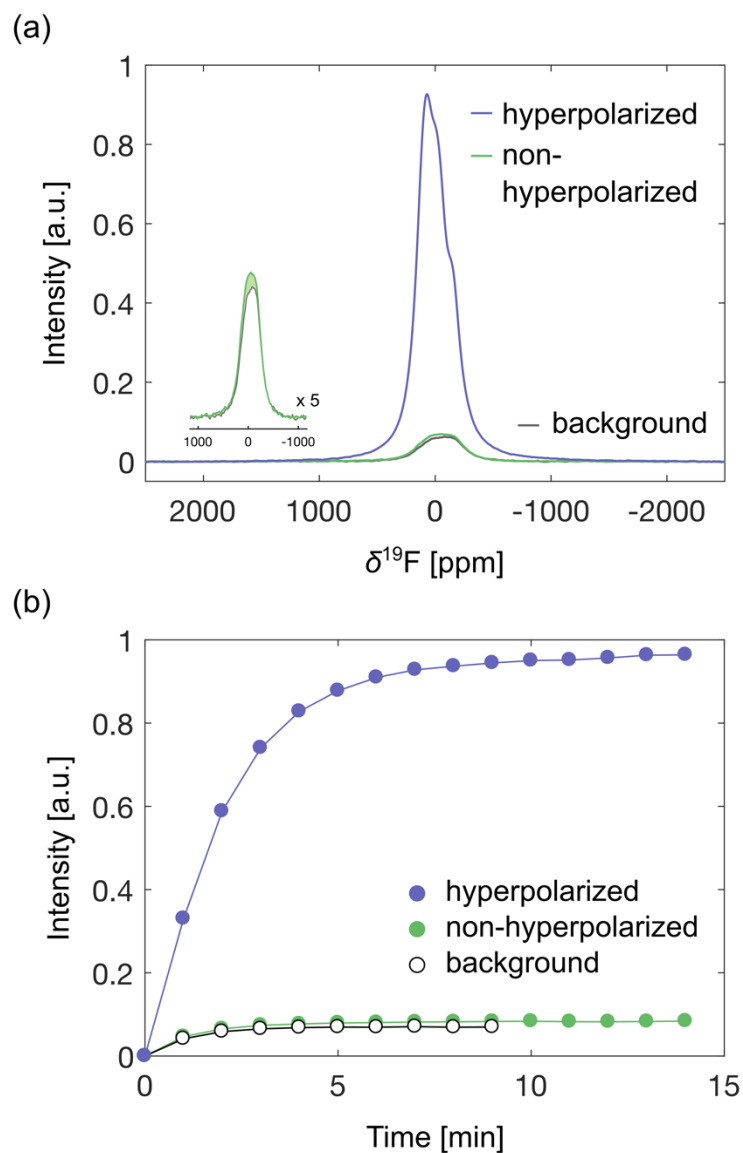
Figure 2.5: (a) NMR spectrum of hyperpolarized and non-hyperpolarized 1 M TFE sample with 30 mM TEMPOL (drawn in purple, and green, respectively), and background spectrum measured with an empty sample chamber (grey). These spectra are the 10th scans of solid-state polarization build-up curves shown in (b). The colored circles represent the signal intensities from the measurements with the sample, and the open circles from the background measurement.

intensity of hyperpolarized signal is 10 times higher than that observed without microwave irradiation. The signal arising from the sample, however, was found to be only a fraction of the observed signal, with a larger contribution of a background signal. The background was measured using the probe with the empty sample chamber. This background signal is from polytetrafluoroethylene dielectric (PTFE) surrounding the center conductor of the coaxial cable. In the inset of Figure 2.5a, the shaded area represents the pure NMR signal from a sample without hyperpolarization. After background subtraction, an approximately 80-fold enhancement by DNP was calculated. The signals in all scans were integrated over the spectral width and plotted as a function of polarization time in Figure 2.5b.

A set of polarization buildup curves measured from the samples with varying substrate concentrations including the case of [-CF$_3$] = 1 M are shown in Figure 2.6a. It was observed that the signal intensity was saturated most rapidly for 1 M sample and slowly with less concentrated ones. It can be clearly seen that the signal intensities build up faster for higher -CF$_3$ concentration in the normalized intensity plot (Figure 2.6b). The polarization build-up time constant (τ_b) for each dataset determined using Equation (2.1) are shown in the inset. The results show that a higher ^{19}F concentration shortened the time for achieving a maximum polarization from 10 to 7, and to 2 min. The effect of substrate concentration on τ_b can be explained by spin diffusion which is responsible for propagating polarization to neighboring nuclei farther from the paramagnetic centers.[134] The reduced internuclear distance (r) in the higher ^{19}F concentration sample facilitates the spin diffusion.[135,136] Similar observations have been reported in literatures. From the work done by Comment, the ^{13}C polarization rate of acetate increases as the solute concentration increases at constant TEMPO concentration.[137] The same effect has been observed by
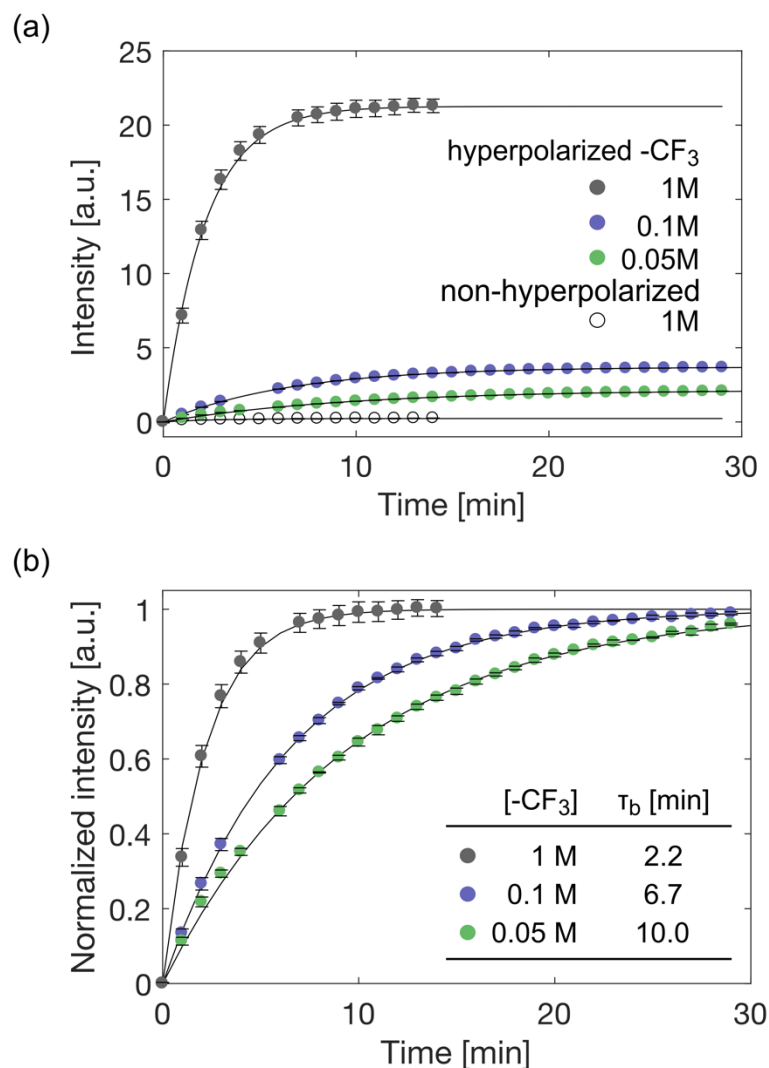
Figure 2.6: (a) Solid-state polarization buildup curves of 1, 0.1, and 0.05 M CF_3CH_2OH with 30 mM TEMPOL in D_2O/DMSO-d_6 (v/v 1:1) with and without the microwave irradiation. Data points were obtained at 1.4 K during irradiation with microwaves of 94.01 GHz and 100 mW power (filled circles) or with 0 mW (open circles). Each data point is the averaged signal intensity from 3 repetitions after subtraction of background signal. Standard deviations are shown with error bars. Solid lines represent the fitted curves obtained using Equation (2.1). (b) Normalized signal intensities of the polarization build-up curves shown in (a). For each curve, the signal intensities were normalized with respect to the value of I_M obtained from data fitting. The values of τ_b determined from the fitting are shown together.

enriching the density of target nuclei using a labeled glassy matrix[138] or adding a copolarization agent,[139] which were both performed for ^{13}C polarization. The absolute signal intensities per mole of ^{19}F were within a factor of two of each other. The absolute polarization enhancements, however, were not quantitatively analyzed since the signals from non-hyperpolarized measurements were not observable in the samples with low concentrations.

2.2.5. Conclusions

Hyperpolarization of ^{19}F by microwave-driven DNP technique has been demonstrated. The microwave frequency dependence of hyperpolarized ^{19}F NMR signals observed with a water-soluble nitroxide radical TEMPO suggests that the dominant DNP mechanism is thermal mixing. At the optimal microwave frequency for generating positive nuclear spin polarization, the dependence of substrate concentration on the polarization build-up time constant was determined. A higher ^{19}F concentration has yielded shorter polarization time, which could be explained by enhanced spin diffusion in the solid. This observation agrees with reported observations for ^{13}C nuclei. The measured polarization buildup time constants indicate that in general the maximum attainable polarization of ^{19}F could be obtained in half an hour.

3. AFFINITY SCREENING USING COMPETITIVE BINDING WITH FLUORINE-19 HYPERPOLARIZED LIGANDS[*]

3.1. Introduction

Fluorine atoms rarely occur in biology but are used in pharmaceuticals. Consequently, NMR of ^{19}F is often part of the screening protocol for protein−ligand interactions in drug discovery.[45,140–142] Detection of ^{19}F spectra is convenient because they are free of background signals from the protein or even the solvent. Owing to the high gyromagnetic ratio and 100% abundance of the ^{19}F isotope, the NMR detection sensitivity is as high as for protons. Nevertheless, a relatively high ligand concentration is required to obtain a sufficient S/N ratio for identification of the protein−ligand interaction. Recently, we demonstrated that D-DNP, a hyperpolarization technique to increase the NMR sensitivity by several orders of magnitude,[143] is applicable to ^{19}F-NMR in screening experiments.[144] A limitation of ^{19}F-NMR detection lies in the omission of non-fluorinated drug candidates. However, if a suitable fluorinated ligand is known for a protein of interest, this ligand can be used in competitive binding experiments to report on other, non-fluorinated ligands. Competitive binding experiments have been demonstrated using proton or fluorine based NMR,[44,145–147] as well as with hyperpolarized long-lived spin states.[148] If the reporter ligand is in fast exchange with the protein, ligands with a range of binding affinities can thus be identified, such as using the Fluorine Chemical Shift Anisotropy and Exchange for Screening method.[44] Here, we demonstrate the measurement

of dissociation constants of a non-fluorinated ligand from a rapid, single-scan measurement of the ^{19}F spin-spin relaxation rate (R_2) of a DNP hyperpolarized reporter ligand.

3.2.   Experimental section

3.2.1. DNP-NMR Spectroscopy

Experiments without hyperpolarization, used 100 μM TFBC (Maybridge, UK), 1.8 μM trypsin (AMRESCO, Solon, OH) and 40 μM benzamidine (Sigma Aldrich, St. Louis, MO) in buffer (50 mM Tris, 100 mM NaCl and 5 mM $CaCl_2$, pH 8.0). NMR data were acquired using a broadband observe (BBO) probe with ^{19}F tuning capability on the ^1H channel, on a 400 MHz spectrometer (Bruker Biospin, Billerica, MA). For D-DNP experiments, 8 μL of 0.134 mM TFBC and 2 μL of 150 mM 4-hydroxy-2,2,6,6-tetramethylpiperidine-1-oxyl (Sigma Aldrich, St. Louis, MO) in 80% d_6-DMSO and 20% D_2O v/v were irradiated in a HyperSense DNP polarizer (Oxford Instruments, Abingdon, UK), with 100 mW power of 94.005 GHz microwaves, for 30 min at T = 1.4 K. The hyperpolarized sample was dissolved by 4 mL pre-heated buffer and injected into a 5 mm NMR tube,[102,149] where 25 μL buffer, trypsin solution or mixture of trypsin and non-fluorinated ligand was pre-loaded. Final NMR sample volume was 500 μL. NMR spectra were acquired 400 ms after injection at T = 304 K. The concentration of trypsin was determined by UV spectrophotometry, and of TFBC by ^{19}F-NMR. Sample dilution during dissolution (average 1:100) was determined by NMR using a known standard. Single-scan CPMG experiments collected 16384 data points at intervals of 420 μs. Background signal from the NMR probe was obtained in a separate measurement and subtracted. Influence

from background signal was further reduced by processing data only after an initial delay of 42.4 ms. Monte Carlo simulation was performed using Matlab (MathWorks, Natick, MA).

3.2.2. Competitive binding model

In competitive binding, two ligands bind reversibly to the same position of a protein. When a dissociation constant is known for one ligand and it is in fast exchange, it can be used as a reporter ligand to manifest the binding affinity of the other according to the following mechanism

$$CP + R \;\underset{k_{on}}{\overset{k_{off}{}^{C}}{\rightleftharpoons}}\; R + C + P \;\underset{k_{off}{}^{R}}{\overset{k_{on}}{\rightleftharpoons}}\; RP + C \tag{3.1}$$
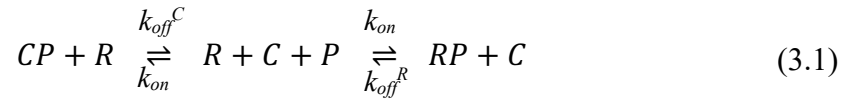
where R, C and P represent a reporter ligand, a competing ligand, and protein, respectively. The association rate constant is indicated by k_{on}, and the dissociation rate constants for R and C are represented by $k_{off}{}^{R}$ and $k_{off}{}^{C}$, respectively. Mass balance equations can be written for the reporter ligand, competing ligand and protein under equilibrium.

$$[R]_t = [R]_{eq} + [RP]_{eq} \tag{3.2}$$

$$[C]_t = [C]_{eq} + [CP]_{eq} \tag{3.3}$$

$$[P]_t = [P]_{eq} + [RP]_{eq} + [CP]_{eq} \tag{3.4}$$

The dissociation constants of the reporter and competing ligands ($K_{D,r}$ and $K_{D,c}$, respectively) are expressed using the terms above.

$$K_{D,r} = \frac{[R]_{eq} \cdot [P]_{eq}}{[RP]_{eq}}$$

$$K_{D,c} = \frac{[C]_{eq} \cdot [P]_{eq}}{[CP]_{eq}}$$

3.2.3. Mathematical derivation of K_D determination through R_2-based competitive binding experiments

A requirement for the competitive ligand-protein binding experiments is that the reporter ligand should be in fast chemical exchange between free and bound forms in order to convey correct binding information of the competing ligand.[145–147,44] The observed spin-spin relaxation rate ($R_{2,r}$) for the ligand under these conditions in the presence of a target protein is provided in Equation (1.4).[26,140,150,151] When the fraction of bound ligand ($p_{b,r} = [RP]_{eq}/[R]_t$) is assumed to be negligibly small that $p_{b,r}(1 - p_{b,r})^2 \approx p_{b,r}$, the $R_{2,r}$ becomes proportional to $p_{b,r}$ as shown in Equation (1.5).

For $K_{D,c}$ calculation, the amount of bound reporter ligand that becomes replaced by the competing ligands is the key factor. The change is observed by determining the R_2 relaxation rates of the reporter ligand. The Equation (1.5) can be rewritten for the reporter ligand as following

$$R_{2,r}^{(nc)} = \left(1 - p_{b,r}^{(nc)}\right)R_{2,r}^{(f)} + p_{b,r}^{(nc)}\left(R_{2,r}^{(b)} + R_{ex}\right) \tag{3.5}$$

$$R_{2,r}^{(c)} = \left(1 - p_{b,r}^{(c)}\right)R_{2,r}^{(f)} + p_{b,r}^{(c)}\left(R_{2,r}^{(b)} + R_{ex}\right) \tag{3.6}$$

where $R_{2,r}^{(f)}$ and $R_{2,r}^{(b)}$ are the R_2 relaxation rates of free and bound ligands, respectively, and $R_{2,r}^{(nc)}$ and $R_{2,r}^{(c)}$ are those of reporter ligand in the presence of protein without competition and that in the presence of both protein and a competing ligand under competitive equilibrium. The fraction of bound reporter ligand in the presence of only

protein ($p_{b,r}^{(nc)}$) is determined by Equation (1.2).[22,151] When $[R]_t$, $[P]_t$ and $K_{D,r}$ are known,

the fraction of bound reporter ligand under a competitive equilibrium ($p_{b,r}^{(c)} = [RP]_{eq}/[R]_t$)

can be calculated based on $p_{b,r}^{(nc)}$ and the ratio of differences in relaxation rates defined as

α for convenience.

$$p_{b,r}^{(c)} = \alpha \cdot p_{b,r}^{(nc)} \tag{3.7}$$

$$\alpha = \frac{R_{2,r}^{(c)} - R_{2,r}^{(f)}}{R_{2,r}^{(nc)} - R_{2,r}^{(f)}} \tag{3.8}$$

From $p_{b,r}^{(c)}$, the concentration of reporter ligand–protein complex at the equilibrium ($[RP]_{eq}$)

is calculated.

$$[RP]_{eq} = p_{b,r}^{(c)} \cdot [R]_t \tag{3.9}$$

The apparent dissociation constant (*i.e.*, the dissociation constant that would be calculated

if no competition were assumed) of the reporter ligand is given by[145]

$$K_{D,app} = \frac{\left([P]_t - [RP]_{eq}\right)\left([R]_t - [RP]_{eq}\right)}{[RP]_{eq}}$$

$$= \frac{[P]_t[R]_t - [P]_t[RP]_{eq} - [R]_t[RP]_{eq} + [RP]_{eq}^{2}}{[RP]_{eq}} \tag{3.10}$$

Using the term $p_{b,r}^{(c)}$, Equation (3.11) can be written as

$$K_{D,app} = [P]_t\left(\frac{1}{p_{b,r}^{(c)}} - 1\right) - [R]_t\left(1 - p_{b,r}^{(c)}\right) \tag{3.11}$$

The $K_{D,app}$ is then used to determine the dissociation constant of the competing ligand ($K_{D,c}$)

according to the equation:

$$K_{D,c} = \frac{[C]_{eq} \, K_{D,r}}{K_{D,app} - K_{D,r}} \qquad (3.12)$$

The concentration of free competing ligand ($[C]_{eq}$) can be calculated from the mass balanced equations and equilibrium constants. It is expressed by

$$[C]_{eq} = [C]_t - [P]_t + \left(\frac{K_{D,r}}{[R]_t - p_{b,r}^{(c)}[R]_t} + 1 \right) p_{b,r}^{(c)}[R]_t \qquad (3.13)$$

3.3. Results and discussion

3.3.1. Affinity screening

A CF$_3$-functionalized ligand, TFBC acts as a reporter ligand for binding to the serine protease trypsin from *B. taurus* (Figure3.1a). Binding of a second, non-fluorinated ligand causes changes in the fraction of bound reporter ligand, which are manifested as changes in R_2, observed in single-scan CPMG experiments.[31] For demonstration, Figure 3.1b shows spin-echo intensities of TFBC recorded without hyperpolarization. A measurement under competition with the trypsin inhibitor benzamidine is complemented by two reference experiments.

The relaxation rate at the competitive equilibrium ($R_{2,r}^{(c)}$) is in-between those of free reporter ligand ($R_{2,r}^{(f)}$) and of reporter in the presence of protein without competition ($R_{2,r}^{(nc)}$). The dissociation constant of the competing ligand of interest ($K_{D,c}$) can be determined from the measured R_2 values, which depend on the fraction of bound reporter ligand ($p_{b,r}$) using a model for competitive binding to a single site.[26,32,150] For small $p_{b,r}$, $R_{2,r}$ is a $p_{b,r}$-weighted average of relaxation rates of free and bound ligand as described by
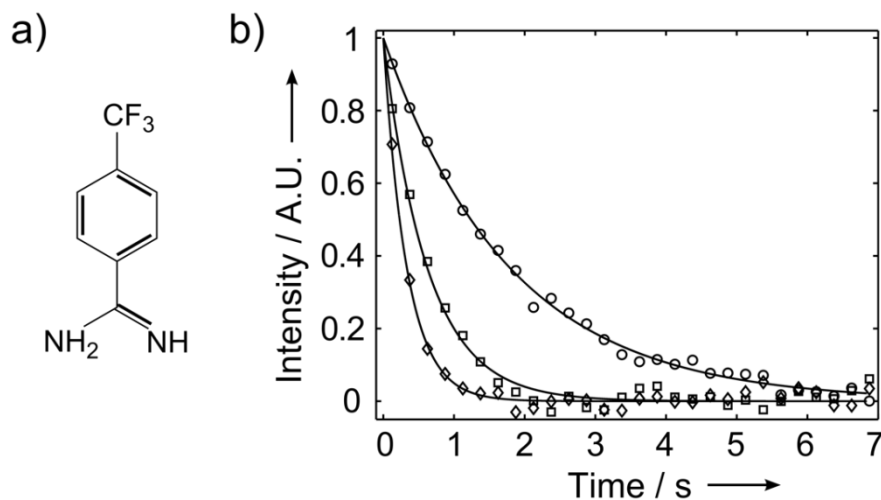
Figure 3.1: (a) Structure of reporter ligand 4-(trifluoromethyl)benzene-1-carboximidamide (TFBC). (b) Single-scan CPMG spin-echo intensities, averaged 128 times, of 100 μM TFBC without hyperpolarization, obtained in absence (o) and presence (◊) of 1.8 μM trypsin, and in the presence of both 1.8 μM trypsin and 40 μM benzamidine (□). Each point shown is the average of 581 successive data points, which were measured at time intervals of 420 μs. R_2 relaxation rates were obtained from the fit to a single exponential; $R_{2,r}^{(f)} = 0.60$ s^{-1} (o), $R_{2,r}^{(nc)} = 3.00$ s^{-1} (◊), $R_{2,r}^{(c)} = 1.61$ s^{-1} (□).

Equation (1.5). In order to determine the fraction of bound reporter ligand under competitive binding ($p_{b,r}^{(c)}$), a parameter α, which depends on measured relaxation rate differences as defined in Equation (3.8), is introduced. It is also practical as it cancels paramagnetic contributions from free radicals used in DNP. Under the above assumption, $p_{b,r}^{(c)}$ is equal to the product of α and $p_{b,r}^{(nc)}$ as shown in Equation (3.7). Consequently, $p_{b,r}^{(c)}$ can be found using the result from the R_2 measurements in combination $p_{b,r}^{(nc)}$ which depends only on known parameters (dissociation constant of reporter $K_{D,r}$, and total concentrations of protein, $[P]_t$, and reporter $[R]_t$).[22] By calculating the apparent dissociation constant for the reporter ligand ($K_{D,app}$) and the concentration of free

competing ligand $[C]_{eq}$ with knowledge of $K_{D,r} = 142 \, \mu M^{144}$ using the Equations (3.10) -

(3.13), the data from the non-hyperpolarized measurement in Figure 3.1b yields $K_{D,c} =$

$15.7 \pm 1.9 \, \mu M$ for benzamidine.

By utilizing D-DNP, ^{19}F-NMR signal enhancements of >1000-fold were achieved.

Hyperpolarized ligands were injected into mixtures of competing ligand and protein,

followed by acquisition of single-scan CPMG data. It was possible to considerably reduce

the final reporter ligand and protein concentrations to $1 \, \mu M$. At such concentrations, $p_{b,r}^{(nc)}$

was calculated to be 0.7% where the above assumption can be safely made. Data for three

ligands at three different concentrations is shown in Figure 3.2. Information on binding is

obtained in two different regimes. A simple confirmation of binding can be made if the

reporter ligand is fully displaced, by observing $R_{2,r}^{(c)} \approx R_{2,r}^{(f)}$ (panels in upper right corner

in the figure). A numerical value for $K_{D,c}$ can be calculated in the case of partial

displacement, when $R_{2,r}^{(nc)} > R_{2,r}^{(c)} > R_{2,r}^{(f)}$ (upper left to lower right diagonal panels). The

R_2 and $K_{D,c}$ values obtained from these experiments are summarized in Table 3.1.

.
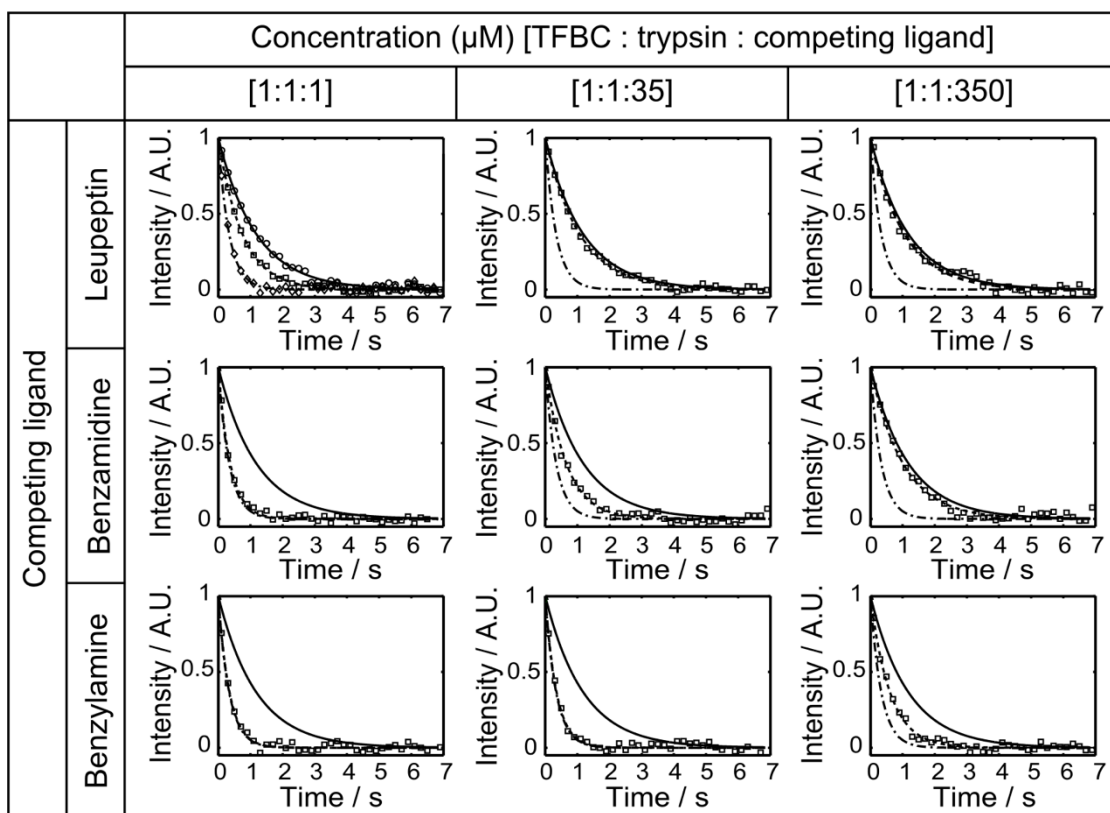
Figure 3.2: CPMG spin-echo intensities of 1 μM hyperpolarized TFBC. The data points for reference experiments with TFBC in the absence (o) and presence (◊) of 1 μM trypsin are only included in the first graph, but the fit curves are shown in all panels. The data points of hyperpolarized TFBC in the competition experiments are shown in all graphs (□). Each point shown is the average of 465 successive data points measured at time intervals of 420 μs. NMR probe-head background has been subtracted and data before 42.4 ms discarded.

Table 3.1: Summary of $R_{2,r}$ and $K_{D,c}$ determination

Competing ligand	$R_{2,r}^{(c)}$ / s^{-1} [a] ($[R]_t = [P]_t = 1\ \mu$M)			$K_{D,c}$ / μM
	$[C]_t = 1\ \mu$M	$[C]_t = 35\ \mu$M	$[C]_t = 350\ \mu$M	
Leupeptin	$1.39 \pm 0.08\ (3)^{[b]}$	0.94, 0.93 (2)	0.93, 0.94 (2)	0.09 ± 0.03

45

Table 3.1 Continued

Competing ligand	$R_{2,r}^{(c)}$ / s^{-1} [a] ([R]$_t$ = [P]$_t$ = 1 μM)			$K_{D,c}$ / μM
	[C]$_t$ = 1 μM	[C]$_t$ = 35 μM	[C]$_t$ = 350 μM	
Benzamidine	2.75, 2.53 (2)	1.52 ± 0.03 (3)	0.99, 0.94 (2)	16.3 ± 1.61
Benzylamine	2.54, 2.90 (2)	2.86, 2.53 (2)	1.73 ± 0.11 (3)	258.1 ± 56.6

[a] $R_{2,r}^{(c)}$ are results from fits of DNP-NMR echo intensities to a single exponential, processed as in Figure 3.2. Mean and standard deviations of $K_{D,c}$ are from calculations with all possible combinations of measured R_2 values. Reference values, $R_{2,r}^{(f)}$ = 0.85 ± 0.03 s^{-1} and $R_{2,r}^{(nc)}$ = 2.92 ± 0.12 s^{-1}, were determined each from three DNP-NMR measurements. [b] In parentheses is the number of repetitions performed.

Table 3.2: Summary of results from non-hyperpolarized single-scan CPMG experiments to determine $K_{D,c}$ of competing ligands

Competing ligand	Sample concentrations	$R_{2,r}$ / s^{-1} [a]			$K_{D,c}$ / μM
		$R_{2,r}^{(f)}$	$R_{2,r}^{(nc)}$	$R_{2,r}^{(c)}$	
Leupeptin	[R]$_t$ = 100 μM, [P]$_t$ = 1 μM, [C]$_t$ = 1 μM	0.60 ± 0.05	2.05 ± 0.10	1.04 ± 0.03	0.08 ± 0.02
Benzamidine	[R]$_t$ = 100 μM, [P]$_t$ = 1.8 μM, [C]$_t$ = 40 μM	0.60 ± 0.05	3.08 ± 0.08	1.51 ± 0.07	15.7 ± 1.90
Benzylamine	[R]t = 100 μM, [P]t = 1.8 μM, [C]t = 400 μM	0.60 ± 0.05	3.08 ± 0.08	1.79 ± 0.15	217.9 ± 43.1

[a] $R_{2,r}$ are results from fits of single-scan CPMG echo intensities to a single exponential. A total of 128 scans were recorded with a repetition time of 3.2 s. Each measurement was repeated three times, using samples freshly prepared from stock solutions. Mean values and standard deviations of $K_{D,c}$ are obtained from the result of calculations with all possible combinations of measured values for $R_{2,r}^{(f)}$, $R_{2,r}^{(nc)}$ and $R_{2,r}^{(c)}$ in Equations (3.7) - (3.13).
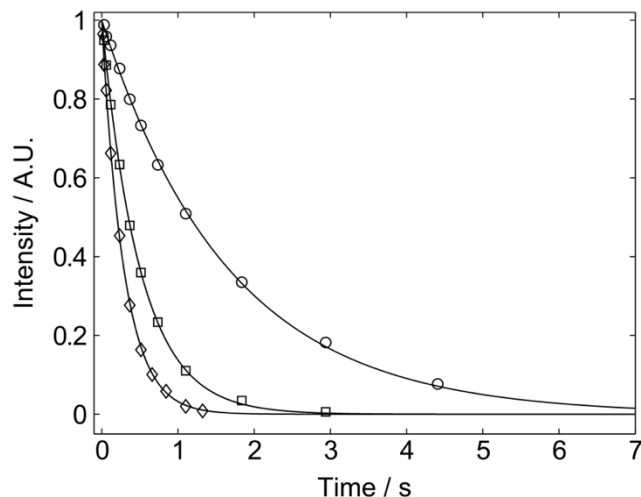
Figure 3.3: Time dependence of the spin-echo intensities of 5 mM TFBC obtained in absence (o) and presence (◊) of 35 μM trypsin, and in the presence of both 35 μM trypsin and 0.8 mM benzamidine (□) from the conventional multi-scan CPMG experiments without hyperpolarization. R_2 relaxation rates were obtained from fit to a single exponential. ($R_{2,r}^{(f)} = 0.60$ s^{-1} (o), $R_{2,r}^{(nc)} = 3.43$ s^{-1} (◊), $R_{2,r}^{(c)} = 1.98$ s^{-1} (□)).

For validation, non-hyperpolarized CPMG experiments were conducted using higher sample concentrations. The CPMG spin-echo intensities obtained from single-scan CPMG experiments are summarized in Table 3.2. Those from multi-scan CPMG experiments (pseudo 2D) are shown in Figure 3.3, and resultant R_2 and $K_{D,c}$ values are summarized in Table 3.3. The DNP-NMR measurements are in good agreement with those, as well as with literature values under similar, but not identical conditions (leupeptin, 0.031−0.4 μM; benzamidine and benzylamine, 18 μM and 300 μM at 100 mM Tris, pH=8.0, 298 K).[152–154] Lowering the final concentration of protein and competing ligand to 0.5 μM, still resulted in a $K_{D,c}$ value that is within error limits of the value from Table 3.1 (Figure 3.4).

Table 3.3: Summary of results from non-hyperpolarized conventional multi-scan CPMG experiments to determine $K_{D,c}$ of competing ligands

Competing ligand	Sample concentrations	$R_{2,r}$ / s^{-1}			$K_{D,c}$ / μM
		$R_{2,r}^{(f)}$	$R_{2,r}^{(nc)}$	$R_{2,r}^{(c)}$	
Leupeptin	$[R]_t = 5$ mM, $[P]_t = 15$ μM, $[C]_t = 15$ μM	0.62	1.77	1.01	0.07
Benzamidine	$[R]_t = 5$ mM, $[P]_t = 35$ μM, $[C]_t = 0.8$ mM	0.60	3.43	1.98	20.8
Benzylamine	$[R]_t = 5$ mM, $[P]_t = 35$ μM, $[C]_t = 8$ mM	0.60	3.43	2.00	212.6
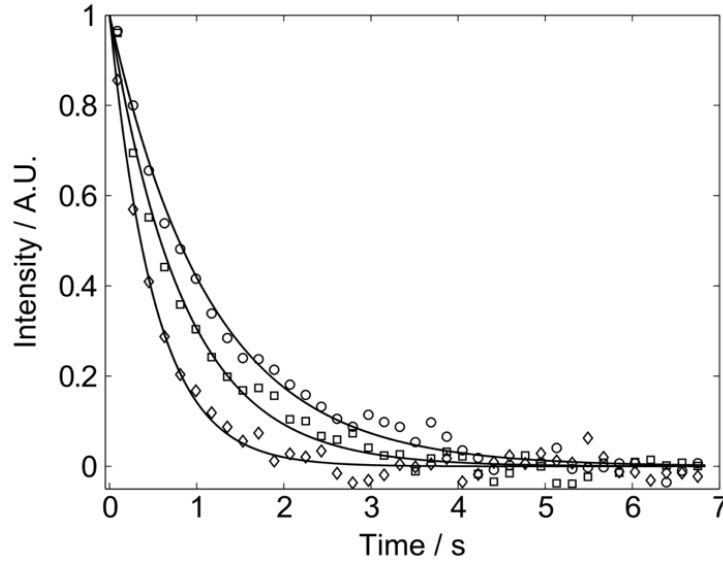
Figure 3.4: Time evolution of the spin-echo intensities of 1 μM TFBC obtained in absence (o) and presence (◊) of 0.5 μM trypsin, and in the presence of both 0.5 μM trypsin and 0.5 μM leupeptin (□) from the single-scan CPMG experiments using ^{19}F DNP-NMR. R_2 relaxation rates were obtained from fit to a single exponential. ($R_{2,r}^{(f)} = 0.87$ s^{-1} (o), $R_{2,r}^{(nc)} = 1.95$ s^{-1} (◊), $R_{2,r}^{(c)} = 1.19$ s^{-1} (□)) Each point shown is the average of 428 successive data points, which were measured at time intervals of 420 μs. The $K_{D,c}$ value determined from the fit is 0.06 ± 0.03 μM.

3.3.2. Accuracy of K_D determination

The effect of ligand concentration on the parameters observed is illustrated in Figure 3.5a. The relationship between $K_{D,c}$ and α is plotted for the three concentrations used, along with the experimental data points. The highest accuracy is expected where the slopes of curves are smallest, which occurs when the reporter ligand is partially displaced.
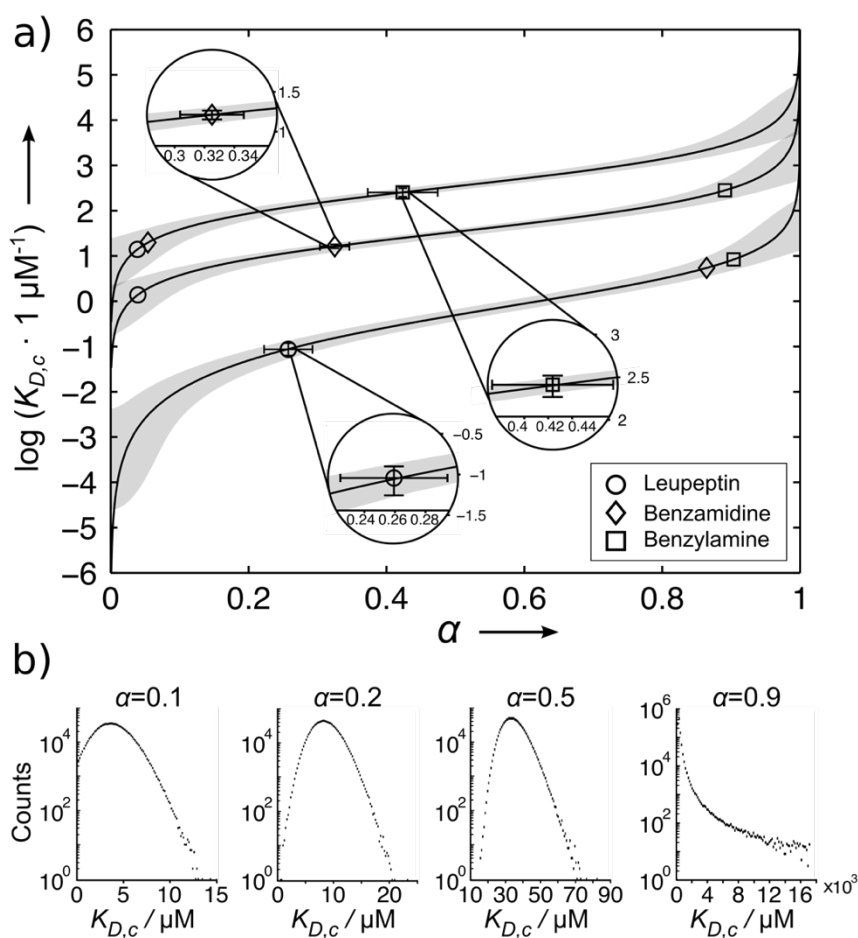
Figure 3.5: (a) Dependence of $\log(K_{D,c})$ on α, for $[[R]_t, [P]_t, [C]_t] = [1, 1, 1]$ μM (bottom curve), $[1, 1, 35]$ μM (middle curve) and $[1, 1, 350]$ μM (top curve) and $K_{D,r} = 142$ μM. Points indicate the DNP NMR measurements from Table 3.1. Shaded areas contain 80% of $K_{D,c}$ values obtained from the Monte Carlo simulations. (b) Logarithmic histograms of $K_{D,c}$ from the Monte Carlo simulations, for selected values of α on the middle curve in (a).

The accuracy of the $K_{D,c}$ determination was further assessed in terms of errors in α, by performing Monte Carlo simulations. Using 10^6 random samples, normal distributions of an α value were created with a standard deviation of 0.04, from which unphysical values outside of $0 < \alpha < 1$ were removed. An exact normal distribution of α would occur for normally distributed R_2 values in its numerator and an exactly known denominator. Assuming a higher accuracy in the denominator appears reasonable, it is composed of reference values valid for an entire set of screening experiments. The interval containing 80% of the resulting $K_{D,c}$ is shaded in Figure 3.5a, indicating that an error in α is least affecting $K_{D,c}$ when α is close to 0.5. Simulation results for four values of α are plotted as histograms in Figure 3.5b. The long tail of the distributions present when the mean of α is close to 1, and the non-vanishing probability for $K_{D,c} = 0$ as the mean of α approaches 0 can be attributed as the cause for the increasing error under these conditions.

3.3.3. Numerical solutions to binding kinetics

For the calculation of $K_{D,c}$, it is assumed that the system is under chemical equilibrium. In the competitive binding experiments, a sufficient amount of equilibration time is therefore required before acquiring signals from the reporter ligands, in order to avoid underestimating the binding constant of the competing ligands. Particularly, ligands with slower k_{off} values require a longer time to reach equilibrium. By obtaining numerical solutions of rate equations for the competitive binding, the required equilibration time was estimated and assessed whether our experiments satisfied the condition.

Using a simple, competitive mechanism, as shown in the Equation (3.1), differential rate equations can be written for the free reporter ligand ($[R(t)]$), free competing ligand ($[C(t)]$) and free protein ($[P(t)]$).

$$\frac{d[R(t)]}{dt} = k_{off}^{R}[RP(t)] - k_{on}[R(t)][P(t)] \qquad (3.14)$$

$$\frac{d[R(t)]}{dt} = k_{off}^{R}[RP(t)] - k_{on}[R(t)][P(t)] \qquad (3.15)$$

$$\frac{d[P(t)]}{dt} = k_{off}^{C}[CP(t)] + k_{off}^{R}[RP(t)] - k_{on}[P(t)]([C(t)] + [R(t)]) \qquad (3.16)$$

In the experiments, the competing ligand and the protein are pre-mixed and diluted by the hyperpolarized reporter ligand solution. Therefore, the reporter ligand perturbs the equilibrium between the competing ligand and the protein. Assuming that the dilution occurs instantaneously, initial conditions of the competing ligand and the protein are chosen as diluted concentrations of the binary equilibrium between the two in the pre-dilution condition. With the fraction of bound competing ligand ($p_{b,c}^{(nc)}$) at the equilibrium calculated using the Equation (3.7), the initial concentrations are found as follows,

$$[CP] = p_{b,c}^{(nc)} \cdot [C]_t \times f_d \qquad (3.17)$$

$$[CP] = p_{b,c}^{(nc)} \cdot [C]_t \times f_d \qquad (3.18)$$

$$[P] = \left(1 - p_{b,c}^{(nc)}\right) \cdot [P]_t \times f_d \qquad (3.19)$$

where f_d is a dilution factor. Accordingly, the mass balance equations (Equation (3.2) - Equation (3.4)) can be written as

$$[R]_t = [R(0)] = [R(t)] + [RP(t)] \qquad (3.20)$$

$$[C]_t = [C(0)] + [CP(0)] = [C(t)] + [CP(t)] \tag{3.21}$$

$$[P]_t = [P(0)] + [CP(0)] = [P(t)] + [RP(t)] + [CP(t)] \tag{3.22}$$

The numerical solutions for the free reporter, competitor ligands and protein obtained at conditions corresponding to those in the 9 panels of Figure 3.2 are shown as a function of time in Figure 3.6 (parameters are stated in the figure caption). It was assumed that $k_{on} = 1 \cdot 10^8$ M^{-1}s^{-1}.[155] Of particular interest is the solid black curve, which corresponds to the reporter ligand, of which the NMR signal is measured. It can be seen that the time to reach equilibrium ranges from less than a millisecond (e.g. panel (i)) to about 100 ms (panel (a)). Therefore, a typical stabilization time of 400 ms that may be employed for dissolution DNP experiments (and is used in the experiments in this work), is sufficient for equilibration under these conditions.

The hyperpolarized experiments demonstrated in this chapter were performed with pre-mixed competing ligand and protein, into which the hyperpolarized reporter ligand is injected. It would alternatively be possible to inject the competing ligand at the same time as the hyperpolarized reporter ligand. In this scenario, the initial conditions do not depend on the pre-dilution binary equilibrium between the ligand and the protein. All three species exist in free forms at the start of the experiments. Calculations for the time evolution of concentrations were also performed for the possible variation of the experiment. The numerical solutions were obtained the same way which is shown above, but with the initial conditions $[R(0)] = [R]_t$, $[C(0)] = [C]_t$, $[P(0)] = [P]_t$, $[RP(0)] = 0$ μM and $[CP(0)] = 0$ μM.
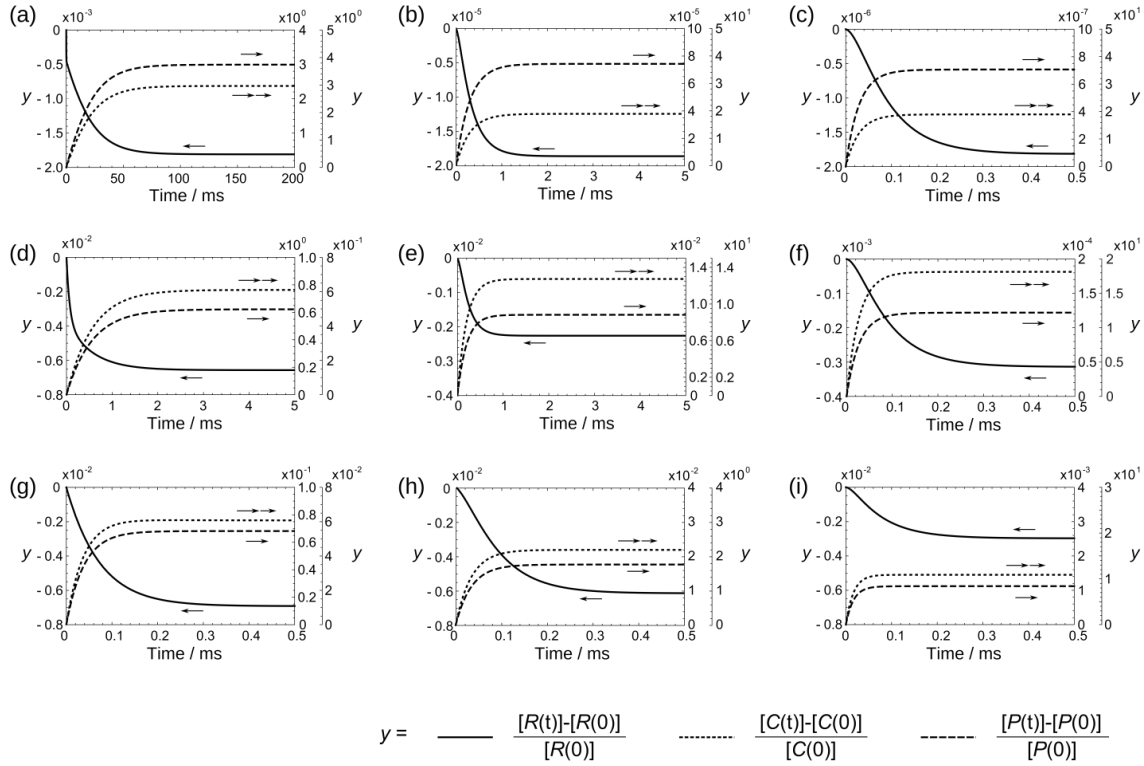
Figure 3.6: Relative change in the concentrations of free reporter, competing ligands and protein as a function of time, when the reporter ligand is added at time $t = 0$. Each panel shows a graph corresponding to the conditions: (a) $K_{D,c} = 0.09~\mu M$, $[[C]_t, [C(0)], [P(0)]] = [1, 0.07, 0.07]~\mu M$, (b) $K_{D,c} = 0.09~\mu M$, $[[C]_t, [C(0)], [P(0)]] = [35, 34, 1.3 \cdot 10^{-4}]~\mu M$, (c) $K_{D,c} = 0.09~\mu M$, $[[C]_t, [C(0)], [P(0)]] = [350, 349, 1.3 \cdot 10^{-5}]~\mu M$, (d) $K_{D,c} = 16.3~\mu M$, $[[C]_t, [C(0)], [P(0)]] = [1, 0.58, 0.58]~\mu M$, (e) $K_{D,c} = 16.3~\mu M$, $[[C_t, [C(0)], [P(0)]] = [35, 34, 0.02]~\mu M$, (f) $K_{D,c} = 16.3~\mu M$, $[[C]_t, [C(0)], [P(0)]] = [350, 349, 0.02]~\mu M$, (g) $K_{D,c} = 258.1~\mu M$, $[[C]_t, [C(0)], [P(0)]] = [1, 0.93, 0.93]~\mu M$, (h) $K_{D,c} = 258.1~\mu M$, $[[C]_t, [C(0)], [P(0)]] = [35, 34.3, 0.27]~\mu M$, (i) $K_{D,c} = 258.1~\mu M$, $[[C]_t, [C(0)], [P(0)]] = [350, 349, 0.04]~\mu M$. In all cases, $k_{on} = 1 \cdot 10^8~M^{-1}s^{-1}$, $K_{D,r} = 142~\mu M$, $[R]_t = [R(0)] = 1~\mu M$ and $[P]_t = 1~\mu M$. These conditions correspond to the respective panels in Figure 3.2. The concentration difference of reporter ligand, competing ligand and protein is indicated by a solid, dotted and dashed line, respectively. Each curve is plotted with a separate y-axis, and the corresponding axis is indicated with arrows (solid curve: left axis, dashed curve: inner right axis, dotted curve: outer right axis). A doubled arrow refers to the outer right axis.
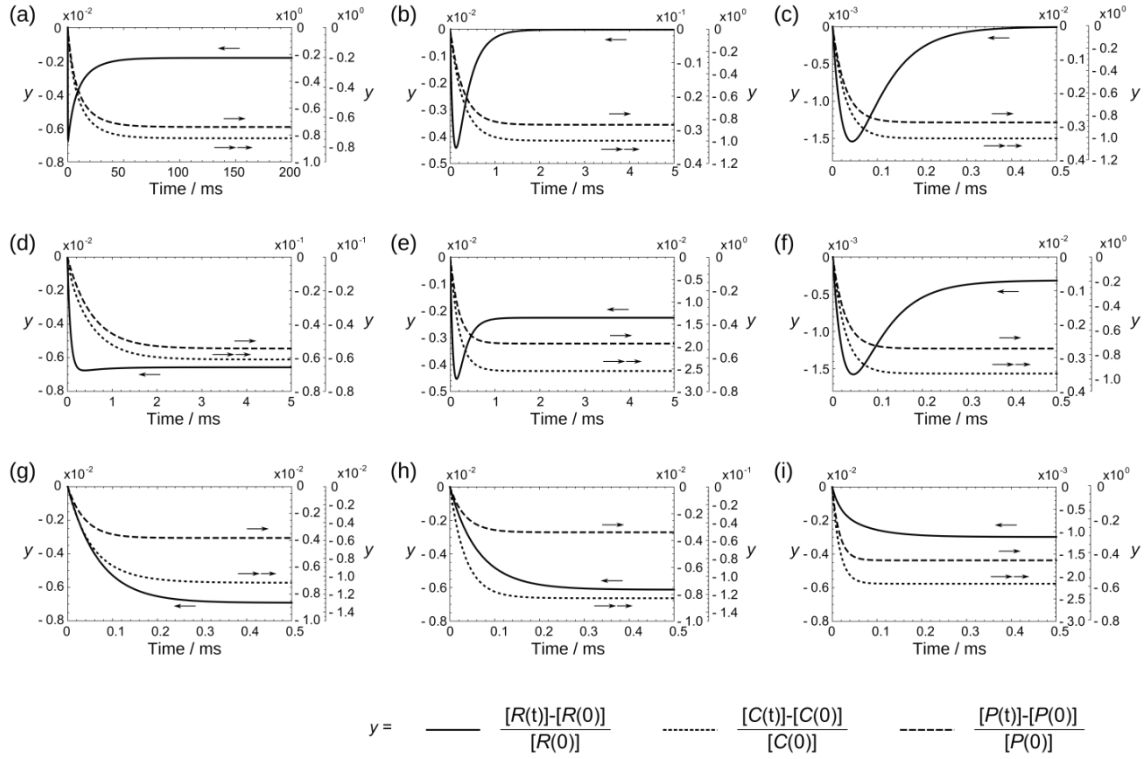
Figure 3.7: Relative change in the concentrations of free reporter, competing ligands and protein as a function of time, when the components are mixed all together at time $t = 0$. Each panel shows a graph corresponding to the conditions: (a) $K_{D,c} = 0.09\ \mu M$, $[C]_t = 1\ \mu M$, (b) $K_{D,c} = 0.09\ \mu M$, $[C]_t = 35\ \mu M$, (c) $K_{D,c} = 0.09\ \mu M$, $[C]_t = 350\ \mu M$ (d) $K_{D,c} = 16.3\ \mu M$, $[C]_t = 1\ \mu M$, (e) $K_{D,c} = 16.3\ \mu M$, $[C]_t = 35\ \mu M$, (f) $K_{D,c} = 16.3\ \mu M$, $[C]_t = 350\ \mu M$ (g) $K_{D,c} = 258.1\ \mu M$, $[C]_{tot} = 1\ \mu M$, (h) $K_{D,c} = 258.1\ \mu M$, $[C]_t = 35\ \mu M$, (i) $K_{D,c} = 258.1\ \mu M$, $[C]_t = 350\ \mu M$. In all cases, $K_{D,r} = 142\ \mu M$, $[R]_t = [R(0)] = 1\ \mu M$, $[P]_t = [P(0)] = 1\ \mu M$, $[C]_t = [C(0)]$, $[RP(0)] = 0\ \mu M$ and $[CP(0)] = 0\ \mu M$. In all cases, $k_{on} = 1 \cdot 10^8\ M^{-1}s^{-1}$ was assumed. The concentration difference of reporter ligand, competing ligand and protein is indicated by a solid, dotted and dashed line, respectively. Each curve is plotted with a separate y-axis, and the corresponding axis is indicated with arrows (solid curve: left axis, dashed curve: inner right axis, dotted curve: outer right axis). A doubled arrow refers to the outer right axis.

The results from this calculation are plotted in Figure 3.7. In some panels, *e.g.* (c) and (f), a more rapid initial change of free reporter ligand is observed, due to the absence of the pre-bound competing ligands to the proteins. It is apparent, however, that the overall equilibration time is similar to the previous case. There does not appear to be a significant advantage of one of the two experiments over the other, in terms of equilibration. Although a time delay is indispensable for reaching equilibrium, time constrains exist in the DNP experiments. An equilibration time that is much longer than the spin-lattice relaxation time (T_1) would lead to loss of hyperpolarization prior to signal acquisition. As inferred from the calculations above, a typical delay that is used in all DNP experiments to allow for sample settling, such as of several hundred milliseconds, is sufficient for equilibration of ligands with K_D as low as 100 nM. For ligands with lower dissociation constant, this equilibration time can be extended, within the limits of T_1. To evaluate a range of K_D of the competing ligand amenable determination with these experiments, calculations were also performed for other cases, where the k_{off} rates of reporter and competing ligands are slower. The concentrations for the simulations at a given value of K_D were chosen such that about 15 - 50 % of the reporter ligand that would otherwise be bound is displaced by the competing ligand. The results of these calculations are plotted in Figure 3.8.
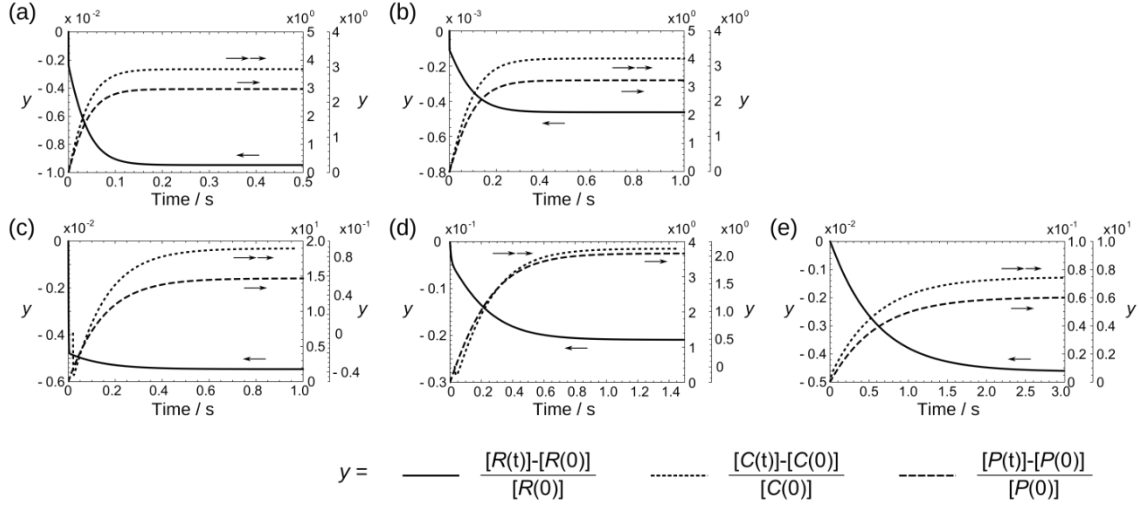
Figure 3.8: Dependence of equilibration time on the binding constants of competing and reporter ligands. Difference in the concentrations of free reporter, competing ligands and protein are shown as a function of time, assuming the equilibrium between the competing ligand and protein is established and the reporter ligand is added at time $t = 0$. Each panel shows a graph corresponding to the conditions: (a) $K_{D,r} = 142 \mu M$, $K_{D,c} = 50$ nM, $[[R]_{tot}, [P]_t, [C]_t] = [1, 0.5, 0.5] \mu M$, $[[R(0), [P(0)], [C(0)]] = [1, 0.03, 0.03] \mu M$, (b) $K_{D,r} = 142 \mu M$, $K_{D,c} = 10$ nM, $[[R]_t, [P]_t, [C]_t] = [1, 0.5, 0.5] \mu M$, $[[R(0), [P(0)], [C(0)]] = [1, 0.02, 0.02] \mu M$, (c) $K_{D,r} = 10 \mu M$, $K_{D,c} = 10$ nM, $[[R]_t, [P]_t, [C]_t] = [0.5, 0.1, 0.1] \mu M$, $[[R(0), [P(0)], [C(0)]] = [0.5, 0.007, 0.007] \mu M$, (d) $K_{D,r} = 1 \mu M$, $K_{D,c} = 10$ nM, $[[R]_t, [P]_t, [C]_t] = [0.5, 0.1, 0.1] \mu M$, $[[R(0), [P(0)], [C(0)]] = [0.5, 0.007, 0.007] \mu M$, (e) $K_{D,r} = 0.1 \mu M$, $K_{D,c} = 10$ nM, $[[R]_t, [P]_t, [C]_t] = [0.5, 0.0005, 0.05] \mu M$, $[[R(0), [P(0)], [C(0)]] = [0.5, 5 \cdot 10^{-5}, 0.045] \mu M$. In all cases, $k_{on} = 1 \cdot 10^8$ $M^{-1}s^{-1}$ was assumed. The concentration difference of reporter ligand, competing ligand and protein is indicated by a solid, dotted and dashed line, respectively. A corresponding y-axis for the graphs is indicated by an arrow. A doubled arrow refers to the very right axis.

Using the same reporter ligand as in the experiments ($K_{D,r} = 142\ \mu$M), it is found

that the lower limit of $K_{D,c}$ that can be determined is approximately 10 nM (Figure 3.8b).

It is important to keep in mind that, when the ratio of $K_{D,c}$ to $K_{D,r}$ becomes too low, the

competing ligands will bind dominantly to the protein, increasing the error in the K_D

determination. As shown in the Figure 3.9(i), when $K_{D,c}$ becomes smaller relative to $K_{D,r}$,

α becomes smaller, which results in an increased error in $K_{D,c}$. A reporter ligand of lower

$K_{D,r}$ would, however, improve the accuracy by again increasing α (Figure 3.9(ii)-(iv)). In

these cases, the time to reach equilibrium increases to between 1 and 3 s (Figure 3.8c-e).

The set of conditions in Figure 3.8d and e is an example that would allow K_D determination
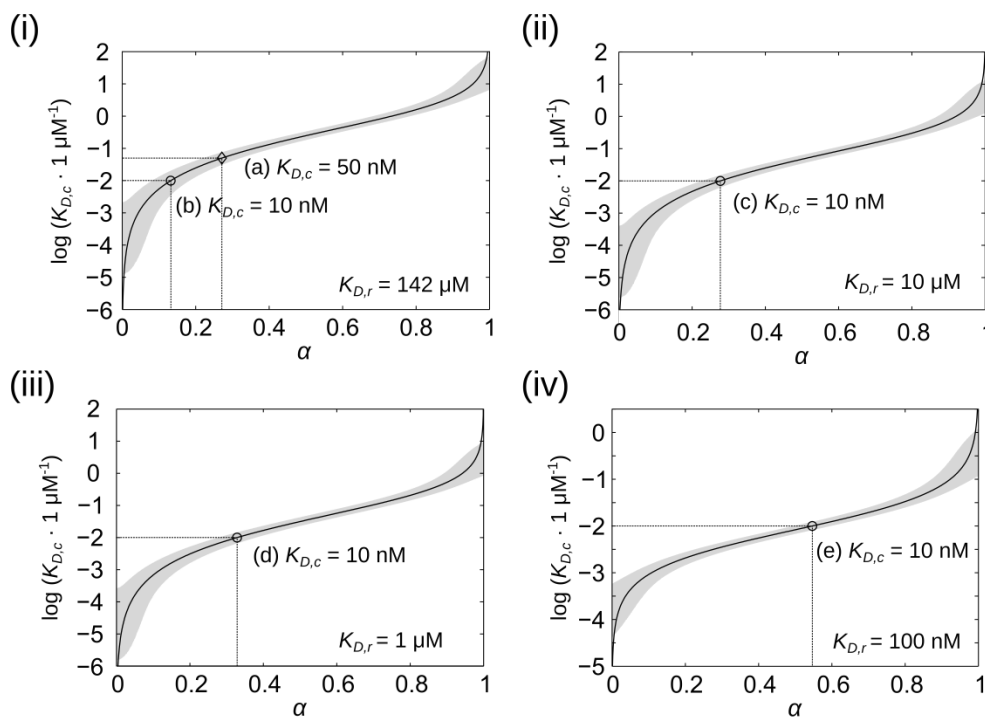
Figure 3.9: Accuracy of $K_{D,c}$ determination depending on the dissociation constant of reporter ligand. The dependence of $\log(K_{D,c})$ on α was simulated, at a given sample concentration for panels (a)-(e) in Figure 3.8. Shaded areas contain 80% of $K_{D,c}$ values, obtained from Monte Carlo simulations carried out as those shown in Figure 3.5.

with similar accuracy as for the data shown in Figure 3.5a, for a ligand of interest with a K_D of 10 nM and an equilibration time of 1 s without prohibitive relaxation losses in the DNP experiments.

3.3.4. Discussion

Whereas in non-hyperpolarized NMR, calibrated peak intensities in single NMR spectra can be used to determine K_D,[44] the single-scan CPMG experiment employed here appears ideal for D-DNP. Data acquisition is completed rapidly, and the measurement of echo intensities does not require narrow spectral lines, simplifying shimming procedures that need to be done prior to sample injection in D-DNP. Unlike many other methods for K_D determination, this experiment also does not require a titration in the case of competitive binding to a single site. For this binding mode, the known $K_{D,r}$ and $p_{b,r}^{(c)}$ provide sufficient information for determination of $K_{D,c}$. More complicated models, such as those involving cooperativity or allosteric interactions, may also be evaluated. The fraction of bound ligand in this case would need to be determined at multiple concentrations.

Since the reporter ligand is in fast exchange between free and bound states, even strongly binding ligands of interest, which can present a challenge in ligand observed screening at excess concentration, are readily identified. For this screening application, throughput could further be increased by using mixtures of putative ligands. For determination of $K_{D,c}$, a single competing ligand should be used together with the reporter, and a kinetic equilibrium is required prior to data acquisition.

Sensitivity and throughput could be further optimized through improvements in solid state polarization and sample injection. Current developments of D-DNP may be applicable, such as using a polarizer with dual center magnet,[156] increasing the magnetic field for polarization[157] or sample transfer,[148] or a multiplexed polarization process.[158] ^{19}F-NMR detection could be improved for increased sensitivity and reduced probe background. A dedicated cryogenically cooled ^{19}F NMR probe at 14.1 T[159] instead of the broadband probe used here at 9.4 T in combination with DNP would itself reduce the limit of detection by at least 7-fold through improvements in noise, NMR coil filling factor and detection field.

3.4.   Conclusions

In summary, making use of the significant signal gain of ^{19}F-DNP NMR, R_2 relaxation rates of a fluorinated reporter ligand obtained from single-scan CPMG experiments were used to determine the dissociation constants of competitive ligands. Monte Carlo simulations can assist in the design of experimental conditions. The DNP based method may be of interest for screening experiments in drug discovery, because ligand binding can be identified and K_D determined, from a single, rapid experiment.

4. PARALLELIZED LIGAND SCREENING USING DISSOLUTION DYNAMIC NUCLEAR POLARIZATION[*]

4.1.   Introduction

Primary challenges for the application of nuclear magnetic resonance (NMR) spectroscopy in the determination of protein−ligand interaction in drug discovery include the achievable sensitivity and throughput.[16,160] These limitations can partially offset the benefits of high resolution and chemical selectivity of this technique. Throughput can be increased by reliance on automation, which routinely permits the unsupervised acquisition of spectra from a large number of samples but remains limited by the signal averaging time. Increases in the NMR sensitivity to reduce the needed acquisition time can be implemented in the form of high-field magnets, cold probe technology or nuclear spin hyperpolarization.[59,161]

A hyperpolarization method amenable to the production of spin-polarized ligand solutions is a technique called dissolution dynamic nuclear polarization (D-DNP).[143] In D-DNP, the hyperpolarization is first achieved in the solid state at a temperature of $1-2$ K, and samples are subsequently dissolved for NMR measurement at room temperature. Signal gains of up to 4 orders of magnitude achieved in a single scan meet or exceed the requirements for detection of difficult targets in the submicromolar concentration range.

Several methods for employing the signal gains from D-DNP for characterizing protein−ligand interactions have been proposed. Among these are the use of direct ^{13}C or

---

^{19}F NMR detection of the hyperpolarized ligands,[144,162] as well as the combination of ligand signal based determination of protein−ligand interactions with long-lived spin states to extend the lifetime of hyperpolarization.[148] Transfer of ligand hyperpolarization via nuclear Overhauser effect to the protein or to a competing ligand can further provide a means to prove binding and potentially characterize the binding site.[163,164] While the latter may already extend beyond the most basic screening application, a parameter that is often of interest in drug discovery is the dissociation constant of the ligand for the protein. Typically, the determination of binding affinities using NMR spectroscopy is achieved by a titration of protein or ligand concentration. In a D-DNP experiment, however, the measurement of each data point requires a new hyperpolarization and sample dissolution step. While it is possible to carry out the titrations using D-DNP,[144] this requirement imposes a new limitation on the achievable throughput. A method to circumvent the need for titrations, based on the relaxation measurement of displaced reporter ligands,[44,145–147] has been recently developed for use with D-DNP in our group.[165] Even in this case, the measurement of relaxation parameters at two or three different concentrations can be desirable. DNP instruments that are capable of polarizing multiple samples have been developed.[158,166] However, even with polarization of a single sample, the amount of hyperpolarized substance generated is often much larger than what can be used in a single experiment. The use of large aliquots of hyperpolarized substance has been recently demonstrated for magnetic resonance imaging (MRI) experiments, where several metabolic experiments were carried out simultaneously.[116]

Here, we describe an implementation of an NMR screening experiment that allows for parallel measurements of competitive protein−ligand interactions using a single

hyperpolarized aliquot injected into separate detection coils located in a high-field NMR spectrometer. We demonstrate the measurement of the ^{19}F spin–spin relaxation rate (R_2) of a hyperpolarized (HP) reporter ligand in the presence of non-HP solutions of protein and inhibitor at different mixing ratios in two channels. These measurements permit the calculation of the dissociation constant K_D in a larger range.

4.2. Experimental section

4.2.1. Two-channel NMR probe

An NMR probe was designed for accommodating two flow cells needed for simultaneous acquisition of relaxometry data (Figure 4.1). The flow cells were manufactured in U-shape by joining borosilicate glass tubing (4 mm outer diameter, 0.5 mm inner diameter) for inlet and outlet with tubing of the same material (5 mm outer diameter, 3.6 mm inner diameter) for the measurement chamber. Inlet and outlet PEEK tubing was inserted into the ends of the flow cells and glued in place using acrylic adhesive. The flow cells were arranged perpendicular to each other in the probe to reduce cross-talk. Flow cells were held by pieces printed from acrylonitrile butadiene styrene (ABS) plastic and assembled on a support frame made of brass. The flow cell supports were designed to allow for modular stacking. A grounded copper foil (0.762 mm thickness) was placed between the cells, in contact with the probe shield, for radio frequency (RF) shielding. Solenoidal RF coils with six turns were directly wound on each cell using a copper wire of 0.812 mm diameter (20 AWG), comprising a detection volume of approximately 100 μL. Due to space constraints, each coil was pretuned close to the ^{19}F NMR frequency (376.4 MHz) with nonmagnetic fixed value capacitors of 1.1 − 1.3 pF (Johanson
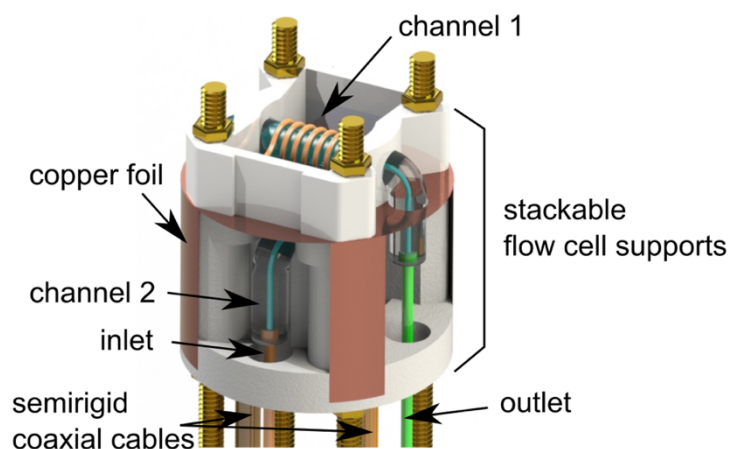
Figure 4.1: Diagram of the two-channel NMR probe. A 6-turn solenoidal coil is wound around a flow cell, pretuned to 376.4 MHz using a fixed capacitor, and connected to a semirigid coaxial cable placed next to the coil end. The flow cells are arranged perpendicular to each other, and a copper foil is inserted between the two coils, to minimize a coupling between the coils. The extended legs of this copper foil are in contact with the probe shield to be grounded. Flow cell supports are stackable, enabling to adjust the location of the coils and to add additional cells.

Technology, Inc., CA). A transmission line (UT-141C semi-rigid coaxial cable, Amawave, Oceanside, CA, inside of the probe, and double-shielded flexible coaxial cable outside of the probe) with a total length of $3\lambda/2 \approx 86.5$ cm connected each coil to a remote tuning circuit outside of the probe.[131] Remote tuning was achieved using variable tuning and matching capacitors of $0.45 - 4$ pF (Voltronics, Salisbury, MD). NMR cross-talk between the two channels was measured by pulsing on, and detecting signal from one channel, which was empty, while the other channel was filled with a solution of 130 mM trifluoroethanol in water.[55] With this method, less than 1% of cross-talk was observed, which was consistent with the value $S_{21} = -34$ dB measured between the coils using a vector impedance analyzer (Model VIA Echo 1000 SF, AEA Technology Inc., Carlsbad,

CA). The NMR probe was located in a standard bore magnet (40 mm accessible diameter within the shim stack) with 9.4 T field strength (Bruker Biospin, Billerica, MA).

4.2.2. Sample preparation

The non-HP sample component was prepared as a solution of 2 or 4 μM trypsin (AMRESCO, Road Solon, OH) and 100 μM or 2 mM of ligand of interest in buffer (50 mM tris(hydroxymethyl)aminomethane, 10 mM KCl, 15 mM trifluoroacetic acid (TFA), pH 8). Benzylamine (TCI, Portland, OR) and benzamidine (Sigma-Aldrich, St. Louis, MO) were the two ligands of interest used in the screening experiments. A volume of 10 μL of HP sample, prepared in a mixture of D_2O/DMSO-d_6 (v/v 1:1), was composed of 4 mM reporter ligand 4-(trifluoromethyl)benzene-1-carboximidamide hydrochloride hydrate (TFBC·HCl; Maybridge, U.K.), 0.88 M KF, and 15 mM 4-hydroxy-2,2,6,6-tetramethylpiperidine-1-oxyl (TEMPOL; Sigma-Aldrich, St. Louis, MO). The concentrations of stock solutions were determined by UV/vis and NMR spectroscopy. TFA and KF were used as reference compounds for non-HP and HP samples, respectively, to evaluate final protein and ligand concentrations in the flow cells using NMR spectroscopy.

4.2.3. Hyperpolarization

Hyperpolarization was generated on ^{19}F spins in a HyperSense DNP polarizer (Oxford Instruments, Abingdon, U.K.) by irradiating with microwaves of 94.055 GHz and 100 mW power, at a temperature of 1.4 K. After 20 min of the polarization, the samples were dissolved in a stream of 4 mL of buffer that had been preheated until a pressure of 5

bar was reached at an approximate temperature of 385 K. Dissolved samples were automatically loaded into the injection loop.

4.2.4. Sample mixing and injection

Figure 4.2 shows the flow paths and accessories used to achieve the sample injection. The non-HP solutions of protein or protein and ligand of interest were preloaded into the separate sections of tubing designed to hold the samples for each channel (t4 and t4', V = 70 μL), before commencing the experiments. Shut-off valves and plugs were used to block the inlets and outlets of these sections. High-pressure syringe pumps (pumps A and B) containing water as a driving fluid started prior to dissolution of the HP sample in preparation for injection, with the fluid directed to a waste line by the injection valves.[167] The samples were injected after the HP sample entered the injection loop (L1, V = 1 mL), which was indicated by an optical detector. At this time, the first injection valve (V1) was switched, and then the second injection valve (V2) after 370 ms to have the HP and non-HP samples push together into the flow cells. Before having the samples enter the probe, the HP sample was split into two streams by a splitter (IDEX Health & Science, Oak Harbor, WA). Each stream passed through a Y-mixer (IDEX Health & Science, Oak Harbor, WA) to which the tubing filled with the non-HP solution was connected, resulting in mixing the HP and non-HP solutions. To prevent back- or cross-flow due to pressure differentials, check valves (IDEX Health & Science, Oak Harbor, WA) were installed on the mixers. The streams leaving the flow cells merged again before connecting to the return port of the V1. This connection held the flow stopped in both cells at the same time after switching of the injection valves. In all the DNP experiments, the pumps A and B

delivered the fluid at the flow rates of 160 and 120 mL/min, which resulted in peak

pressures of 6.8 and 3.0 MPa, respectively. A total delay time of 770 ms allowed for the

samples to arrive in the flow cells. The experimental verification and optimization of the

injection characteristics were performed by recording images of the flow cells using a dye

and measuring NMR signals of the reference compounds after the injection.
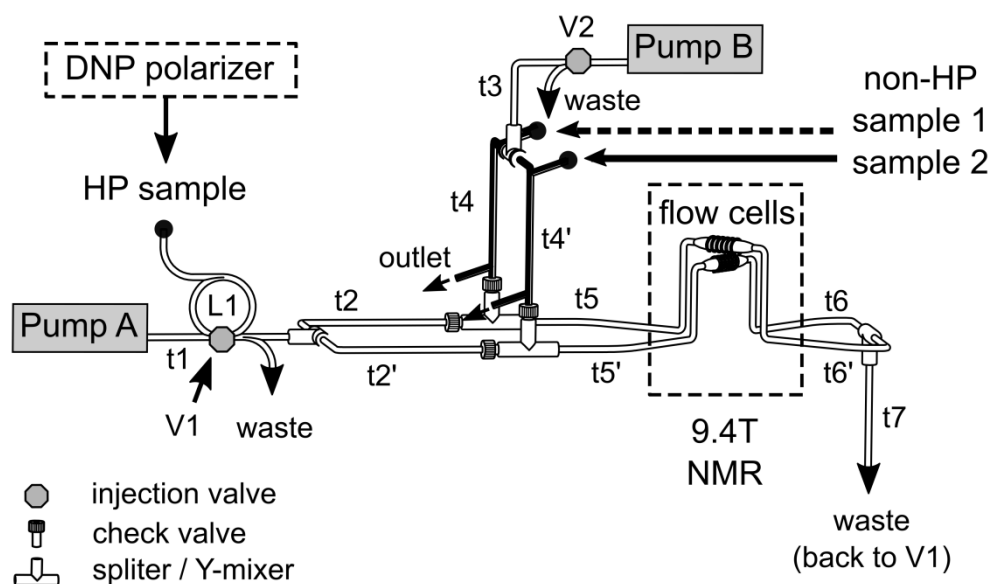
Figure 4.2: Flow path utilized for parallelized measurement of competitive protein–ligand interaction using a single hyperpolarized aliquot of ligand. The HP sample is injected through the sample loop (L1) into the flow path. The tubing (t4 and t4', bold lines) is used to preload two non-HP solutions containing protein and a ligand of interest. The flow path connected to the bottom flow cell is distinguished from the top flow cell by primed notations. The tubing connections to the two flow cells are symmetric. Tubing length: t1: 152.4 cm; t2: 20 cm; t3: 23 cm; t4: 15 cm; t5 and t6: 60 cm; t7: 170 cm. L1: 50 cm. Tubing inner diameter: t1, t2, t3 and t5: 0.02"; t4, t6 and t7: 0.03".

4.2.5. NMR experiments

For the NMR experiments, a home-built multiplexing NMR spectrometer for ^{19}F detection was utilized. The spectrometer consisted of the RF generator and processing boards (SpinCore Technologies, Gainesville, FL). The RF signal was amplified by a power amplifier (model BT00250 Gamma, Tomco Technologies, Stepney, South Australia) before it was split and fed into both coils. The NMR signal from each channel was received separately. The NMR experiments were started 400 ms after having the flow of fluids stopped by switching the injection valves. The experiments employed a Carr Purcell Meiboom Gill (CPMG) pulse sequence,[31] where a train of spin–echoes were acquired using $p1 - \tau - [p2 - 2\tau]_n$. Here, p1 is an excitation pulse with flip angle $\pi/2$ and phase x, p2 is a π pulse of phase y, $\tau = 4$ ms and $n = 860$. A total of 280 complex data points was taken for 7 ms in the 2τ period indicated in the pulse sequence, resulting in a 40 kHz spectral width. Pulse strengths were $\gamma B_1/(2\pi) = 45.5$ kHz using 51.2 W forward power split equally on Channels 1 and 2 (top and bottom coils, respectively, shown in Figure 4.2). In this experiment, the transmitter offset frequency was set to the middle of the TFBC frequencies in Channels 1 and 2 due to a slight difference in magnetic fields at the two coils. The receiver frequency was set to the center of the TFBC and KF frequencies. After the decay of the hyperpolarization, a one-pulse NMR experiment was performed using 36 scans to determine the concentrations of the reference compounds.

4.2.6. Data analysis

For the data processing, each complex valued spin–echo was multiplied by a sine-squared window function with the center of the echo set to $t = 0$, and Fourier transformed into a frequency-domain spectrum. A pure absorption spectrum was obtained for both the real and imaginary parts due to the time symmetric nature of the signal. The phase shift was corrected to maximize the real component while minimizing the imaginary one (Figure 4.3).
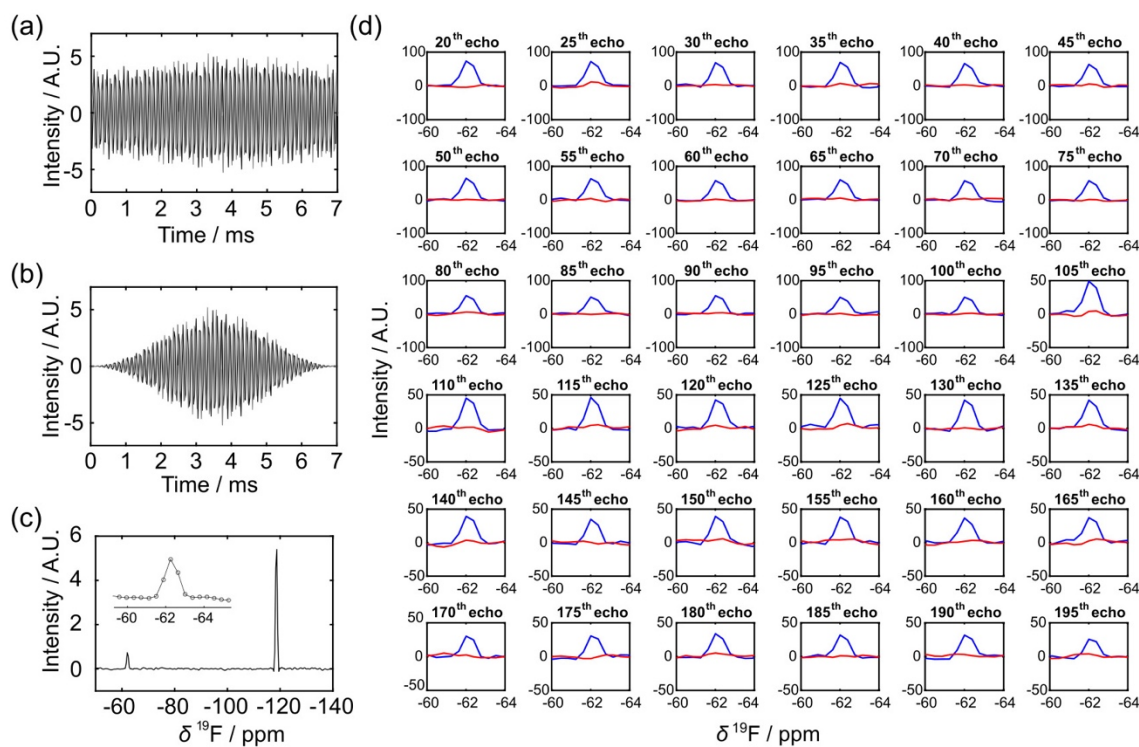
Figure 4.3: Data processing of spin–echo signals. (a) Real part of spin–echo from the CPMG experiment of hyperpolarized TFBC and KF. (b) Spin–echo apodized with a sine-squared window function. (c) Resulting frequency-domain spectrum after Fourier transformation (the inset shows the digital resolution of 0.38 ppm/point). (d) The spectra of successive spin–echoes were properly phased to maximize the real and minimize the imaginary components, shown in blue and red, respectively. The same phase parameters were applied to all spectra.

Signal intensities were measured from the spectrum of each echo, and subsequently used for R_2 determination by exponential fitting. Only the spectra after 160 μs (840 spectra) were used to avoid fluctuations arising during the sample settling immediately following the injection.

Under fast exchange, R_2 of free and bound ligands ($R_{2,f}$ and $R_{2,b}$, respectively) contribute to the overall R_2 depending on the relative populations. An additional increase in the overall R_2 can occur due to chemical exchange unless the chemical shift difference between the free and bound states is negligibly small when compared to the exchange rate.[168] If the fraction of bound ligands (p_b) is assumed to be small that $(1 - p_b)^2 \approx 1$, its effect on the overall R_2 is proportional to p_b. By using a reversible inhibitor of trypsin, TFBC ($K_D = 142$ μM[144]) as a reporter ligand and keeping $p_b < 0.005$ in all the experiments, the error in the exchange contribution due to the approximation was less than 1%. In the presence of protein and reporter ligand under binding without competition, p_b is given by Equation (1.2)[22] When the reporter ligand is competing with the ligand of interest, p_b is given by Equation (4.1),[169] additionally depending on the total concentration of the ligand of interest $[C]_t$ and its dissociation constant $K_{D,c}$.

$$p_b = \frac{2\sqrt{(a^2 - 3b)}\cos(\theta/3) - a}{3K_{D,r} + 2\sqrt{(a^2 - 3b)}\cos(\theta/3) - a} \tag{4.1}$$

where

$$\theta = arcos\left[\frac{-2a^3 + 9ab - 27c}{2\sqrt{(a^2 - 3b)^3}}\right]$$

$$a = K_{D,r} + K_{D,c} + [R]_t + [C]_t - [P]_t$$

$$b = K_{D,c}([R]_t - [P]_t) + K_{D,r}([C]_t - [P]_t) + K_{D,r}K_{D,c}$$

$$c = -K_{D,r}K_{D,c}[P]_t$$

$[P]_t$ and $[R]_t$ are, the total protein and reporter ligand concentrations, respectively, and $K_{D,r}$ is the dissociation constant of the reporter ligand.

To determine $K_{D,c}$ from the competitive binding experiments, the reference parameter $R_{2,f}$ was measured from the CPMG experiments of free hyperpolarized TFBC, and $R_{2,b}{}^*$, which corresponds to $R_{2,b} + (2\pi\Delta v)^2/k_{off}$ in Equation (1.5), was obtained by fitting the observed R_2 relaxation rates ($R_{2,obs}$) of hyperpolarized TFBC in the presence of trypsin at different concentrations to Equation (1.5). The total protein and ligand concentrations were determined based on the signal intensities of the reference compounds in the flow cells measured after the hyperpolarized experiment (Figure 4.4).
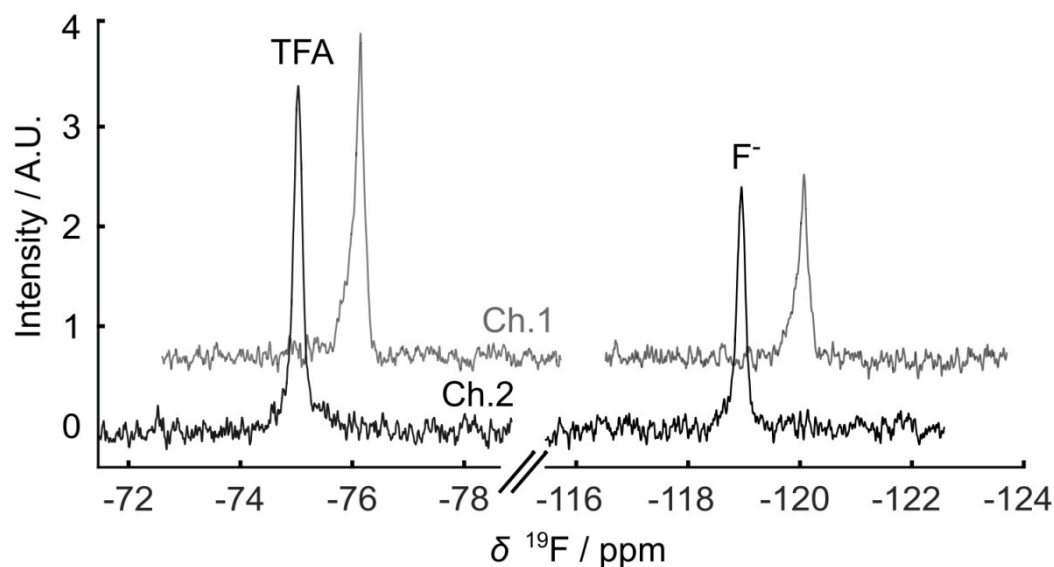
Figure 4.4: Examples of ^{19}F NMR spectrum acquired under thermal condition after CPMG experiments. Each spectrum is an average of 36 scans. The signals of reference compounds, TFA ($\delta = -75.0$ ppm) and F$^-$ ($\delta = -118.7$ ppm) were used to quantify the final concentrations of hyperpolarized and non-polarized samples in the flow cells. The top and bottom spectra were obtained from Channels 1 and 2, respectively.

The $K_{D,c}$ value was calculated first by obtaining the value of p_b using the fitted $R_{2,obs}$ from the CPMG experiments, and then by solving equations for the binding equilibrium for each channel individually.[165] Alternatively, the $K_{D,c}$ value was determined by fitting to the CPMG datasets from both channels at the same time. For this purpose, the decay rate of $R_{2,obs}$ was expressed as a function of p_b given by Equation (4.1), and a single value of optimized $K_{D,c}$ was obtained by minimizing the sum of squared residuals of the predicted values and the measured data from Channels 1 and 2.

The $K_{D,c}$ value is subject to the errors associated with the determinations of the values for the relaxation rates and the concentrations of proteins and ligands. This error was estimated using a Monte Carlo method. For each CPMG dataset, 10^5 simulated groups of data were created, comprising normally distributed, randomized parameter values for $R_{2,f}$, $R_{2,b}^*$, $R_{2,obs}$, $[P]_t$, $[R]_t$, and $[C]_t$. For $R_{2,f}$ and $R_{2,b}^*$, averages and standard deviations were obtained from the separate CPMG experiments. The distribution of $R_{2,obs}$ was based on the fitted value and fitting error $E_{R_{2,obs}}$. The concentration values were used as determined from the NMR measurements and associated with an estimated 5% error. $K_{D,r}$ was a constant. Since, at the competitive equilibrium, the measured decay rate should be between the rate of free reporter ligand and that under binding without competition, combinations with $R_{2,obs}$ values that are closer than $E_{R_{2,obs}}$ to those limits were discarded. From the remaining groups of parameters, the resulting distribution of $K_{D,c}$ was calculated. All data analysis was conducted using the Matlab program (MathWorks, Natick, MA).

4.3.   Results and discussion

Two simultaneously acquired single-scan CPMG datasets using the hyperpolarized TFBC as a reporter ligand are shown in Figure 4.5. Here, the ligand of interest, benzylamine, was added to the protein solution in two different proportions. The ratios were chosen to enable the detection of competitive binding over a range of $K_{D,c}$ of at least an order of magnitude. The hyperpolarized reporter was admixed during the sample injection at a nominally equal ratio with respect to the protein. Each spectrum shown in the figure was obtained from an average of 20 successive spin–echoes acquired
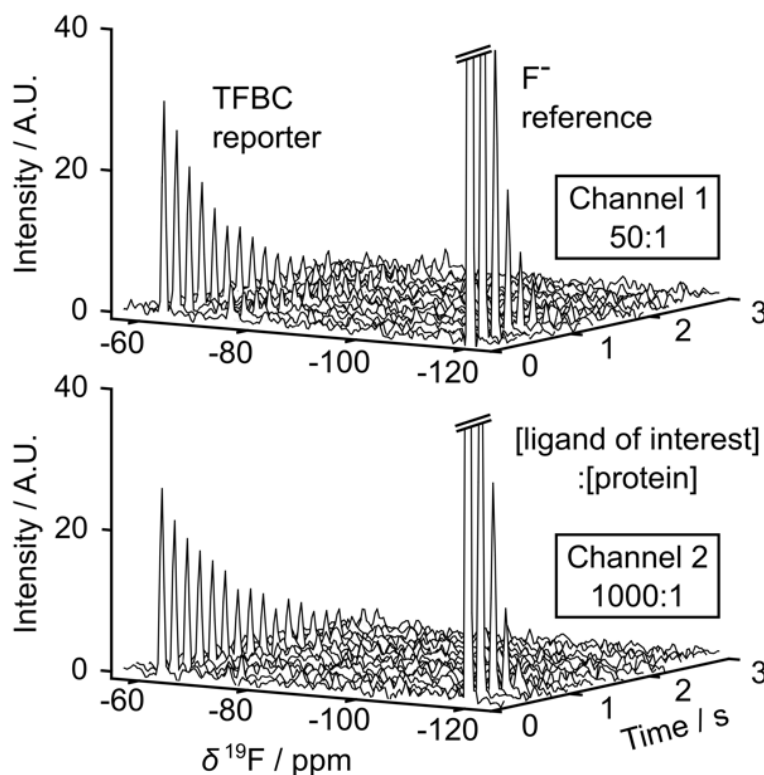
Figure 4.5: Single-scan CPMG spectra of hyperpolarized TFBC ($\delta = -62.4$ ppm) and reference compounds, KF ($\delta = -118.7$ ppm) and TFA ($\delta = -75.0$ ppm) in the presence of 23.1 μM TFBC, 0.31 μM trypsin, and 15.6 μM benzylamine (top, Channel 1), and 18.3 μM TFBC, 0.26 μM trypsin, and 258 μM benzylamine (bottom, Channel 2). For presentation only, each spectrum shown represents the average of 20 acquired spectra.

from the CPMG pulse train, thus indicating the time dependence of echo intensity due to R_2 relaxation. With the inclusion of a single fluorinated site in the sample mixture, the echo signals in the absence of spectral resolution would in principle suffice to determine the relaxation rate. However, the spectra shown in the figure permit distinguishing the signals of the reporter TFBC at $\delta = -62.4$ ppm from those of reference compounds, F^- and TFA. TFA was not hyperpolarized and yielded signals close to the noise level, and an NMR cross-talk signal was not observed despite a signal enhancement of over a thousand-fold. The signal decay of the reporter is dependent on the fraction of protein-bound reporters. A slower relaxation in Channel 2, due to increased displacement of bound reporters in the presence of 20 times more of benzylamine, is clearly visible.

The time dependence of the signals of TFBC competing with benzylamine, as well as in separate datasets competing with benzamidine, is shown in Figure 4.6. Additional repetitions are included in Figures A.3 and A.4. The noise appears larger than in the spectra in Figure 4.5 because the peak intensity from each echo was plotted without averaging in Figure 4.6. In order to assess the binding affinity of the competing ligand, a measurable change in the population of bound reporters is required. This change can be quantified by comparing the difference between $R_{2,obs}$ and $R_{2,f}$ to that of the limiting values of $R_{2,f}$ and $R_{2,obs}$ in the absence of competition. It was previously shown that the ratio of these differences, here designated as α, is equal to the ratio of p_b under competitive binding to that under binding without competition.[165] In Figure 4.6, it is apparent that the $R_{2,obs}$ values from Channel 1 with benzamidine (Figure 4.6a) and Channel 2 with benzylamine (Figure 4.6d) appear midway between the two limits, which is reflected by the values of α close to 0.5. This indicates a partial displacement of the bound reporters due to binding
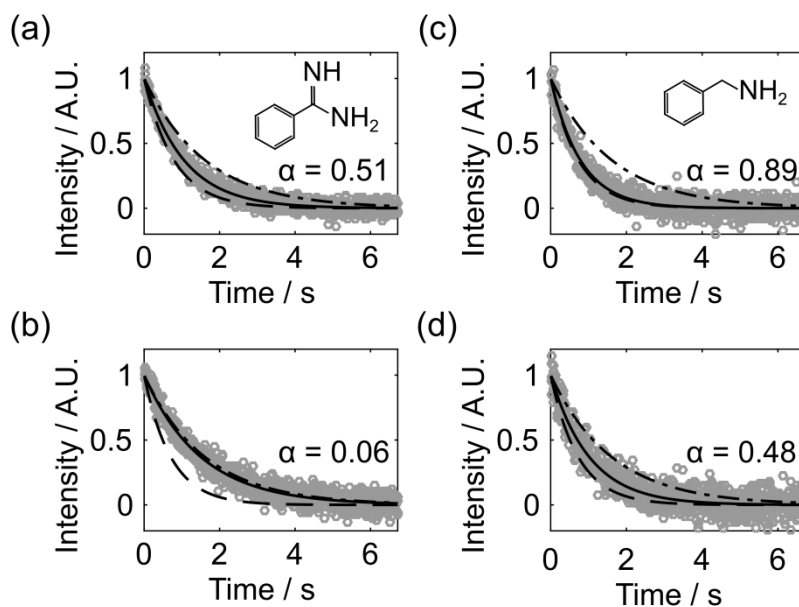
Figure 4.6: R_2 relaxation decays of hyperpolarized TFBC competing with benzamidine (a and b) and benzylamine (c and d) obtained from the CPMG experiments. The first row (second row) displays the data acquired from Channel 1 (Channel 2). The maximum intensities of TFBC signals from 840 successive echoes are denoted by gray circles. The fitted $R_{2,obs}$ curves are indicated by solid lines. Signal decays of R_2 limiting curves corresponding to free TFBC ($R_{2,f}$ = 0.62 s^{-1}) (– - –) and maximally bound TFBC, calculated from $R_{2,b}{}^*$, (– –) are indicated. The α value shown in each graph reflects the ratio of p_b with respect to p_b in the absence of competition. The values of sample concentrations and fitted $R_{2,obs}$ are summarized in Tables A.2 and A.3.

competition. The other two datasets either show almost complete (Figure 4.6b) or almost negligible displacement (Figure 4.6c), indicated by the value of α close to zero or unity, respectively. The most accurate $K_{D,c}$ can be obtained when 50% displacement occurs, that is, $\alpha \sim 0.5$.[22,165] Hence, the multiplexed detection in both cases includes one set of concentrations expected to allow for reliable determination of $K_{D,c}$.

The limiting value of $R_{2,obs}$ for each dataset was calculated using the values of $R_{2,f}$ = 0.62 ± 0.01 s^{-1} (Figure A.1), and $R_{2,b}{}^*$ = 388 ± 33 s^{-1} and 464 ± 34 s^{-1} for Channels 1 and 2, respectively (Figure A.2 and Table A.1). The difference in $R_{2,b}{}^*$ of the two channels

may be attributed to different RF-pulse (B_1) field distributions of two coils and main field (B_0) inhomogeneity. For $K_{D,c}$ determination, here, an individual $R_{2,b}^*$ value was therefore applied to the data from each channel, but this difference could possibly be alleviated by using compensated spin–echo pulse sequences.[170–172]

The measurement of datasets at two concentrations for each inhibitor allows for the possibility to fit a single $K_{D,c}$ parameter that minimizes residuals to both datasets or, alternatively, to analyze each dataset separately. Values for $K_{D,c}$ obtained by the two methods are shown on a logarithmic scale in Figure 4.7. Those by the group fitting are
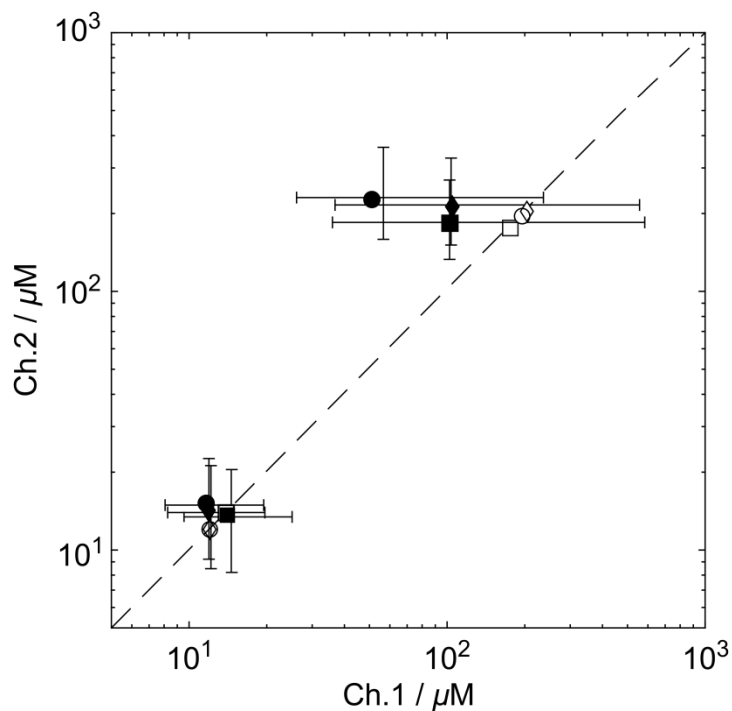
Figure 4.7: Numerical values of $K_{D,c}$ of benzamidine (lower left cluster) and benzylamine (upper right cluster) determined from three trials ('◊','□','○'). Those obtained by the individual fitting are indicated using closed symbols. The error bars indicate the intervals containing 95% of the $K_{D,c}$ values simulated using Monte Carlo method. The empty symbols on diagonal represent the $K_{D,c}$ values obtained by the group fitting. All the values are summarized in Tables A.4−A.5.

plotted using open symbols and those by the individual fitting using closed symbols. The horizontal and vertical coordinates of the closed symbols represent the $K_{D,c}$ values determined by the individual fitting for Channels 1 and 2. These values deviate from the diagonal, which indicates that the $K_{D,c}$ values from the two channels are different. Presumably, due to the nonoptimal value of α, the resulting $K_{D,c}$ for benzylamine from Channel 1 is underestimated.

To further assess the source of errors in $K_{D,c}$, propagation due to uncertainty of the measured parameters were analyzed using Monte Carlo simulations. A source of error would be due to concentration variations between the different injections, which were found to be within approximately 10%. The accuracy of concentration values was, however, increased to 5% by determining the final concentrations using a one-pulse reference experiment after the decay of the hyperpolarization. Other sources of errors were determined, as described in the Data analysis. The result from the Monte Carlo simulations is indicated with horizontal and vertical bars at a confidence level of 95% for the resulting $K_{D,c}$ values from Channels 1 and 2. As expected, the errors evaluated for the $K_{D,c}$ values of benzylamine from Channel 1 were greater than those from Channel 2, where α was close to the optimal value. When a dataset with near optimal α is available, generally, the individual fitting results in a more accurate $K_{D,c}$, as shown by the error ranges. For these more optimal cases, the confidence intervals of benzamidine (Channel 1) and benzylamine (Channel 2) determined from a single dataset were typically (8.3 μM, 20 μM) and (151 μM, 328 μM), respectively. The average $K_{D,c}$ values over the three separate experiments were 12.6 ± 1.4 and 207 ± 22 μM, respectively, where the ranges indicate standard deviation. The spread of values reflected in these standard deviations is consistent with

the confidence intervals for the single measurement calculated above. The average $K_{D,c}$ values are also in good agreement with previously reported values (benzamidine, 16 ± 2 μM; benzylamine, 218 ± 43 μM at 50 mM Tris, pH 8.0, 304 K).[165] Figure 4.7 further indicates that for the datasets obtained here, the group fitting method (open symbols) provided values of $K_{D,c}$ located within the confidence intervals of the individual fits, close to the individual values of the more accurate channel. If the datasets comprise no optimal sets of concentrations, the group fitting may be applied effectively to obtain a more reliable $K_{D,c}$ value.

Using the described multiplexing DNP-NMR system, two ligands of interest that have binding affinities differing by an order of magnitude were successfully screened without changing the experimental conditions. The use of two channels broadens the target range of $K_{D,c}$, reducing the possibility of missing the detection of binding due to nonoptimal concentrations. One experiment taken to obtain a $K_{D,c}$ value required less than 25 min. Most of the time was used for achieving the hyperpolarization, while only a few minutes were required to prepare the dissolution by using the flow system, which obviates the steps of cleaning and loading NMR tubes between the sequential dissolutions. Considering that multiple experiments are often desired to obtain a reliable K_D value, the overall experimental time can be reduced by 2-fold owing to the capability of the parallelization. Besides simplifying the procedures, the flow system allows for achieving a wide range of volume ratios of non-HP to HP samples by adjusting the injection parameters. This ratio can be 1:1 or higher, which is not attainable with the gas-driven injection, where the volume of the secondary sample preloaded into the NMR tube is limited to about 10% of the final injection volume.[102] Therefore, when injecting into the

flow cell, the protein samples can be prepared less concentrated, avoiding protein aggregation or solubility issues. One drawback of this flow system is, on the other hand, a relatively low sample recovery fraction compared to the gas-driven injection method, likely caused by distribution in the tubing due to laminar flow. Here, the mass fraction of non-HP sample recovered was 20%, and the amount of HP sample was 5% in each flow cell. Sample recovery may be increased in the future by using a driving fluid that is immiscible with the samples.[173] The latter number also indicates that the DNP polarizer has a capacity of polarizing a larger amount of sample than what is needed for the typical binding experiment. Adding several additional coils to the NMR probe could provide further time savings. Despite the use of multiple coils, the delivery of the sample required no more than two high-pressure pumps, for the HP and non-HP components, respectively. Using additional flow splitters, a larger number of cells could be filled without requiring additional pumps that would result in further expense and complexity.

Apart from the determination of $K_{D,c}$ as shown here, the ability to parallelize experiments would also be useful for other applications requiring titrations. For example, this design could be used to investigate inhibitors with allosteric properties, the importance of has have been highlighted in drug design among others targeting kinases.[174,175]

4.4.   Conclusions

In conclusion, we have demonstrated a parallelized screening method using a multiplexing ^{19}F NMR probe and spectrometer in combination with D-DNP. This method to acquire R_2 relaxation rates from a single hyperpolarized aliquot of reporter ligands mixed with two different ratios of ligands of interest to target proteins can reduce the total

experimental time and extend the detectable range of $K_{D,c}$ in a single scan. Since the affinity range of putative ligands is often unknown, the applicability of D-DNP NMR in drug discovery can be improved by the multiplexed screening experiments shown here.

5. DETERMINATION OF BINDING AFFINITIES USING HYPERPOLARIZED NMR WITH SIMULTANEOUS 4-CHANNEL DETECTION[*]

5.1. Introduction

Advances in hyperpolarization, including using the methods of dissolution dynamic nuclear polarization (D-DNP)[76,143] or parahydrogen induced polarization (PHIP)[68,176] hold promise to improve the capabilities of liquid state NMR spectroscopy for chemical analysis. These techniques lower the limits of detection by orders of magnitude, thereby providing access to conditions, where otherwise prohibitive signal averaging would be required.[177,178] The time requirements for preparing hyperpolarized (HP) samples, however, partially offset these gains for routine applications. In particular, quantitative problems frequently require the acquisition of multiple spectra in function of a variable parameter. For example, titrations are commonly used for the determination of binding affinities such as between proteins and ligands in drug discovery.[160] They are applied to the measurement of equilibrium constants in complex molecules, such as the protonation or deprotonation of amino acid side chains accompanied by a structural change in a protein,[179] or in combination with relaxation measurements for the characterization of dynamic changes that occur due to intermolecular interactions.[32–34]

These problems require multiple data acquisitions, resulting in increased complexity for the application of hyperpolarization protocols that include several additional preparation steps. For D-DNP, hyperpolarization itself may require microwave

irradiation for a duration of on the order of tens of minutes to hours, in addition to mechanical steps for sample loading and dissolution.[79] High throughput D-DNP NMR has been proposed with the construction of instrumentation that can polarize multiple sample aliquots at the same time, followed by sequential dissolution.[158,166,180,181] Experiments may also be facilitated by developing NMR pulse sequences and data analysis techniques that reduce the number of required repetitions for a specific problem. Authors of this publication have previously developed such methods for the characterization of protein-ligand interactions, employing relaxation measurements of a reporter ligand.[165] These methods were subsequently applied in combination with a purpose developed NMR probe, which allowed the simultaneous measurement of two relaxation traces from a single HP aliquot.[182]

Here, we demonstrate that up to four simultaneous measurements of concentration-dependent relaxation data can be achieved with a probe designed to fit into a standard narrow-bore magnet, and a spectrometer with a split excitation channel capable of applying the same pulse sequence on each channel. Using the protein trypsin in combination with several ligands, we show that binding affinity can be determined over a range of three orders of magnitude in a single experiment. Finally, we include a detailed analysis of the accuracy of the method and discuss applicability to multi-scan NMR in general.

5.2. Materials and methods

5.2.1. Four-channel NMR detection

A four-channel NMR spectrometer for ^{19}F detection was built on four radio frequency (RF) generation and processing boards, one of which was a RadioProcessor^{TM} (RP), and the others were receiver-only RP (RP-RX) boards (SpinCore Technologies, Gainesville, FL). The RF signal generated from the only excitation channel (RP) was first amplified by a power amplifier (model BT00250 Gamma, Tomco Technologies, Stepney, South Australia). The amplified RF signal was then fed into power splitters (model ZA2CS-62-40W+, Mini-Circuits, Brooklyn, NY) where four RF outputs were produced and transmitted to the four coils in the probe. In the receiver part, all four boards were utilized, receiving the induced NMR signals separately.

The multiplexed NMR probe, accommodating four flow cells, was designed to fit into a standard narrow-bore magnet (40 mm accessible diameter within the shim stack). The probe expands on a previous two-channel design.[165] Briefly, U-shaped flow cells of 100 μL volume were stacked within 35 mm of vertical space with a center-to-center distance of 8 mm (Figure 5.1). Solenoidal RF coils, wound around the flow cells, were arranged orthogonally to each other to reduce cross-talk, and grounded copper sheets (0.55 mm thickness) were inserted in-between for RF shielding. Each coil was tuned to the ^{19}F NMR frequency at 9.4 T (376.4 MHz) by using a remote tuning and matching circuit.[17] The cross-talk between individual channels was measured by applying a radio-frequency pulse to, and acquiring NMR signal from a channel that was empty, while one of other three channels was filled with a solution of 130 mM trifluoroethanol (TFE). The channels that were not involved in the measurement were terminated with 50 ohms. With this

method, 1-5% cross-talk was observed between neighboring channels. The cross-talk from

non-adjacent coils was less than 1%.
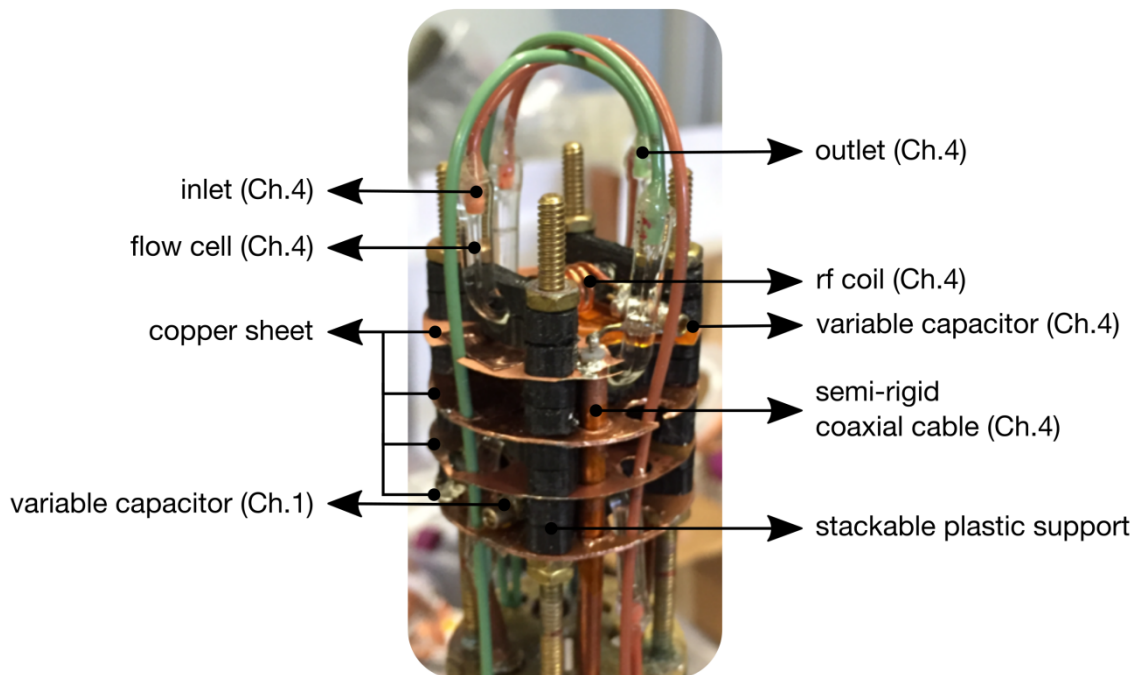
Figure 5.1: Probe head inside the four-channel NMR probe. A 4-turn solenoidal coil is wound around each flow cell, pre-tuned to 376.4 MHz using a variable capacitor, and connected to a semi-rigid coaxial cable placed next to the coil end. The flow cells are arranged perpendicular to each other, and copper sheets are inserted between the coils to minimize cross-talk. The copper sheets are in contact with the probe shield for grounding. Flow cell supports are stackable, enabling to adjust the location of the coils and to add additional cells.

5.2.2. Sample preparation

A solution of 10 mM 4-(trifluoromethyl)benzene-1-carboximidamide hydrochloride dihydrate (TFBC·HCl·2H$_2$O; Matrix Scientific, Columbia, SC) for hyperpolarization was prepared in a mixture of D2O/DMSO-d6 (v/v 1:1) with 30 mM 4-hydroxy-2,2,6,6-tetramethylpiperidine-1-oxyl (TEMPOL; Sigma-Aldrich, St. Louis, MO).

Non-HP samples contained 5 μM trypsin (AMRESCO, Road Solon, OH) in buffer (50 mM Tris, 10 mM $CaCl_2$, 50 mM trifluoroacetic acid (TFA), pH 8). The compound TFA was used as an internal reference to evaluate the dilution factor (DF) of the non-HP sample component in the final solution. For the measurements of concentration-dependent relaxation data, solutions of 37.5, 375, 1875, and 3750 μM benzylamine (TCI, Portland, OR) and benzamidine (Sigma-Aldrich, St. Louis, MO) were prepared with 5 μM trypsin in the same buffer. The concentrations of stock solutions were determined by UV/Vis and NMR spectroscopy.

5.2.3. Hyperpolarization

A 10-μL aliquot of TFBC sample was loaded into a HyperSense DNP polarizer (Oxford Instruments, Abingdon, U.K.) operating at 1.4 K. Hyperpolarization on ^{19}F spins of the sample was achieved by microwave irradiation of 94.055 GHz and 100 mW power for 20 min. After being dissolved in a degassed buffer (50 mM Tris and 10 mM $CaCl_2$ at pH 8), pre-heated to approximately 385 K, the sample was injected into the flow cells through a flow path described in the following section.

5.2.4. Simultaneous sample mixing and injection

The flow path was designed to split a single stream of HP sample into four substreams. Each substream was mixed with another reagent individually before filling the flow cells, as depicted in Figure 5.2. For flow injection, high-pressure syringe pumps (Pump A; 500D and Pump B; 1000D Teledyne Isco, Lincoln, NE) were enabled before the dissolution of a hyperpolarized sample. A steady liquid pressure was achieved by
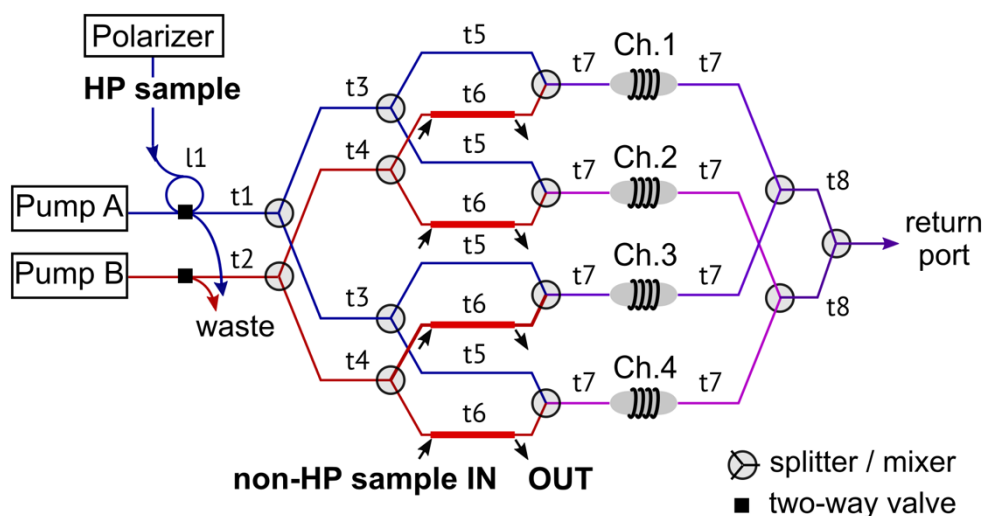
Figure 5.2: Flow path designed for simultaneous injection of four hyperpolarized samples into NMR flow cells. Non-HP reagents are independently admixed to each channel. t1: 152cm, t2:15 cm, t3 and t4: 5cm, t5: 12cm, t6: 20cm, t7: 65cm, and t8: 15cm.

flowing water through an open path to waste (see figure). Nominal flow rates were 160 and 150 mL/min for pump A and B, respectively. Following dissolution, the HP sample arrived in the sample loop (l1), the injection valve (v1) was switched and the HP sample was driven to flow into the splitters. After 400 ms, the second valve (v2) was switched, allowing the non-HP samples to flow and admix to the HP samples. After running simultaneously for 500 ms, both pumps were stopped. The NMR measurement began after 400 ms of sample settling time.

The non-HP reagents including protein or protein and ligand of interest were manually filled into the separate sections of tubing (t6, V = 40 μL) before the start of the dissolution. The inlets and outlets of these sections were blocked using shut-off valves and plugs to hold the samples for each channel during the operation of Pump A. At every junction, Y-mixers (IDEX Health & Science, Oak Harbor, WA) were used, and check

valves (IDEX Health & Science, Oak Harbor, WA) were installed to prevent back- or cross-flow.

The amount of sample delivered to the flow cells was estimated by measuring DF of reference compounds from one-pulse NMR measurements. The DF for HP samples was found from multiple test measurements where a solution of 50% TFE was loaded into the DNP polarizer. The pre-determined DF values were then used to estimate the concentrations of HP samples in four channels in the actual ligand binding experiments. The non-HP samples contained TFA in all experiments. The concentrations of protein or competitive ligand were obtained from every injection based on the TFA signals. The DF determined from the individual channels averaged 450 ± 32 and 7.8 ± 1.0 for HP and non-HP samples, respectively, with less than 10% variations in each channel as summarized in Table 5.1. A comparison between the DF from the four channels showed 20% and 35% variations for HP and non-HP samples, respectively, which were taken account of in error analysis.

Table 5.1: Sample dilution factors measured for HP and non-HP samples after injection into the flow cells.

	Ch. 1	Ch. 2	Ch. 3	Ch. 4	Average
HP sample	489 ± 40	439 ± 37	414 ± 28	455 ± 44	450 ± 32
Non-HP sample	8.1 ± 0.6	9.1 ± 0.5	6.8 ± 0.2	7.3 ± 0.3	7.8 ± 1.0

5.2.5. NMR spectroscopy

For four simultaneous measurements of transverse relaxation rate (R_2), a chemical shift resolved spin relaxation measurement was implemented using a Carr Purcell Meiboom Gill (CPMG) pulse sequence.[31,182] As shown in Figure 5.3, the RF pulses were generated from the single excitation channel split to feed the four coils in the probe. Spin echo signals arising from the sample were received in separate receiver channels. A total of 860 spin echoes were acquired from each channel. Each echo was composed of 280 complex data points collected for 7 ms during the interpulse delay $2\tau = 8$ ms. The excitation pulse was set to 13.5 µs, which was the average of 90° pulse lengths measured to be 13, 13.5, 13 and 14 µs from four channels, at a pulse power of 9.1 W ± 3% per channel. The transmitter offset frequency was set to the center frequency of the TFBC signals obtained from the four channels, as a slight difference in magnetic fields was present between the sample locations. In the one-pulse measurements for determining the EF of the injected samples in the flow cells, 32 scans of ^{19}F NMR spectra were measured using a 90° pulse after the hyperpolarization was lost. The measured signal intensities
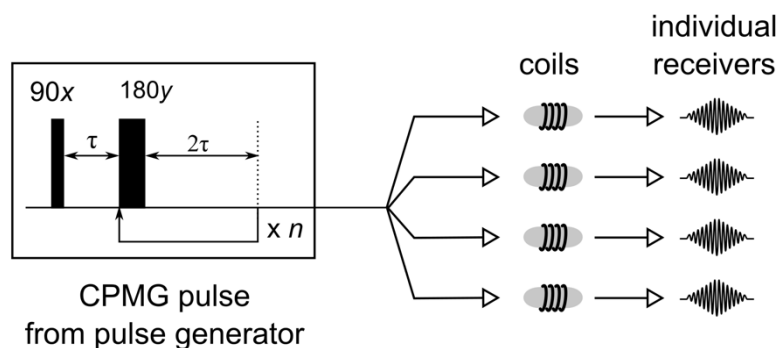
Figure 5.3: Schematic of pulse transmission and signal reception for simultaneous NMR measurements with multiple channels. A CPMG pulse sequence employed for R_2 relaxation measurement is shown.

were converted to the sample concentrations based on the calibration curves obtained from the individual channels.

5.2.6. Data analysis

Spin-echo signals from the relaxation measurements were processed by first applying a sine-squared window function with the center of the echo set to $t = 0$. After a complex-valued Fourier transformation, the spectra were phase corrected to minimize the imaginary part. Signal intensities, integrated over the signal range in the spectra, were fitted to a single exponential decay function to find a R_2 relaxation rate.

An increase in the R_2 relaxation rate of a ligand in the presence of protein reflects the ligand binding. When the ligand is in fast exchange with respect to the R_2 relaxation, the observed R_2 relaxation rate ($R_{2,obs}$) is determined by Equation (1.4)[24] Under the condition that $(1- pb)^2 \approx 1$, $R_{2,obs}$ becomes linearly related to pb as expressed in Equation (1.5). When the ligand competes with another ligand for the same binding pocket in the protein, the system shifts to a new equilibrium, resulting in a change in pb and therefore $R_{2,obs}$. The equation for pb under binding competition can be written in terms of protein and ligand concentrations and binding affinities of the two ligands.[169] In our experiments, TFBC was a reporter ligand whose K_D was known as 142 μM at pH 8.[144] Using the equations given in ref. 169 and knowledge of $R_{2,f}$, $R_{2,b}^*$ ($R_{2,b}^* = R_{2,b} + (2\pi\Delta v)^2/k_{off}$ in Equation (1.5)), as well as the concentrations of protein and ligands, the K_D of a competing ligand was found from four $R_{2,obs}$ values measured in one experiment.

5.3. Results and discussion

5.3.1. Concentration-dependent R_2 measurements

The experiments utilized hyperpolarization of ^{19}F spins of a reporter ligand to evaluate the binding affinity of a ligand of interest based on transverse relaxation rates (R_2) of the reporter ligand under the competitive binding. Figure 5.4 shows the concentration-dependent relaxation data obtained from the four simultaneous relaxation measurements performed with the multi-channel DNP-NMR. The hyperpolarized reporter ligand TFBC was injected into the four channels after mixing with the protein trypsin and known inhibitor benzamidine.[165] Trypsin was at a nominally equal concentration in each channel, whereas the concentration of benzamidine increased from the channel 1 to 4. The first 50 spin-echoes acquired from the four channels are shown in Figure 5.4a. Among the four echo trains, the signals from the channel 1 exhibit the fastest decay. The channels with higher numbers show a reduced signal decay rate due to a higher concentration of benzamidine, the ligand for which K_D was intended to be determined by the experiment, and which displaces the reporter ligand from the binding site. As seen from the graph in Figure 5.4b, the benzamidine concentrations varied from 1- to 10-, 50-, and 100-fold dilution of a 0.5 mM solution, and the average concentration of trypsin was 640 nM with a variation of 10% across the channels. The averaged concentration of reporter ligand in four channels was 22.3 μM. From the contour plots of Fourier-transformed frequency spectra shown in Figure 5.4c-f, the effect of benzamidine on the signal decay rates of the reporter ligand can be seen more clearly. The signal in each spectrum originates from the reporter ligand under fast exchange between the free and bound forms. Using an exponential fit to these signal intensities, the observed relaxation rate constant ($R_{2,obs}$) for
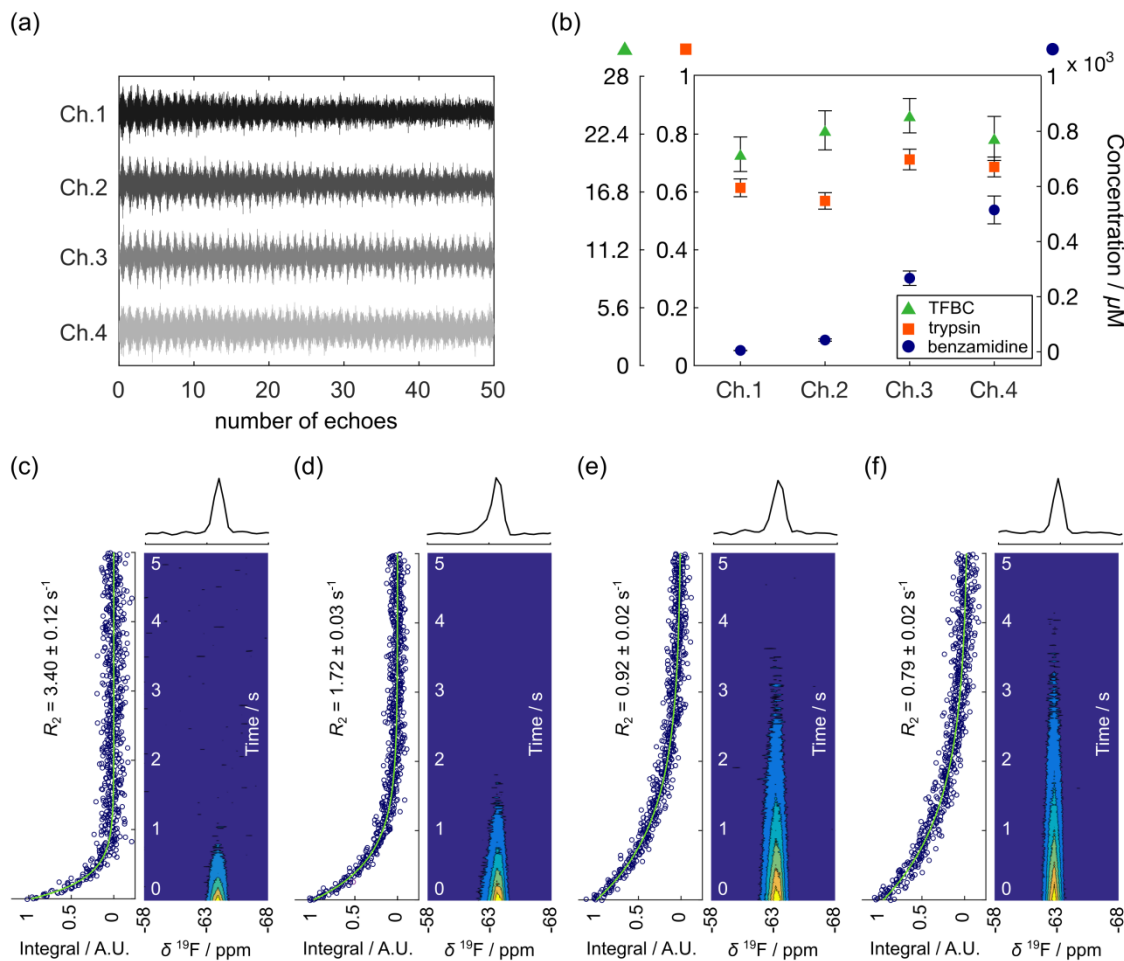
Figure 5.4: (a) First 50 spin-echoes acquired from the four simultaneous measurements of concentration dependent relaxation rates of hyperpolarized reporter ligand (TFBC) in the presence of trypsin and the competing ligand, benzamidine. (b) Final concentrations determined for TFBC, trypsin and benzamidine in the measurements shown in (a). (c)-(f) Contour plots of chemical shift resolved CPMG spectra obtained from Ch.1 – Ch.4 (from left to right). First 625 spectra (0 ~ 5 s) are shown. The first spectrum from each dataset is shown on top of the contour plot. The integrated signals are plotted with a fitted curve (green) next to the contour plot.
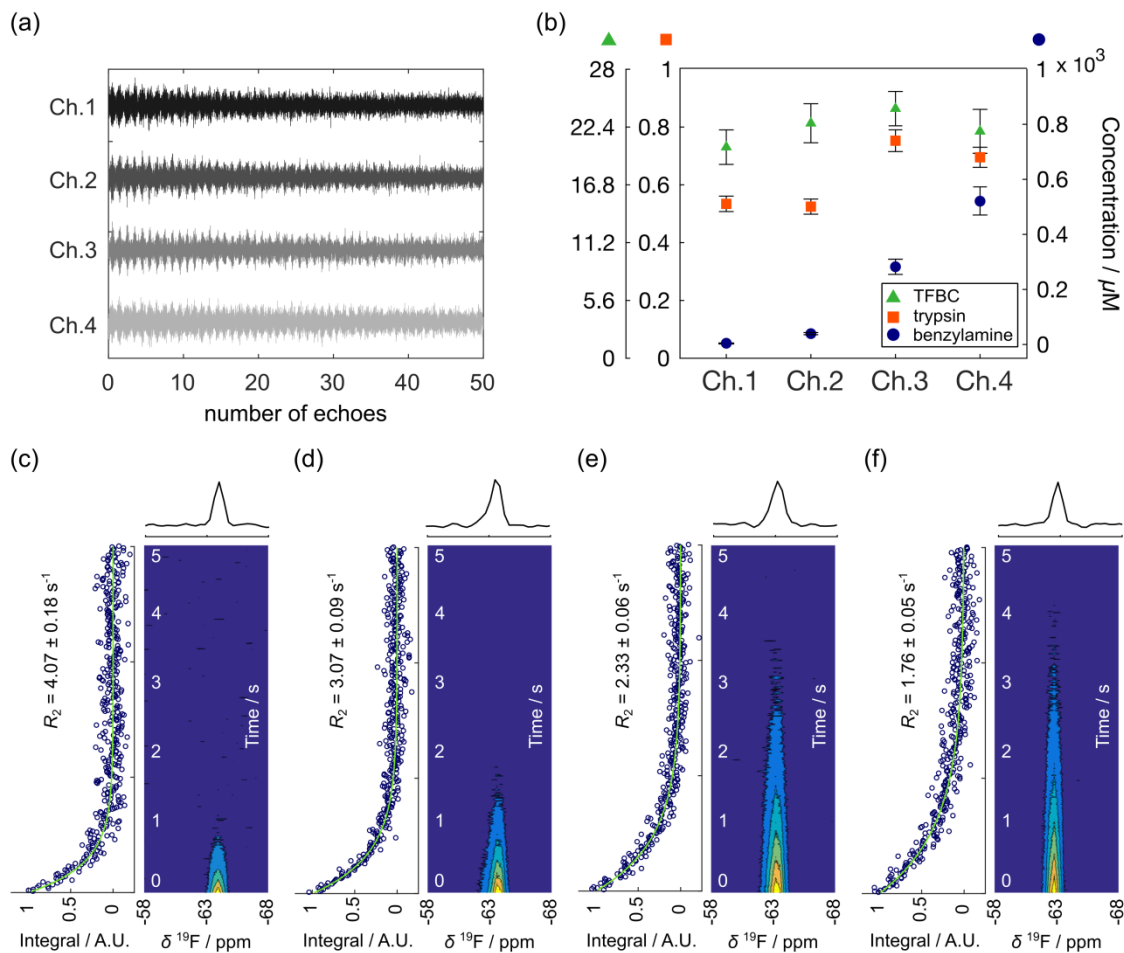
Figure 5.5: (a) First 50 spin-echoes acquired from the four simultaneous measurements of concentration dependent relaxation rates of hyperpolarized reporter ligand (TFBC) in the presence of trypsin and the competing ligand, benzylamine. (b) Final concentrations determined for TFBC, trypsin and benzylamine in the measurements shown in (a). (c)-(f) Contour plots of chemical shift resolved CPMG spectra obtained from Ch1 – Ch4 (from left to right). First 625 spectra (0 ~ 3s) are shown. The first spectrum from each dataset is shown on top of the contour plot. The integrated signals are plotted with a fitted curve (green) next to the contour plot.

each channel was obtained. Without any modification to the experimental parameters such as sample concentrations, the relaxation experiment was conducted for a second ligand, benzylamine, which has a higher binding affinity than benzamidine (Figure 5.5).

5.3.2. K_D determination

The resulting $R_{2,obs}$ values of TFBC under competition with benzamidine and benzylamine are plotted with circles in Figure 5.6a and b, respectively. At all concentrations, a higher $R_{2,obs}$ is found with benzylamine compared to with benzamidine, which is explained by the relative binding strength of the two ligands. In the same trend, the fitting errors for $R_{2,obs}$, represented by error bars the figure, from the benzylamine experiment are higher, which is attributed to fewer data points contributing to the data fitting for fast-relaxing signals (higher $R_{2,obs}$).

To determine K_D from four simultaneously measured $R_{2,obs}$ values, parameters including R_2 values of reporter ligand in the free and bound states ($R_{2,f}$ and $R_{2,b}^*$), the concentrations of protein and ligands in each channel, and K_D of reporter ligand are required. The R_2 references were determined from separate measurements with the hyperpolarized reporter ligand (TFBC) in the absence and the presence of a known amount of trypsin. From three repetitions, the average $R_{2,f}$ and $R_{2,b}^*$ for the four channels was found to be 0.66 ± 0.02 s^{-1} and 841 ± 82 s^{-1}, respectively. For the determination of $R_{2,b}^*$, the fraction of bound TFBC (pb) was first calculated based on the known values of K_D of TFBC and the concentrations of TFBC and trypsin. Then, pb was used to calculate $R_{2,b}^*$ from Equation (1.5) with the $R_{2,obs}$ and $R_{2,f}$ rates obtained from the measurements. The values of $R_{2,f}$ and $R_{2,b}^*$ were assumed to be the same for all channels in the data analysis.
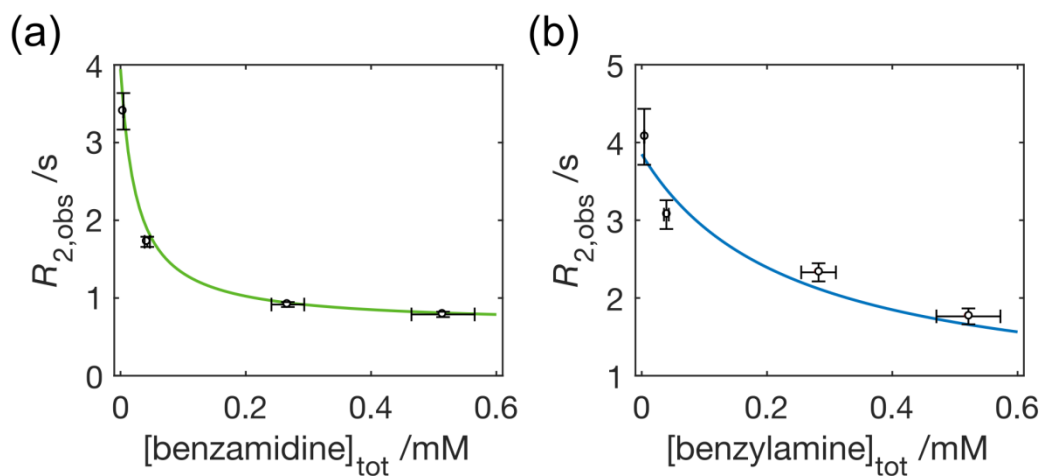
Figure 5.6: R_2 plots obtained from the relaxation measurements for benzamidine (a) and benzylamine (b). The curves represent the calculated relaxation rates using the fitted K_D of 21.6 μM and 205 μM for benzamidine and benzylamine, respectively, in combination with the average concentrations of trypsin and TFBC from the four channels. The error bars represent the 95% confidence intervals associated with the measured $R_{2,\text{obs}}$ (along the vertical axis) and 5% error of the measured concentrations for competing ligands (along the horizontal axis).

Individually measured values are summarized in Table 5.2. A variation of about 10% in the $R_{2,b}^{*}$ values was observed from the four channels, which may be caused by different rf-pulse (B_1) or main field (B_0) distributions. With the final sample concentrations, which were 22.3 μM and 0.66 μM for trypsin on average, the dissociation constant of the competing ligand was found by fitting of the $R_{2,\text{obs}}$ values. From the datasets shown in Figure 5.6, K_D for benzamidine and benzylamine were determined to be 21.6 μM and 205 μM, respectively.

Table 5.2: R_2 relaxation rates measured for free ($R_{2,f}$) and bound ($R_{2,b}^*$) ligands. The sample concentrations used for the measurements are 22.3 μM for TFBC and 0.66 μM for trypsin on average.

	Ch. 1	Ch. 2	Ch. 3	Ch. 4	Average
$R_{2,f}$ / s^{-1}	0.67 ± 0.02	0.65 ± 0.02	0.66 ± 0.02	0.65 ± 0.01	0.66 ± 0.02
$R_{2,b}^*$ / s^{-1}	900 ± 90	798 ± 79	872 ± 65	794 ± 75	841 ± 82

5.3.3. Error analysis

To provide error estimates for K_D that combine all the uncertainties present, Monte Carlo simulations were performed. First, 10^4 parameter sets were generated, each of which was composed of the measured relaxation rates ($R_{2,f}$, $R_{2,b}^*$, and $R_{2,obs}$) and the concentrations of trypsin and two competing ligands. The assumptions made for this simulation are (1) $R_{2,f}$ and $R_{2,b}^*$ values are normally distributed about their corresponding value of the averaged R_2 with a relative standard deviation of 2.5% and 9.7%, respectively. (2) $R_{2,obs}$ values are normally distributed about the fitted $R_{2,obs}$ with a standard deviation obtained from each individual fit (fitting error). (3) Sample concentrations are normally distributed about the measured values with a relative standard deviation of 5%. (4) The binding affinity of reporter ligand is known exactly as K_D = 142 μM.[144] From the combinations of these simulated parameters, a distribution of K_D values was obtained. It was found that the 95% confidence intervals of K_D determined for benzamidine and benzylamine from a single measurement were (12.0 μM, 36.1 μM) and (136 μM, 327 μM), respectively. The K_D values and the associated error ranges obtained from additional experiments are summarized in Table 5.3. The table shows that the results are reproducible

with less than 4% of relative standard deviation. The K_D values can be found by an alternative method, where $R_{2,b}^*$ and K_D are determined simultaneously from the datasets of the reference experiments and the competitive binding experiments. Using this method, the values of $R_{2,b}^*$ and K_D were found to be identical to the above within the error limits. An advantage of first determining $R_{2,b}^*$, as described above, is that the reference datasets do not need to be fitted for every K_D determination.

Table 5.3: The K_D estimates obtained from the concentration-dependent R_2 measurements and the associated error ranges from Monte Carlo simulations

Ligand		K_D (μM)	Literature values (μM)
Benzamidine	Trial 1	21.6, (12.0, 36.1)	35,[183] 16 ± 2,[165] (8.3, 19.6)[b,182]
	Trial 2	23.0, (14.1, 36.1)	
	Trial 3	22.2, (12.4, 36.7)	
Benzylamine	Trial 1	205, (136, 327)	300,[183] 218 ± 43,[165] (151, 328)[b,182]
	Trial 2	220, (141, 362)	
	Trial 3	215, (142, 351)	

[a] The first value indicates K_D (μM) obtained from the fitting of $R_{2,obs}$ datasets, and the following values in the parenthesis represent the central 95% of the K_D distributions yielded from the simulations. [b] The values in the parenthesis represent 95% confidence intervals of K_D distributions determined from error analysis using Monte Carlo method.

We have further assessed the uncertainties in the K_D determination for wide-ranging affinities of a competing ligand from 10^{-2} to 10^4 μM. The data points shown in Figure 5.7a are examples of R_2 values from artificial datasets created for seven selected K_D values at given concentrations similar to the experimental condition. For each case, a total of 10^4 values for R_2 were generated assuming that the R_2 values are normally distributed about the value of R_2 calculated using Equation (1.5) with a standard deviation equal to 6% of the calculated R_2 value. This error range was decided on based on the fitting errors obtained from all of the measured relaxation datasets. Except for this modification to the assumption (3) made above, the same assumptions were applied to the simulations. The uncertainties accumulated through the sequential K_D determination steps are indicated in Figure 5.7b using the error bars encompassing central 95% of the K_D distributions. It
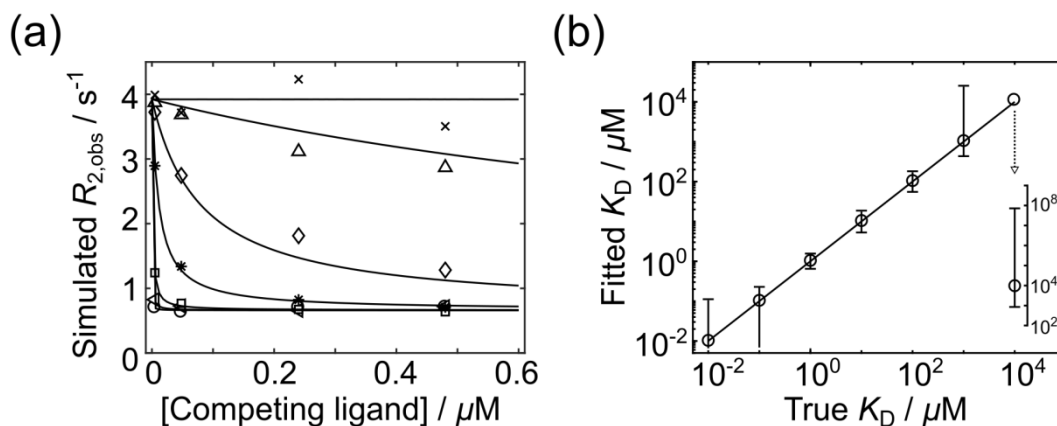
Figure 5.7: Random sets of simulated $R_{2,obs}$ values generated for each case of the competing ligand with $K_D = 10^{-2}$, 10^{-1}, 10^0, 10^1, 10^2, 10^3, and 10^4 μM. For the simulations, the concentrations of reporter ligand, trypsin, and competing ligand were 22.3 μM, 0.62 μM, and [4.8, 48, 240, 480] μM; $R_{2,f} = 0.66$ s^{-1}, $R_{2,b}{}^* = 841$ s^{-1}, reporter ligand $K_D = 142$ μM. The curves represent the best fits to simulated data points. (b) Simulation results. Median values of the K_D distributions resulting from 10^4 simulated datasets ('Fitted K_D') are plotted versus the corresponding values of true K_D. The error bars indicate 95% confidence intervals of the simulated K_D distributions. The lower end of the error bar for $K_D \leq 10^{-1}$ μM extends to $K_D = 0$, which could not be drawn in the plot.

was found that K_D can be determined with a similar level of error to that observed for the K_D values of benzamidine and benzylamine over three orders of magnitude, from 10^0 to 10^2 μM. The error becomes significant when $K_D \geq 10^3$ μM or $K_D \leq 10^{-1}$ μM, where the width of the 95% confidence interval exceeds the true K_D value by 20-fold. Additionally, it was found that the most significant source of error is $R_{2,b}^*$. This uncertainty can be reduced through multiple measurements of this reference value. In the absence of $R_{2,b}^*$ error, the confidence intervals for K_D would be reduced approximately by half.

It has been previously shown that it is possible to obtain an accurate K_D from a single- or two-point R_2 measurement with competitive binding using D-DNP.[165,182] The four-channel NMR apparatus described here covers a broadened range of screenable K_D over three orders of magnitude compared to the previous experiments. It effectively permits the use of a single experiment without individual optimization of experimental conditions. A challenge in using multiple coils is the need for shimming over an extended volume. Here, the experiment was intended for relaxometry including the measurement of a single ^{19}F signal. For this purpose, a typical line width of ~1 ppm as seen in Figure 5.4c-f is sufficient. Homogeneity could potentially be improved by shimming techniques for multiple coils, as well as by magnetic susceptibility matching of coils and flow cells.

The applicability of multiplexed D-DNP NMR can be extended to screening multiple ligands in one spectrum or to chemical shift based functional assays.[140] ^{19}F-NMR detection offers the benefit of avoiding the need to suppress a large signal of hyperpolarized water protons. Screening methods based on polarization transfer from hyperpolarized water would also be compatible with the multiplexed system.[184] The multiplexed D-DNP approach can be used for other experiments that involve several

measurements on the same sample with variations of experimental parameters. Such experiments would be inefficient with D-DNP instrumentation requiring multiple dissolutions. Examples include NMR based titrations or relaxation dispersion measurements that require multiple pulsing delays.[105] Another approach to high-throughput D-DNP NMR has previously been described, which enables polarization of multiple different sample aliquots simultaneously and dissolving each sample independently.[158,166,180,181] The multiplexing method described here could also be combined with this approach to further increase the efficiency of D-DNP NMR experiments. Lastly, similar multiplexed flow NMR systems may be applicable to measurements without hyperpolarization, such as in screening of protein-ligand interactions.

5.4.   Conclusions

Using a multi-channel flow NMR system, we have demonstrated that the throughput of D-DNP NMR experiments can be improved by four times. The system was applied to determine the binding affinities of two non-fluorinated ligands from concentration-dependent R_2 relaxation measurements, using competitive binding with a fluorinated reporter ligand. From a single hyperpolarization experiment, a titration curve of the ligand under investigation could be obtained. Without altering the sample concentrations, it was possible to accurately measure the binding affinities of the two ligands, which differ 10-fold. Further, it was evaluated that this method permits to determine K_D in a range over three orders of magnitude under the experimental conditions examined. Besides the advantages brought by the increased throughput, the described

screening method benefits from the dramatically enhanced signal intensity by hyperpolarization. It allowed for reducing the protein concentration to a few μM in a stock solution, and several hundred nM was sufficient for the measurements. These required sample concentrations are compatible with targeting proteins that are difficult to express or poorly soluble.

6.   SUMMARY AND CONCLUSIONS

Nuclear magnetic resonance (NMR) is a robust spectroscopic method widely used in drug discovery for screening compounds that bind to a drug target. Its strength lies in the capability of detecting low-affinity ligands, which is desirable in the fragment-based screening approach. A number of NMR based screening methods have been established for binding identification and affinity determination. These methods, however, face major challenges due to low sensitivity and throughput. A solution to the sensitivity problem can be provided by the hyperpolarization technique of D-DNP. With a signal enhancement of $3 \sim 4$ orders of magnitude in the liquid state compared to conventional NMR, the need for signal averaging and the problems arising due to a low protein or ligand solubility can be avoided.

The benefits of D-DNP can be combined with those of ^{19}F NMR based screening methods by hyperpolarizing a fluorinated ligand for use as a reporter in the screening of non-fluorinated ligands. To demonstrate NMR screening with ^{19}F-DNP, a fluorinated reporter ligand and non-fluorinated ligands with strong to weak binding affinity were chosen that competitively bind to the same target protein. The competitive binding was observed in single-scan CPMG experiments by measuring transverse relaxation rates, R_2 of the reporter ligand in the absence and presence of non-fluorinated ligands at constant trypsin concentration. A decrease in R_2 of the reporter ligand indicated displacements of bound reporter ligand by the non-fluorinated ligand, through which the binding interaction was identified. At optimal ligand concentrations where close to 50% of bound reporter ligand is displaced, the dissociation constants, K_D of the non-fluorinated ligands were able

to be determined from single data. As R_2 of ^{19}F NMR is highly sensitive to ligand binding, the trypsin concentration could be reduced to 0.5 μM to detect the competitive binding of a strongly binding ligand with 1 μM reporter ligand, giving rise to less than 0.5% of the reporter ligand in the bound state.

Despite the substantial signal enhancement by DNP, the nature of the most commonly available instrumentation for D-DNP provides a single hyperpolarized sample after each polarization process, limiting the achievable throughput. A multiplexed NMR system was developed to improve the throughput of D-DNP experiments which permitted parallelized screening experiments. In combination with a flow injection system allowing for mixing hyperpolarized ligand with non-hyperpolarized protein and competitive ligand at a desired ratio, multiple R_2 relaxation rates of the reporter ligand were obtained simultaneously as a function of competitive ligand concentration. With four-channel NMR detection, it was possible to determine K_D for the ligands with affinities that are in different orders of magnitude without the need for adjusting the experimental conditions as required when only a single dataset can be acquired. From error analysis, it was found that the detectable range of K_D under a single set of experimental conditions covers up to three orders of magnitude. Additionally, the experimental time is reduced by four times. In drug screening, where little information is known about the compounds under study, the multiplexed D-DNP NMR screening could be a convenient method to rank compounds with a wide range of affinities.

In conclusion, a method for D-DNP assisted ^{19}F-NMR screening was developed that can provide a signal enhancement of over a thousand-fold. With this method, the determination of K_D for ligands of interest was demonstrated from a single experiment,

which improves throughput. These capabilities may increase the practicality of D-DNP NMR for drug discovery. The multiplexed-detection and flow NMR techniques developed here can be further utilized in other D-DNP experiments to improve the time efficiency in general.

REFERENCES

(1)   Balunas, M. J.; Kinghorn, A. D. Drug Discovery from Medicinal Plants. *Life Sciences* **2005**, *78* (5), 431–441.

(2)   Drews, J. Drug Discovery: A Historical Perspective. *Science* **2000**, *287* (5460), 1960–1964.

(3)   Gershell, L. J.; Atkins, J. H. A Brief History of Novel Drug Discovery Technologies. *Nature Reviews Drug Discovery* **2003**, *2* (4), 321–327.

(4)   Pina, A. S.; Hussain, A.; Roque, A. C. A. An Historical Overview of Drug Discovery. *Ligand-Macromolecular Interactions in Drug Discovery*; Roque, A. C. A., Ed.; Humana Press: Totowa, NJ, 2010; Vol. 572, pp 3–12.

(5)   Mestre-Ferrandiz, J.; Sussex, J.; Towse, A. *The R&D Cost of a New Medicine*; Monographs; Office of Health Economics, 2012.

(6)   Nicolaou, K. C. Advancing the Drug Discovery and Development Process. *Angew. Chem.* **2014**, *126* (35), 9280–9292.

(7)   Craik, D. J.; Smith, P. A.; Clark, R. J. NMR-Based Screening and Drug Discovery. In *Burger's Medicinal Chemistry and Drug Discovery*; John Wiley & Sons, Inc.: Hoboken, NJ, USA, 2010.

(8)   Schneider, G. Automating Drug Discovery. *Nature Reviews Drug Discovery* **2017**, *17* (2), 97–113.

(9)   Entzeroth, M.; Flotow, H.; Condron, P. Overview of High-Throughput Screening. In *Current Protocols in Pharmacology*; Enna, S. J., Williams, M., Barret, J. F.,

Ferkany, J. W., Kenakin, T., Porsolt, R. D., Eds.; John Wiley & Sons, Inc.: Hoboken, NJ, USA, 2009.

(10)   Schuffenhauer, A.; Ruedisser, S.; Marzinzik, A. L.; Jahnke, W.; Blommers, M.; Selzer, P.; Jacoby, E. Library Design for Fragment Based Screening. *Current Topics in Medicinal Chemistry* **2005**, *5* (8), 751–762.

(11)   Ma, R.; Wang, P.; Wu, J.; Ruan, K. Process of Fragment-Based Lead Discovery— A Perspective from NMR. *Molecules* **2016**, *21* (7), 854.

(12)   Erlanson, D. A.; Fesik, S. W.; Hubbard, R. E.; Jahnke, W.; Jhoti, H. Twenty Years on: The Impact of Fragments on Drug Discovery. *Nature Reviews Drug Discovery* **2016**, *15* (9), 605–619.

(13)   Shuker, S. B.; Hajduk, P. J.; Meadows, R. P.; Fesik, S. W. Discovering High-Affinity Ligands for Proteins: SAR by NMR. *Science* **1996**, *274* (5292), 1531–1534.

(14)   Hartshorn, M. J.; Murray, C. W.; Cleasby, A.; Frederickson, M.; Tickle, I. J.; Jhoti, H. Fragment-Based Lead Discovery Using X-Ray Crystallography. *J. Med. Chem.* **2005**, *48* (2), 403–413.

(15)   Giannetti, A. M. From Experimental Design to Validated Hits. In *Methods in Enzymology*; Elsevier, 2011; Vol. 493, pp 169–218.

(16)   Dalvit, C. NMR Methods in Fragment Screening: Theory and a Comparison with Other Biophysical Techniques. *Drug Discovery Today* **2009**, *14* (21–22), 1051–1057.

(17) Gossert, A. D.; Jahnke, W. NMR in Drug Discovery: A Practical Guide to Identification and Validation of Ligands Interacting with Biological Macromolecules. *Prog. Nucl. Magn. Reson. Spectrosc.* **2016**, *97*, 82–125.

(18) Meyer, B.; Peters, T. NMR Spectroscopy Techniques for Screening and Identifying Ligand Binding to Protein Receptors. *Angew. Chem. Int. Ed.* **2003**, *42* (8), 864–890.

(19) Sugiki, T.; Furuita, K.; Fujiwara, T.; Kojima, C. Current NMR Techniques for Structure-Based Drug Discovery. *Molecules* **2018**, *23* (1), 148.

(20) Baker, M. Fragment-Based Lead Discovery Grows Up. *Nature Reviews Drug Discovery* **2013**, *12* (1), 5–7.

(21) Chessari, G.; Woodhead, A. J. From Fragment to Clinical Candidate—a Historical Perspective. *Drug Discovery Today* **2009**, *14* (13–14), 668–675.

(22) Fielding, L. NMR Methods for the Determination of Protein–Ligand Dissociation Constants. *Prog. Nucl. Magn. Reson. Spectrosc.* **2007**, *51* (4), 219–242.

(23) Carver, J. P.; Richards, R. E. A General Two-Site Solution for the Chemical Exchange Produced Dependence of T_2 upon the Carr-Purcell Pulse Separation. *J. Magn. Reson. (1969)* **1972**, *6* (1), 89–105.

(24) Wennerström, H. Nuclear Magnetic Relaxation Induced by Chemical Exchange. *Mol. Phys.* **1972**, *24* (1), 69–80.

(25) McConnell, H. M. Reaction Rates by Nuclear Magnetic Resonance. *J. Chem. Phys.* **1958**, *28* (3), 430–431.

(26)   Swift, T. J.; Connick, R. E. NMR-Relaxation Mechanisms of O17 in Aqueous Solutions of Paramagnetic Cations and the Lifetime of Water Molecules in the First Coordination Sphere. *J. Chem. Phys.* **1962**, *37* (2), 307–320.

(27)   Pervushin, K.; Riek, R.; Wider, G.; Wüthrich, K. Transverse Relaxation-Optimized Spectroscopy (TROSY) for NMR Studies of Aromatic Spin Systems in ^{13}C-Labeled Proteins. *J. Am. Chem. Soc.* **1998**, *120* (25), 6394–6400.

(28)   Salzmann, M.; Pervushin, K.; Wider, G.; Senn, H.; Wüthrich, K. NMR Assignment and Secondary Structure Determination of an Octameric 110 KDa Protein Using TROSY in Triple Resonance Experiments. *J. Am. Chem. Soc.* **2000**, *122* (31), 7543–7548.

(29)   Kodama, Y.; Takeuchi, K.; Shimba, N.; Ishikawa, K.; Suzuki, E.; Shimada, I.; Takahashi, H. Rapid Identification of Ligand-Binding Sites by Using an Assignment-Free NMR Approach. *J. Med. Chem.* **2013**, *56* (22), 9342–9350.

(30)   Levitt, M. H. *Spin Dynamics: Basics of Nuclear Magnetic Resonance*, 2nd ed.; John Wiley & Sons: Chichester, England ; Hoboken, NJ, 2008.

(31)   Meiboom, S.; Gill, D. Modified Spin-Echo Method for Measuring Nuclear Relaxation Times. *Review of Scientific Instruments* **1958**, *29* (8), 688–691.

(32)   Dubois, B. W.; Evers, A. S. Fluorine-19 NMR Spin-Spin Relaxation (T2) Method for Characterizing Volatile Anesthetic Binding to Proteins. Analysis of Isoflurane Binding to Serum Albumin. *Biochemistry* **1992**, *31* (31), 7069–7076.

(33)   Furukawa, A.; Konuma, T.; Yanaka, S.; Sugase, K. Quantitative Analysis of Protein–Ligand Interactions by NMR. *Prog. Nucl. Magn. Reson.* **2016**, *96*, 47–57.

(34)   Sugase, K.; Dyson, H. J.; Wright, P. E. Mechanism of Coupled Folding and Binding of an Intrinsically Disordered Protein. *Nature* **2007**, *447* (7147), 1021–1025.

(35)   Allerhand, A.; Gutowsky, H. S. Spin-Echo Studies of Chemical Exchange. II. Closed Formulas for Two Sites. *J. Chem. Phys.* **1965**, *42* (5), 1587–1599.

(36)   Jahnke, W. Spin Labels as a Tool to Identify and Characterize Protein–Ligand Interactions by NMR Spectroscopy. *ChemBioChem* **2002**, *3* (2–3), 167–173.

(37)   Zhang, J.; Adrián, F. J.; Jahnke, W.; Cowan-Jacob, S. W.; Li, A. G.; Iacob, R. E.; Sim, T.; Powers, J.; Dierks, C.; Sun, F.; et al. Targeting Bcr–Abl by Combining Allosteric with ATP-Binding-Site Inhibitors. *Nature* **2010**, *463* (7280), 501–506.

(38)   Vanwetswinkel, S.; Heetebrij, R. J.; van Duynhoven, J.; Hollander, J. G.; Filippov, D. V.; Hajduk, P. J.; Siegal, G. TINS, Target Immobilized NMR Screening: An Efficient and Sensitive Method for Ligand Discovery. *Chemistry & Biology* **2005**, *12* (2), 207–216.

(39)   Salvi, N.; Buratto, R.; Bornet, A.; Ulzega, S.; Rentero Rebollo, I.; Angelini, A.; Heinis, C.; Bodenhausen, G. Boosting the Sensitivity of Ligand–Protein Screening by NMR of Long-Lived States. *J. Am. Chem. Soc.* **2012**, *134* (27), 11076–11079.

(40)   Mayer, M.; Meyer, B. Characterization of Ligand Binding by Saturation Transfer Difference NMR Spectroscopy. *Angew. Chem. Int. Ed.* **1999**, *38* (12), 1784–1788.

(41)   Dalvit, C.; Pevarello, P.; Tatò, M.; Veronesi, M.; Vulpetti, A.; Sundström, M. Identification of Compounds with Binding Affinity to Proteins via Magnetization Transfer from Bulk Water. *J. Biomol. NMR* **2000**, *18* (1), 65–68.

(42)   Ni, F. Recent Developments in Transferred NOE Methods. *Prog. Nucl. Magn. Reson.* **1994**, *26, Part 6*, 517–606.

(43)   Sánchez-Pedregal, V. M.; Reese, M.; Meiler, J.; Blommers, M. J. J.; Griesinger, C.; Carlomagno, T. The INPHARMA Method: Protein-Mediated Interligand NOEs for Pharmacophore Mapping. *Angew. Chem. Int. Ed.* **2005**, *44* (27), 4172–4175.

(44)   Dalvit, C.; Fagerness, P. E.; Hadden, D. T. A.; Sarver, R. W.; Stockman, B. J. Fluorine-NMR Experiments for High-Throughput Screening: Theoretical Aspects, Practical Considerations, and Range of Applicability. *J. Am. Chem. Soc.* **2003**, *125* (25), 7696–7703.

(45)   Dalvit, C.; Ardini, E.; Fogliatto, G. P.; Mongelli, N.; Veronesi, M. Reliable High-Throughput Functional Screening with 3-FABS. *Drug Discovery Today* **2004**, *9* (14), 595–602.

(46)   Coyne, K. New World-Record Magnet Fulfills Superconducting Promise. *National high magnetic field laboratory*, 2017.

(47)   Hoult, D. .; Richards, R. . The Signal-to-Noise Ratio of the Nuclear Magnetic Resonance Experiment. *J. Magn. Reson. (1969)* **1976**, *24* (1), 71–85.

(48)   *Protein NMR Spectroscopy: Principles and Practice*, 2. ed.; Cavanagh, J., Ed.; Elsevier, Acad. Press: Amsterdam, 2007.

(49)   Shoolery, J. N. NMR Spectroscocpy in the Beginning. *Anal. Chem.* **1993**, *65* (17), 731A-741A.

(50)   Morris, G. A.; Freeman, R. Enhancement of Nuclear Magnetic Resonance Signals by Polarization Transfer. *J. Am. Chem. Soc.* **1979**, *101* (3), 760–762.

(51)   Mancini, L.; Payne, G. S.; Leach, M. O. Comparison of Polarization Transfer Sequences for Enhancement of Signals in Clinical31P MRS Studies. *Magn. Reson. Med.* **2003**, *50* (3), 578–588.

(52)   Hoult, D. I. The NMR Receiver: A Description and Analysis of Design. *Prog. Nucl. Magn. Reson. Spectrosc.* **1978**, *12* (1), 41–77.

(53)   Peck, T. L.; Magin, R. L.; Lauterbur, P. C. Design and Analysis of Microcoils for NMR Microscopy. *J. Magn. Reson. B* **1995**, *108* (2), 114–124.

(54)   Olson, D. L.; Peck, T. L.; Webb, A. G.; Magin, R. L.; Sweedler, J. V. High-Resolution Microcoil ^{1}H-NMR for Mass-Limited, Nanoliter-Volume Samples. *Science* **1995**, *270* (5244), 1967–1970.

(55)   Li, Y.; Wolters, A. M.; Malawey, P. V.; Sweedler, J. V.; Webb, A. G. Multiple Solenoidal Microcoil Probes for High-Sensitivity, High-Throughput Nuclear Magnetic Resonance Spectroscopy. *Anal. Chem.* **1999**, *71* (21), 4815–4820.

(56)   Henry, I. D.; Park, G. H. J.; Kc, R.; Tobias, B.; Raftery, D. Design and Construction of a Microcoil NMR Probe for the Routine Analysis of 20-ML Samples. *Concepts Magn. Reson.* **2008**, *33B* (1), 1–8.

(57)   Kainosho, M.; Torizawa, T.; Iwashita, Y.; Terauchi, T.; Mei Ono, A.; Güntert, P. Optimal Isotope Labelling for NMR Protein Structure Determinations. *Nature* **2006**, *440* (7080), 52–57.

(58)   Goto, N. K.; Gardner, K. H.; Mueller, G. A.; Willis, R. C.; Kay, L. E. A Robust and Cost-Effective Method for the Production of Val, Leu, Ile (Δ1) Methyl-Protonated [15]N-, [13]C-, [2]H-Labeled Proteins. *J. Biomol. NMR* **1999**, *13* (4), 369–374.

(59)   Kovacs, H.; Moskau, D.; Spraul, M. Cryogenically Cooled Probes—a Leap in NMR Technology. *Prog. Nucl. Magn. Reson. Spectrosc.* **2005**, *46* (2–3), 131–155.

(60)   Carver, T. R.; Slichter, C. P. Polarization of Nuclear Spins in Metals. *Phys. Rev.* **1953**, *92* (1), 212–213.

(61)   Prisner, T. F. Dynamic Nuclear Polarization. In *NMR of Biomolecules*; Bertini, I., McGreevy, K. S., Parigi, G., Eds.; Wiley-VCH Verlag GmbH & Co. KGaA: Weinheim, Germany, 2012; pp 419–431.

(62)   Overhauser, A. W. Polarization of Nuclei in Metals. *Phys. Rev.* **1953**, *92* (2), 411–415.

(63)   Cherubini, A.; Bifone, A. Hyperpolarised Xenon in Biology. *Prog. Nucl. Magn. Reson. Spectrosc.* **2003**, *42* (1–2), 1–30.

(64)   Walker, T. G.; Happer, W. Spin-Exchange Optical Pumping of Noble-Gas Nuclei. *Rev. Mod. Phys.* **1997**, *69* (2), 629–642.

(65)   Goez, M. Chapter 3 Photo-CIDNP Spectroscopy. In *Annual Reports on NMR Spectroscopy*; Elsevier, 2009; Vol. 66, pp 77–147.

(66)   Mok, K. Photo-CIDNP NMR Methods for Studying Protein Folding. *Methods* **2004**, *34* (1), 75–87.

(67)   Adams, R. W.; Aguilar, J. A.; Atkinson, K. D.; Cowley, M. J.; Elliott, P. I. P.; Duckett, S. B.; Green, G. G. R.; Khazal, I. G.; López-Serrano, J.; Williamson, D. C. Reversible Interactions with Para-Hydrogen Enhance NMR Sensitivity by Polarization Transfer. *Science* **2009**, *323* (5922), 1708–1711.

(68)   Hovener, J.; Pravdivtsev, A. N.; Kidd, B.; Bowers, C. R.; Glöggler, S.; Kovtunov, K. V.; Plaumann, M.; Katz-Brull, R.; Buckenmaier, K.; Jerschow, A.; et al.

Parahydrogen-Based Hyperpolarization for Biomedicine. *Angew. Chem. Int. Ed.* **2018**, *57* (35), 11140–11162.

(69) Abragam, A.; Goldman, M. Principles of Dynamic Nuclear Polarisation. *Rep. Prog. Phys*. **1978**, *41* (3), 395–467.

(70) Jeffries, C. D. Polarization of Nuclei by Resonance Saturation in Paramagnetic Crystals. *Phys. Rev.* **1957**, *106* (1), 164–165.

(71) Hovav, Y.; Feintuch, A.; Vega, S. Dynamic Nuclear Polarization Assisted Spin Diffusion for the Solid Effect Case. *J. Chem. Phys.* **2011**, *134* (7), 074509.

(72) Hovav, Y.; Feintuch, A.; Vega, S. Theoretical Aspects of Dynamic Nuclear Polarization in the Solid State – The Cross Effect. *J. Magn. Reson.* **2012**, *214*, 29–41.

(73) Wenckebach, W. T. Dynamic Nuclear Polarization via Thermal Mixing: Beyond the High Temperature Approximation. *J. Magn. Reson.* **2017**, *277*, 68–78.

(74) Ardenkjær-Larsen, J. H.; Fridlund, B.; Gram, A.; Hansson, G.; Hansson, L.; Lerche, M. H.; Servin, R.; Thaning, M.; Golman, K. Increase in Signal-to-Noise Ratio of >10,000 Times in Liquid-State NMR. *Proc. Natl. Acad. Sci. U.S.A.* **2003**, *100* (18), 10158–10163.

(75) Hurd, R. E.; Yen, Y.-F.; Chen, A.; Ardenkjaer-Larsen, J. H. Hyperpolarized [13] C Metabolic Imaging Using Dissolution Dynamic Nuclear Polarization. *J. Magn. Reson. Imaging* **2012**, *36* (6), 1314–1328.

(76) Zhang, G.; Hilty, C. Applications of Dissolution Dynamic Nuclear Polarization in Chemistry and Biochemistry. *Magn. Reson. Chem.* **2018**, *56* (7), 566–582.

(77)   Zeng, H.; Lee, Y.; Hilty, C. Quantitative Rate Determination by Dynamic Nuclear Polarization Enhanced NMR of a Diels−Alder Reaction. *Anal. Chem.* **2010**, *82* (21), 8897–8902.

(78)   Liu, M.; Zhang, G.; Mahanta, N.; Lee, Y.; Hilty, C. Measurement of Kinetics and Active Site Distances in Metalloenzymes Using Paramagnetic NMR with ^{13}C Hyperpolarization. *J. Phys. Chem. Lett.* **2018**, *9* (9), 2218–2221.

(79)   Lee, Y. Dissolution Dynamic Nuclear Polarization–Enhanced Magnetic Resonance Spectroscopy and Imaging: Chemical and Biochemical Reactions in Nonequilibrium Conditions. *Appl. Spectrosc. Rev.* **2016**, *51* (3), 210–226.

(80)   Lee, Y.; Heo, G. S.; Zeng, H.; Wooley, K. L.; Hilty, C. Detection of Living Anionic Species in Polymerization Reactions Using Hyperpolarized NMR. *J. Am. Chem. Soc.* **2013**, *135* (12), 4636–4639.

(81)   Chen, C.-H.; Shih, W.-C.; Hilty, C. In Situ Determination of Tacticity, Deactivation, and Kinetics in [Rac-(C_2H_4(1-Indenyl)$_2$)ZrMe][B(C_6F_5)$_4$] and [Cp$_2$ZrMe][B(C_6F_5)$_4$]-Catalyzed Polymerization of 1-Hexene Using ^{13}C Hyperpolarized NMR. *J. Am. Chem. Soc.* **2015**, *137* (21), 6965–6971.

(82)   R. Jensen, P.; Meier, S.; H. Ardenkjær-Larsen, J.; Ø. Duus, J.; Karlsson, M.; H. Lerche, M. Detection of Low-Populated Reaction Intermediates with Hyperpolarized NMR. *Chem. Commun.* **2009**, (34), 5168–5170.

(83)   Kim, Y.; Chen, C.-H.; Hilty, C. Direct Observation of Ru-Alkylidene Forming into Ethylene in Ring-Closing Metathesis from Hyperpolarized ^{1}H NMR. *Chem. Commun.* **2018**, *54* (34), 4333–4336.

(84)   Zhang, G.; Schilling, F.; Glaser, S. J.; Hilty, C. Reaction Monitoring Using Hyperpolarized NMR with Scaling of Heteronuclear Couplings by Optimal Tracking. *J. Magn. Reson.* **2016**, *272*, 123–128.

(85)   Kurzbach, D.; Canet, E.; Flamm, A. G.; Jhajharia, A.; Weber, E. M. M.; Konrat, R.; Bodenhausen, G. Investigation of Intrinsically Disordered Proteins through Exchange with Hyperpolarized Water. *Angew. Chem. Int. Ed.* **2017**, *56* (1), 389–392.

(86)   Kim, J.; Liu, M.; Hilty, C. Modeling of Polarization Transfer Kinetics in Protein Hydration Using Hyperpolarized Water. *J. Phys. Chem. B* **2017**, *121* (27), 6492–6498.

(87)   Szekely, O.; Olsen, G. L.; Felli, I. C.; Frydman, L. High-Resolution 2D NMR of Disordered Proteins Enhanced by Hyperpolarized Water. *Anal. Chem.* **2018**, *90* (10), 6169–6177.

(88)   Wang, Y.; Ragavan, M.; Hilty, C. Site Specific Polarization Transfer from a Hyperpolarized Ligand of Dihydrofolate Reductase. *J. Biomol. NMR* **2016**, *65* (1), 41–48.

(89)   Min, H.; Sekar, G.; Hilty, C. Polarization Transfer from Ligands Hyperpolarized by Dissolution Dynamic Nuclear Polarization for Screening in Drug Discovery. *ChemMedChem* **2015**, *10* (9), 1559–1563.

(90)   Lee, Y.; Zeng, H.; Ruedisser, S.; Gossert, A. D.; Hilty, C. Nuclear Magnetic Resonance of Hyperpolarized Fluorine for Characterization of Protein–Ligand Interactions. *J. Am. Chem. Soc.* **2012**, *134* (42), 17448–17451.

(91)   Lee, Y.; Zeng, H.; Mazur, A.; Wegstroth, M.; Carlomagno, T.; Reese, M.; Lee, D.; Becker, S.; Griesinger, C.; Hilty, C. Hyperpolarized Binding Pocket Nuclear Overhauser Effect for Determination of Competitive Ligand Binding. *Angew. Chem. Int. Ed.* **2012**, *51* (21), 5179–5182.

(92)   Buratto, R.; Bornet, A.; Milani, J.; Mammoli, D.; Vuichoud, B.; Salvi, N.; Singh, M.; Laguerre, A.; Passemard, S.; Gerber-Lemaire, S.; et al. Drug Screening Boosted by Hyperpolarized Long-Lived States in NMR. *ChemMedChem* **2014**, *9* (11), 2509–2515.

(93)   Chappuis, Q.; Milani, J.; Vuichoud, B.; Bornet, A.; Gossert, A. D.; Bodenhausen, G.; Jannin, S. Hyperpolarized Water to Study Protein–Ligand Interactions. *J. Phys. Chem. Lett.* **2015**, *6* (9), 1674–1678.

(94)   Höfer, P.; Carl, P.; Guthausen, G.; Prisner, T.; Reese, M.; Carlomagno, T.; Griesinger, C.; Bennati, M. Studies of Dynamic Nuclear Polarization with Nitroxides in Aqueous Solution. *Appl. Magn. Reson.* **2008**, *34* (3–4), 393–398.

(95)   Zhu, Y.; Chen, C.-H.; Wilson, Z.; Savukov, I.; Hilty, C. Milli-Tesla NMR and Spectrophotometry of Liquids Hyperpolarized by Dissolution Dynamic Nuclear Polarization. *J. Magn. Reson.* **2016**, *270*, 71–76.

(96)   Miéville, P.; Ahuja, P.; Sarkar, R.; Jannin, S.; Vasos, P. R.; Gerber-Lemaire, S.; Mishkovsky, M.; Comment, A.; Gruetter, R.; Ouari, O.; et al. Scavenging Free Radicals To Preserve Enhancement and Extend Relaxation Times in NMR Using Dynamic Nuclear Polarization. *Angew. Chem. Int. Ed.* **2010**, *49* (35), 6182–6185.

(97)   Dollmann, B. C.; Junk, M. J. N.; Drechsler, M.; Spiess, H. W.; Hinderberger, D.; Münnemann, K. Thermoresponsive, Spin-Labeled Hydrogels as Separable DNP Polarizing Agents. *PCCP* **2010**, *12* (22), 5879–5882.

(98)   Gajan, D.; Bornet, A.; Vuichoud, B.; Milani, J.; Melzi, R.; van Kalkeren, H. A.; Veyre, L.; Thieuleux, C.; Conley, M. P.; Grüning, W. R.; et al. Hybrid Polarizing Solids for Pure Hyperpolarized Liquids through Dissolution Dynamic Nuclear Polarization. *Proc. Natl. Acad. Sci. U.S.A.* **2014**, *111* (41), 14693–14697.

(99)   McCarney, E. R.; Han, S. Spin-Labeled Gel for the Production of Radical-Free Dynamic Nuclear Polarization Enhanced Molecules for NMR Spectroscopy and Imaging. *J. Magn. Reson.* **2008**, *190* (2), 307–315.

(100)   Capozzi, A.; Hyacinthe, J.-N.; Cheng, T.; Eichhorn, T. R.; Boero, G.; Roussel, C.; van der Klink, J. J.; Comment, A. Photoinduced Nonpersistent Radicals as Polarizing Agents for X-Nuclei Dissolution Dynamic Nuclear Polarization. *J. Phys. Chem. C* **2015**, *119* (39), 22632–22639.

(101)   Eichhorn, T. R.; Takado, Y.; Salameh, N.; Capozzi, A.; Cheng, T.; Hyacinthe, J.-N.; Mishkovsky, M.; Roussel, C.; Comment, A. Hyperpolarization without Persistent Radicals for in Vivo Real-Time Metabolic Imaging. *Proc. Natl. Acad. Sci. U.S.A.* **2013**, *110* (45), 18064–18069.

(102)   Bowen, S.; Hilty, C. Rapid Sample Injection for Hyperpolarized NMR Spectroscopy. *PCCP* **2010**, *12* (22), 5766–5770.

(103)   Macnaughtan, M. A.; Hou, T.; Xu, J.; Raftery, D. High-Throughput Nuclear Magnetic Resonance Analysis Using a Multiple Coil Flow Probe. *Anal. Chem.* **2003**, *75* (19), 5116–5123.

(104)   Chen, H.-Y.; Hilty, C. Implementation and Characterization of Flow Injection in Dissolution Dynamic Nuclear Polarization NMR Spectroscopy. *ChemPhysChem* **2015**, *16* (12), 2646–2652.

(105)   Liu, M.; Kim, Y.; Hilty, C. Characterization of Chemical Exchange Using Relaxation Dispersion of Hyperpolarized Nuclear Spins. *Anal. Chem.* **2017**, *89* (17), 9154–9158.

(106)   Katsikis, S.; Marin-Montesinos, I.; Pons, M.; Ludwig, C.; Günther, U. L. Improved Stability and Spectral Quality in Ex Situ Dissolution DNP Using an Improved Transfer Device. *Appl. Mag. Reson.* **2015**, *46* (7), 723–729.

(107)   Granwehr, J.; Panek, R.; Leggett, J.; Köckenberger, W. Quantifying the Transfer and Settling in NMR Experiments with Sample Shuttling. *J. Chem. Phys.* **2010**, *132* (24), 244507.

(108)   Milani, J.; Vuichoud, B.; Bornet, A.; Miéville, P.; Mottier, R.; Jannin, S.; Bodenhausen, G. A Magnetic Tunnel to Shelter Hyperpolarized Fluids. *Rev. Sci. Instrum.* **2015**, *86* (2), 024101.

(109)   Zeng, H.; Bowen, S.; Hilty, C. Sequentially Acquired Two-Dimensional NMR Spectra from Hyperpolarized Sample. *J. Magn. Reson.* **2009**, *199* (2), 159–165.

(110)   Frydman, L.; Blazina, D. Ultrafast Two-Dimensional Nuclear Magnetic Resonance Spectroscopy of Hyperpolarized Solutions. *Nat. Phys.* **2007**, *3* (6), 415–419.

(111)   Ahola, S.; Zhivonitko, V. V.; Mankinen, O.; Zhang, G.; Kantola, A. M.; Chen, H.-Y.; Hilty, C.; Koptyug, I. V.; Telkki, V.-V. Ultrafast Multidimensional Laplace NMR for a Rapid and Sensitive Chemical Analysis. *Nat. Commun.* **2015**, *6*, 8363.

(112) Zhang, G.; Schilling, F.; Glaser, S. J.; Hilty, C. Chemical Shift Correlations from Hyperpolarized NMR Using a Single SHOT. *Anal. Chem.* **2013**, *85* (5), 2875–2881.

(113) Batel, M.; Krajewski, M.; Weiss, K.; With, O.; Däpp, A.; Hunkeler, A.; Gimersky, M.; Pruessmann, K. P.; Boesiger, P.; Meier, B. H.; et al. A Multi-Sample 94 GHz Dissolution Dynamic-Nuclear-Polarization System. *Journal of Magnetic Resonance* **2012**, *214*, 166–174.

(114) Hu, S.; Larson, P. E. Z.; VanCriekinge, M.; Leach, A. M.; Park, I.; Leon, C.; Zhou, J.; Shin, P. J.; Reed, G.; Keselman, P.; et al. Rapid Sequential Injections of Hyperpolarized [1-^{13}C]Pyruvate in Vivo Using a Sub-Kelvin, Multi-Sample DNP Polarizer. *Magn. Reson. Imaging* **2013**, *31* (4), 490–496.

(115) Bowen, S.; Ardenkjaer-Larsen, J. H. Enhanced Performance Large Volume Dissolution-DNP. *J. Magn. Reson.* **2014**, *240*, 90–94.

(116) Lee, J.; Ramirez, M. S.; Walker, C. M.; Chen, Y.; Yi, S.; Sandulache, V. C.; Lai, S. Y.; Bankson, J. A. High-Throughput Hyperpolarized ^{13}C Metabolic Investigations Using a Multi-Channel Acquisition System. *J. Magn. Reson.* **2015**, *260*, 20–27.

(117) Jannin, S.; Bornet, A.; Colombo, S.; Bodenhausen, G. Low-Temperature Cross Polarization in View of Enhancing Dissolution Dynamic Nuclear Polarization in NMR. *Chem. Phys. Lett.* **2011**, *517* (4–6), 234–236.

(118) Bornet, A.; Melzi, R.; Perez Linde, A. J.; Hautle, P.; van den Brandt, B.; Jannin, S.; Bodenhausen, G. Boosting Dissolution Dynamic Nuclear Polarization by Cross Polarization. *J. Phys. Chem. Lett.* **2013**, *4* (1), 111–114.

(119)   Bornet, A.; Melzi, R.; Jannin, S.; Bodenhausen, G. Cross Polarization for Dissolution Dynamic Nuclear Polarization Experiments at Readily Accessible Temperatures $1.2 < T < 4.2$ K. *Appl. Magn. Reson.* **2012**, *43* (1–2), 107–117.

(120)   Reynolds, S.; Patel, H. Monitoring the Solid-State Polarization of ^{13}C, ^{15}N, ^{2}H, ^{29}Si and ^{31}P. *Appl. Magn. Reson.* **2008**, *34* (3–4), 495–508.

(121)   Kurdzesau, F.; Brandt, B. van den; Comment, A.; Hautle, P.; Jannin, S.; Klink, J. J. van der; Konter, J. A. Dynamic Nuclear Polarization of Small Labelled Molecules in Frozen Water–Alcohol Solutions. *J. Phys. D: Applied Physics* **2008**, *41* (15), 155506.

(122)   Lumata, L.; Jindal, A. K.; Merritt, M. E.; Malloy, C. R.; Sherry, A. D.; Kovacs, Z. DNP by Thermal Mixing under Optimized Conditions Yields > 60000-Fold Enhancement of ^{89}Y NMR Signal. *J. Am. Chem. Soc.* **2011**, *133* (22), 8673–8680.

(123)   Lumata, L.; Merritt, M. E.; Hashami, Z.; Ratnakar, S. J.; Kovacs, Z. Production and NMR Characterization of Hyperpolarized ^{107,109}Ag Complexes. *Angew. Chem. Int. Ed.* **2012**, *51* (2), 525–527.

(124)   Ardenkjaer-Larsen, J. H.; Macholl, S.; Johannesson, H. Dynamic Nuclear Polarization with Trityls at 1.2 K. *Appl. Magn. Reson.* **2008**, *34* (3–4), 509–522.

(125)   Lumata, L.; Merritt, M. E.; Malloy, C. R.; Sherry, A. D.; Kovacs, Z. Impact of Gd^{3+} on DNP of [1-^{13}C]Pyruvate Doped with Trityl OX063, BDPA, or 4-Oxo-TEMPO. *J. Phys. Chem. A* **2012**, *116* (21), 5129–5138.

(126)   Lumata, L.; Merritt, M. E.; Kovacs, Z. Influence of Deuteration in the Glassing Matrix on ^{13}C Dynamic Nuclear Polarization. *PCCP* **2013**, *15* (19), 7032.

(127) Hu, K.-N.; Yu, H.; Swager, T. M.; Griffin, R. G. Dynamic Nuclear Polarization with Biradicals. *J. Am. Chem. Soc.* **2004**, *126* (35), 10844–10845.

(128) Song, C.; Hu, K.-N.; Joo, C.-G.; Swager, T. M.; Griffin, R. G. TOTAPOL: A Biradical Polarizing Agent for Dynamic Nuclear Polarization Experiments in Aqueous Media. *J. Am. Chem. Soc.* **2006**, *128* (35), 11385–11390.

(129) Ardenkjær-Larsen, J. H.; Laursen, I.; Leunbach, I.; Ehnholm, G.; Wistrand, L.-G.; Petersson, J. S.; Golman, K. EPR and DNP Properties of Certain Novel Single Electron Contrast Agents Intended for Oximetric Imaging. *J. Magn. Reson.* **1998**, *133* (1), 1–12.

(130) Lumata, L.; Ratnakar, S. J.; Jindal, A.; Merritt, M.; Comment, A.; Malloy, C.; Sherry, A. D.; Kovacs, Z. BDPA: An Efficient Polarizing Agent for Fast Dissolution Dynamic Nuclear Polarization NMR Spectroscopy. *Chem. Eur. J.* **2011**, *17* (39), 10825–10827.

(131) Kodibagkar, V. D.; Conradi, M. S. Remote Tuning of NMR Probe Circuits. *J. Magn. Reson.* **2000**, *144* (1), 53–57.

(132) Kaptein, R.; Dijkstra, K.; Tarr, C. E. A Single-Scan Fourier Transform Method for Measuring Spin-Lattice Relaxation Times. *J. Magn. Reson. (1969)* **1976**, *24* (2), 295–300.

(133) Chen, H.-Y.; Lee, Y.; Bowen, S.; Hilty, C. Spontaneous Emission of NMR Signals in Hyperpolarized Proton Spin Systems. *J. Magn. Reson.* **2011**, *208* (2), 204–209.

(134) Bloembergen, N. On the Interaction of Nuclear Spins in a Crystalline Lattice. *Physica* **1949**, *15* (3–4), 386–426.

(135) Ramanathan, C. Dynamic Nuclear Polarization and Spin Diffusion in Nonconducting Solids. *Appl. Magn. Reson.* **2008**, *34* (3–4), 409–421.

(136) Dementyev, A. E.; Cory, D. G.; Ramanathan, C. Rapid Diffusion of Dipolar Order Enhances Dynamic Nuclear Polarization. *Phys. Rev. B* **2008**, *77* (2), 024413.

(137) Comment, A.; van den Brandt, B.; Uffmann, K.; Kurdzesau, F.; Jannin, S.; Konter, J. A.; Hautle, P.; Wenckebach, W. T.; Gruetter, R.; van der Klink, J. J. Design and Performance of a DNP Prepolarizer Coupled to a Rodent MRI Scanner. *Concepts in Magnetic Resonance Part B: Magnetic Resonance Engineering* **2007**, *31B* (4), 255–269.

(138) Lumata, L.; Kovacs, Z.; Malloy, C.; Sherry, A. D.; Merritt, M. The Effect of ^{13}C Enrichment in the Glassing Matrix on Dynamic Nuclear Polarization of [1-^{13}C]Pyruvate. *Physics in Medicine & Biology* **2011**, *56* (5), N85–N92.

(139) Ludwig, C.; Marin-Montesinos, I.; Saunders, M. G.; Günther, U. L. Optimizing the Polarization Matrix for Ex Situ Dynamic Nuclear Polarization. *J. Am. Chem. Soc.* **2010**, *132* (8), 2508–2509.

(140) Vulpetti, A.; Hommel, U.; Landrum, G.; Lewis, R.; Dalvit, C. Design and NMR-Based Screening of LEF, a Library of Chemical Fragments with Different Local Environment of Fluorine. *J. Am. Chem. Soc.* **2009**, *131* (36), 12949–12959.

(141) Dalvit, C.; Ardini, E.; Flocco, M.; Fogliatto, G. P.; Mongelli, N.; Veronesi, M. A General NMR Method for Rapid, Efficient, and Reliable Biochemical Screening. *J. Am. Chem. Soc.* **2003**, *125* (47), 14620–14625.

(142) Jenkins, B. G. Detection of Site-Specific Binding and Co-Binding of Ligands to Macromolecules Using ^{19}F NMR. *Life Sciences* **1991**, *48* (13), 1227–1240.

(143) Ardenkjær-Larsen, J. H.; Fridlund, B.; Gram, A.; Hansson, G.; Hansson, L.; Lerche, M. H.; Servin, R.; Thaning, M.; Golman, K. Increase in Signal-to-Noise Ratio of > 10,000 Times in Liquid-State NMR. *Proc. Natl. Acad. Sci. U.S.A.* **2003**, *100* (18), 10158–10163.

(144) Lee, Y.; Zeng, H.; Ruedisser, S.; Gossert, A. D.; Hilty, C. Nuclear Magnetic Resonance of Hyperpolarized Fluorine for Characterization of Protein–Ligand Interactions. *J. Am. Chem. Soc.* **2012**, *134* (42), 17448–17451.

(145) Dalvit, C.; Flocco, M.; Knapp, S.; Mostardini, M.; Perego, R.; Stockman, B. J.; Veronesi, M.; Varasi, M. High-Throughput NMR-Based Screening with Competition Binding Experiments. *J. Am. Chem. Soc.* **2002**, *124* (26), 7702–7709.

(146) Heath, R. E.; Dykes, G. M.; Fish, H.; Smith, D. K. Rapid Screening of Binding Constants by Calibrated Competitive ^{1}H NMR Spectroscopy. *Chem. Eur. J.* **2003**, *9* (4), 850–855.

(147) Jahnke, W.; Floersheim, P.; Ostermeier, C.; Zhang, X.; Hemmig, R.; Hurth, K.; Uzunov, D. P. NMR Reporter Screening for the Detection of High-Affinity Ligands. *Angew. Chem. Int. Ed.* **2002**, *41* (18), 3420–3423.

(148) Buratto, R.; Bornet, A.; Milani, J.; Mammoli, D.; Vuichoud, B.; Salvi, N.; Singh, M.; Laguerre, A.; Passemard, S.; Gerber-Lemaire, S.; et al. Drug Screening Boosted by Hyperpolarized Long-Lived States in NMR. *ChemMedChem* **2014**, *9* (11), 2509–2515.

(149) Bowen, S.; Hilty, C. Time-Resolved Dynamic Nuclear Polarization Enhanced NMR Spectroscopy. *Angew. Chem. Int. Ed.* **2008**, *47* (28), 5235–5237.

(150) Ernst, R. R.; Bodenhausen, G.; Wokaun, A. *Principles of Nuclear Magnetic Resonance in One and Two Dimensions*; Clarendon Press, 1990.

(151) Lian, L. Y.; Roberts, G. C. K. *Effects of Chemical Exchange on NMR Spectra*; IRL Press: New York, 1993.

(152) Kurinov, I. V.; Harrison, R. W. Two Crystal Structures of the Leupeptin-Trypsin Complex. *Protein Science* **1996**, *5* (4), 752–758.

(153) Krieger, M.; Kay, L. M.; Stroud, R. M. Structure and Specific Binding of Trypsin: Comparison of Inhibited Derivatives and a Model for Substrate Binding. *J. Mol. Biol.* **1974**, *83* (2), 209–230.

(154) Chen, N.; Zou, J.; Wang, S.; Ye, Y.; Huang, Y.; Gadda, G.; Yang, J. J. Designing Protease Sensors for Real-Time Imaging of Trypsin Activation in Pancreatic Cancer Cells. *Biochemistry* **2009**, *48* (15), 3519–3526.

(155) Roberts, G. C. K. The Determination of Equilibrium Dissociation Constants of Protein-Ligand Complexes by NMR. In *BioNMR in Drug Research*; Zerbe, O., Ed.; Wiley-VCH Verlag GmbH & Co. KGaA, 2002; pp 309–319.

(156) Leggett, J.; Hunter, R.; Granwehr, J.; Panek, R.; Perez-Linde, A. J.; Horsewill, A. J.; McMaster, J.; Smith, G.; Köckenberger, W. A Dedicated Spectrometer for Dissolution DNP NMR Spectroscopy. *PCCP* **2010**, *12* (22), 5883–5892.

(157) Jóhannesson, H.; Macholl, S.; Ardenkjaer-Larsen, J. H. Dynamic Nuclear Polarization of [1-^{13}C]Pyruvic Acid at 4.6 Tesla. *J. Magn. Reson.* **2009**, *197* (2), 167–175.

(158) Batel, M.; Krajewski, M.; Weiss, K.; With, O.; Däpp, A.; Hunkeler, A.; Gimersky, M.; Pruessmann, K. P.; Boesiger, P.; Meier, B. H.; et al. A Multi-Sample 94 GHz

Dissolution Dynamic-Nuclear-Polarization System. *J. Magn. Reson.* **2012**, *214* (1), 166–174.

(159) Dalvit, C.; Mongelli, N.; Papeo, G.; Giordano, P.; Veronesi, M.; Moskau, D.; Kümmerle, R. Sensitivity Improvement in ^{19}F NMR-Based Screening Experiments: Theoretical Considerations and Experimental Applications. *J. Am. Chem. Soc.* **2005**, *127* (38), 13380–13385.

(160) Lepre, C. A.; Moore, J. M.; Peng, J. W. Theory and Applications of NMR-Based Screening in Pharmaceutical Research. *Chem. Rev.* **2004**, *104* (8), 3641–3676.

(161) Lee, J. H.; Okuno, Y.; Cavagnero, S. Sensitivity Enhancement in Solution NMR: Emerging Ideas and New Frontiers. *J. Magn. Reson.* **2014**, *241*, 18–31.

(162) Lerche, M. H.; Meier, S.; Jensen, P. R.; Baumann, H.; Petersen, B. O.; Karlsson, M.; Duus, J. Ø.; Ardenkjær-Larsen, J. H. Study of Molecular Interactions with ^{13}C DNP-NMR. *J. Magn. Reson.* **2010**, *203* (1), 52–56.

(163) Min, H.; Sekar, G.; Hilty, C. Polarization Transfer from Ligands Hyperpolarized by Dissolution Dynamic Nuclear Polarization for Screening in Drug Discovery. *ChemMedChem* **2015**, *10* (9), 1559–1563.

(164) Lee, Y.; Zeng, H.; Mazur, A.; Wegstroth, M.; Carlomagno, T.; Reese, M.; Lee, D.; Becker, S.; Griesinger, C.; Hilty, C. Hyperpolarized Binding Pocket Nuclear Overhauser Effect for Determination of Competitive Ligand Binding. *Angew. Chem. Int. Ed.* **2012**, *51* (21), 5179–5182.

(165) Kim, Y.; Hilty, C. Affinity Screening Using Competitive Binding with Fluorine-19 Hyperpolarized Ligands. *Angew. Chem. Int. Ed.* **2015**, *54* (16), 4941–4944.

(166) Hu, S.; Larson, P. E. Z.; VanCriekinge, M.; Leach, A. M.; Park, I.; Leon, C.; Zhou, J.; Shin, P. J.; Reed, G.; Keselman, P.; et al. Rapid Sequential Injections of Hyperpolarized [1-^{13}C]Pyruvate in Vivo Using a Sub-Kelvin, Multi-Sample DNP Polarizer. *Magn. Reson. Imaging* **2013**, *31* (4), 490–496.

(167) Chen, H.-Y.; Hilty, C. Implementation and Characterization of Flow Injection in Dissolution Dynamic Nuclear Polarization NMR Spectroscopy. *ChemPhysChem* **2015**, *16* (12), 2646–2652.

(168) Vulpetti, A.; Dalvit, C. Design and Generation of Highly Diverse Fluorinated Fragment Libraries and Their Efficient Screening with Improved ^{19}F NMR Methodology. *ChemMedChem* **2013**, *8* (12), 2057–2069.

(169) Wang, Z.-X. An Exact Mathematical Expression for Describing Competitive Binding of Two Different Ligands to a Protein Molecule. *FEBS Letters* **1995**, *360* (2), 111–114.

(170) Gullion, T.; Baker, D. B.; Conradi, M. S. New, Compensated Carr-Purcell Sequences. *J. Magn. Reson. (1969)* **1990**, *89* (3), 479–484.

(171) Shaka, A. J.; Rucker, S. P.; Pines, A. Iterative Carr-Purcell Trains. *J. Magn. Reson. (1969)* **1988**, *77* (3), 606–611.

(172) Zweckstetter, M.; Holak, T. A. An Adiabatic Multiple Spin–Echo Pulse Sequence: Removal of Systematic Errors Due to Pulse Imperfections and Off-Resonance Effects. *J. Magn. Reson.* **1998**, *133* (1), 134–147.

(173) Harris, T.; Bretschneider, C.; Frydman, L. Dissolution DNP NMR with Solvent Mixtures: Substrate Concentration and Radical Extraction. *J. Magn. Reson.* **2011**, *211* (1), 96–100.

(174) Noble, M. E. M. Protein Kinase Inhibitors: Insights into Drug Design from Structure. *Science* **2004**, *303* (5665), 1800–1805.

(175) Hantschel, O.; Grebien, F.; Superti-Furga, G. The Growing Arsenal of ATP-Competitive and Allosteric Inhibitors of BCR–ABL. *Cancer Res.* **2012**, *72* (19), 4890–4895.

(176) Duckett, S. B.; Mewis, R. E. Application of *Para* Hydrogen Induced Polarization Techniques in NMR Spectroscopy and Imaging. *Acc. Chem. Res.* **2012**, *45* (8), 1247–1257.

(177) Jensen, P. R.; Meier, S.; Ardenkjær-Larsen, J. H.; Duus, J. Ø.; Karlsson, M.; Lerche, M. H. Detection of Low-Populated Reaction Intermediates with Hyperpolarized NMR. *Chem. Commun.* **2009**, 34, 5168–5170.

(178) Duckett, S. B.; Newell, C. L.; Eisenberg, R. Observation of New Intermediates in Hydrogenation Catalyzed by Wilkinson's Catalyst, $RhCl(PPh_3)_3$, Using Parahydrogen-Induced Polarization. *J. Am. Chem. Soc.* **1994**, *116* (23), 10548–10556.

(179) Platzer, G.; Okon, M.; McIntosh, L. P. PH-Dependent Random Coil 1H, 13C, and 15N Chemical Shifts of the Ionizable Amino Acids: A Guide for Protein PK a Measurements. *J. Biomol. NMR* **2014**, *60* (2–3), 109–129.

(180) Crémillieux, Y.; Goutailler, F.; Montcel, B.; Grand, D.; Vermeulen, G.; Wolf, P.-E. A Super-Wide Bore DNP System for Multiple Sample Polarization: Cryogenic Performance and Polarization at Low Temperature. *Appl. Magn. Reson.* **2012**, *43* (1–2), 167–180.

(181) Krajewski, M.; Wespi, P.; Busch, J.; Wissmann, L.; Kwiatkowski, G.; Steinhauser, J.; Batel, M.; Ernst, M.; Kozerke, S. A Multisample Dissolution Dynamic Nuclear Polarization System for Serial Injections in Small Animals: Multisample Dissolution DNP Polarizer for Small Animals. *Magn. Reson. Med.* **2017**, *77* (2), 904–910.

(182) Kim, Y.; Liu, M.; Hilty, C. Parallelized Ligand Screening Using Dissolution Dynamic Nuclear Polarization. *Anal. Chem.* **2016**, *88* (22), 11178–11183.

(183) Markwardt, F.; Landmann, H.; Walsmann, P. Comparative Studies on the Inhibition of Trypsin, Plasmin, and Thrombin by Derivatives of Benzylamine and Benzamidine. *Eur. J. Biochem.* **1968**, *6* (4), 502–506.

(184) Chappuis, Q.; Milani, J.; Vuichoud, B.; Bornet, A.; Gossert, A. D.; Bodenhausen, G.; Jannin, S. Hyperpolarized Water to Study Protein–Ligand Interactions. *J. Phys. Chem. Lett.* **2015**, *6* (9), 1674–1678.

(185) Bloch, F. Nuclear Induction. *Phys. Rev.* **1946**, *70* (7–8), 460–474.

(186) *Protein NMR Spectroscopy: Principles and Practice*, 2nd ed.; Cavanagh, J., Ed.; Academic Press: Amsterdam ; Boston, 2007.

(187) Ven, F. J. M. van de. *Multidimensional NMR in Liquids: Basic Principles and Experimental Methods*; VCH: New York, 1995.

APPENDIX A

SUPPORTING INFORMATION FOR "PARALLELIZED LIGAND SCREENING

USING DISSOLUTION DYNAMIC NUCLEAR POLARIZATION"[*]

To determine K_D from the R_2 measurements based on competitive binding, two types of experiments need to be performed: (1) the measurement of $R_{2,f}$ and $R_{2,b}{}^*$ and (2) the measurement of $R_{2,obs}$ under competitive. The following tables and figures include the acquired datasets for the measurements (1) and (2) not shown in the corresponding chapter.

A.1. R_2 relaxation decays of hyperpolarized TFBC for $R_{2,f}$ measurements
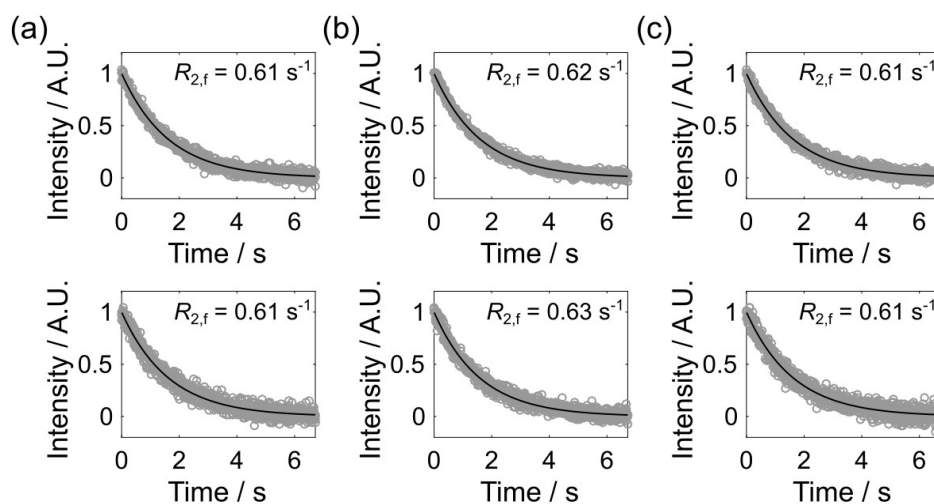
Figure A.1: R_2 relaxation decays of hyperpolarized TFBC obtained from three CPMG experiments without any protein. Each column (a, b and c) represents the same experiment, and each row represents the data acquired from Channels 1 (top) and 2 (bottom). The TFBC signals from 840 successive spin–echoes are shown using gray circles. The fitted curves are indicated by solid lines and the values of $R_{2,f}$ are shown in each graph. The average TFBC concentration was $19.9 \pm 2.3 \ \mu M$.

A.2. R_2 relaxation decays of hyperpolarized TFBC for $R_{2,b}^*$ measurements
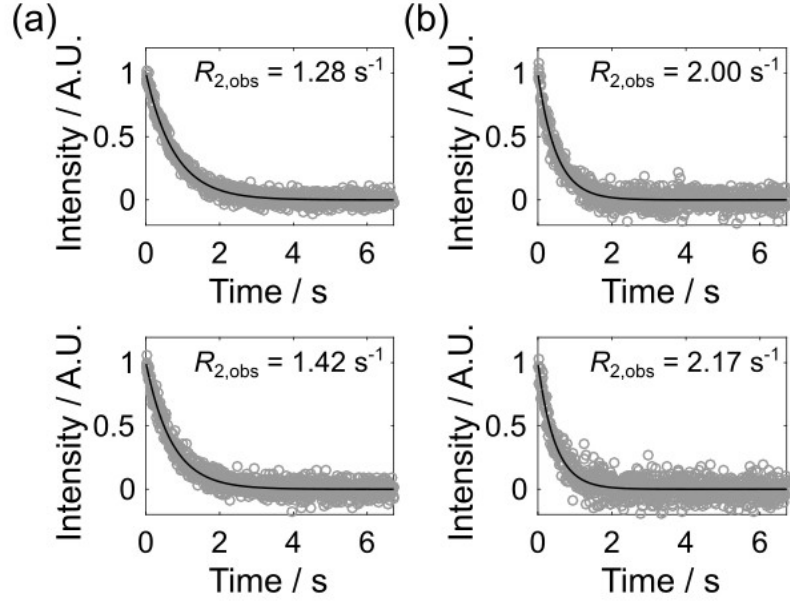
Figure A.2: Example data of R_2 relaxation decays of hyperpolarized TFBC obtained from two CPMG experiments admixing 2 μM (a) and 4 μM (b) trypsin solutions. The TFBC signals from 840 successive spin-echoes are shown using gray circles. The data acquired from Channels 1 and 2 are shown in the top and bottom panels, respectively. The fitted curves are indicated by solid lines and the values of $R_{2,obs}$ are shown in each graph. The final sample concentrations are summarized in Table A.1.

Table A.1: Final protein and ligand concentrations and $R_{2,obs}$

Entry	Channel 1	Channel 2
(a)	[TFBC] = 16.7 μM, [trypsin] = 0.25 μM R_2 = 1.28 s^{-1}	[TFBC] = 18.9 μM, [trypsin] = 0.27 μM R_2 = 1.42 s^{-1}
(b)	[TFBC] = 16.2 μM, [trypsin] =0.52 μM R_2 = 2.00 s^{-1}	[TFBC] = 17.2 μM, [trypsin] = 0.51 μM R_2 = 2.17 s^{-1}
(c)	[TFBC] = 22.9 μM, [trypsin] =0.33 μM R_2 = 1.29 s^{-1}	[TFBC] = 18.3 μM, [trypsin] = 0.25 μM R_2 = 1.32 s^{-1}

Table A.1 Continued

Entry	Channel 1	Channel 2
(d)	[TFBC] = 19.6 μM, [trypsin] =0.57 μM R_2 = 1.95 s^{-1}	[TFBC] = 17.7 μM, [trypsin] = 0.51 μM R_2 = 2.18 s^{-1}
(e)	[TFBC] = 17.4 μM, [trypsin] =0.51 μM R_2 = 1.87 s^{-1}	[TFBC] = 19.1 μM, [trypsin] = 0.27 μM R_2 = 1.41 s^{-1}
(f)	[TFBC] = 20.5 μM, [trypsin] =0.30 μM R_2 = 1.31 s^{-1}	[TFBC] = 19.5 μM, [trypsin] = 0.59 μM R_2 = 2.07 s^{-1}

A total of 6 CPMG experiments were performed admixing the hyperpolarized TFBC to 2 μM and 4 μM trypsin solutions. In Table A.1, the first four entries summarize the results obtained when the same solutions were injected into both channels (a and c: 2 μM trypsin; b and d: 4 μM trypsin), while the last two entries summarize the results obtained when different solutions were used. (e: 4 μM trypsin in Channel 1, and 2 μM trypsin in Channel 2; f: the opposite order of (e)). The entries (a) and (b) correspond to Figure A.1.

A.3. R_2 relaxation decays of hyperpolarized TFBC from competitive binding measurements

A.3.1. Benzamidine

Table A.2: Final protein and ligand concentrations. The entry letters correspond to Figure A.3.

Entry	Channel 1	Channel 2
(a)	[TFBC] = 17.1 μM, [trypsin] = 0.26 μM, [benzamidine] = 13.1 μM	[TFBC] = 17.7 μM, [trypsin] = 0.27 μM,[benzamidine] = 272 μM

Table A.2 Continued

Entry	Channel 1	Channel 2
(b)	[TFBC] = 17.9 μM, [trypsin] = 0.26 μM, [benzamidine] = 13.1 μM	[TFBC] = 17.5 μM, [trypsin] = 0.24 μM, [benzamidine] = 245 μM
(c)	[TFBC] = 17.4 μM, [trypsin] = 0.26 μM, [benzamidine] = 12.9 μM	[TFBC] = 13.9 μM, [trypsin] = 0.25 μM, [benzamidine] = 246 μM

Figure A.3: R_2 relaxation decays of hyperpolarized TFBC competing with benzamidine obtained from three CPMG experiments. Each column (a, b and c) represents the same experiment and each row represents the datasets acquired from Channels 1 and 2 at top and bottom, respectively. The TFBC signals from 840 successive spin–echoes are shown using gray circles. The fitted curves are indicated by solid lines and the values of $R_{2,obs}$ are shown in each graph. Limiting curves for free TFBC ($R_{2,f}$ = 0.62 s^{-1}) (– - –) and maximally bound TFBC, calculated from $R_{2,b}^{*}$, (– –) are shown. Datasets in Figure 4.6a and 4.6b correspond to those in column (a). The final sample concentrations are summarized in Table A.2.

A.3.2. Benzylamine
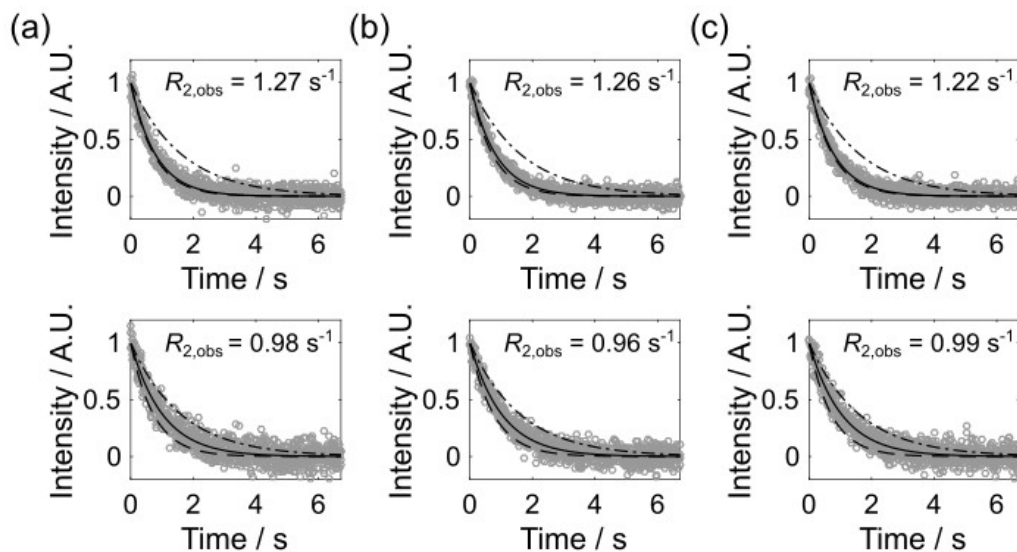
Figure A.4: R_2 relaxation decays of hyperpolarized TFBC competing with benzylamine obtained from three CPMG experiments. Each column (a, b and c) represents the same experiment and each row represents the datasets acquired from Channels 1 and 2 at top and bottom, respectively. The TFBC signals from 840 successive spin–echoes are shown using gray circles. The fitted curves are indicated by solid lines and the values of $R_{2,obs}$ are shown in each graph. Limiting curves for free TFBC ($R_{2,f} = 0.62$ s^{-1}) (– - –) and maximally bound TFBC, calculated from $R_{2,b}$*, (– –) are shown. Datasets in Figure 4.6c and 4.6d correspond to those in column (a). The final sample concentrations are summarized in Table A.3.

Table A.3: Final protein and ligand concentrations. The entry letters correspond to Figure A.4.

Entry	Channel 1	Channel 2
(a)	[TFBC] = 23.1 μM, [trypsin] = 0.31 μM, [benzylamine] = 15.6 μM	[TFBC] = 18.3 μM, [trypsin] = 0.26 μM,[benzylamine] = 258 μM
(b)	[TFBC] = 23.1 μM, [trypsin] = 0.31 μM, [benzylamine] = 15.3 μM	[TFBC] = 19.1 μM, [trypsin] = 0.27 μM, [benzylamine] = 269 μM
(c)	[TFBC] = 19.8 μM, [trypsin] = 0.32 μM, [benzylamine] = 16.2 μM	[TFBC] = 15.1 μM, [trypsin] = 0.23 μM, [benzylamine] = 233 μM

A.4. The $K_{D,c}$ values of benzamidine and benzylamine, and the errors assessed using

Monte Carlo method

Numerical values for $K_{D,c}$ of benzamidine (1) and benzylamine (2) determined by individual and group fitting methods. The results from the error analysis using the Monte Carlo method are summarized. The entry letters correspond to Figure A.3 and Table A.2 for benzamidine, and Figure A.4 and Table A.3 for benzylamine.

A.4.1. Benzamidine

Table A.4: Numerical values of $K_{D,c}$ of benzamidine obtained from the original data and error analysis.

Benzamidine			$K_{D,c}$ (μM) Individual fitting			$K_{D,c}$ (μM) Group fitting
			Channel 1		Channel 2	
Entry	Symbol	Data	Simulation (mean $K_{D,c}$, 95% interval)	Data	Simulation (mean $K_{D,c}$, 95% interval)	Data
(a)	◊	11.9	12.1, (8.3, 19.6)	14.2	14.0, (8.5, 21.2)	12.1
(b)	□	14.2	14.6, (9.6, 25.0)	13.6	13.4, (8.2, 20.4)	13.8
(c)	○	11.7	11.9, (8.1, 19.4)	15.1	14.9, (9.2, 22.5)	12.1

A.4.2. Benzylamine

Table A.5: Numerical values of $K_{D,c}$ of benzylamine obtained from the original data and error analysis.

benzylamine		$K_{D,c}$ (μM) Individual fitting				$K_{D,c}$ (μM) Group fitting
		Channel 1		Channel 2		
Entry	Symbol	Data	Simulation (mean $K_{D,c}$, 95% interval)	Data	Simulation (mean $K_{D,c}$, 95% interval)	Data
(a)	◊	107	103, (36.7, 554)	212	215, (151, 328)	204
(b)	□	104	102, (35.8, 580)	182	184, (133, 269)	176
(c)	○	51.1	56.6, (26.0, 235)	226	230, (159, 360)	196

APPENDIX B

DIRECT OBSERVATION OF RU-ALKYLIDENE FORMING INTO ETHYLENE IN

RING-CLOSING METATHESIS FROM HYPERPOLARIZED ^{1}H NMR[*]

B.1. Introduction

Olefin metathesis is a class of carbon redistribution reactions widely applied in organic synthesis.[1,2] The mechanism of transition metal catalysts for olefin metathesis involves an alkene double bond undergoing [2+2] cycloaddition with a metal alkylidene to form a metallocyclobutane intermediate. Subsequent bond cleavage produces a new olefin and a new metal alkylidene, which propagates the reaction.[3,4] Metathesis can increase efficiency by shortening routes to products and requiring fewer resources than traditional synthetic schemes.[5] It is applied in the petrochemical industry for propylene production from C4 olefin feedstock and ethylene.[6] In the polymer field, polynorbornene and polycyclopentadiene are commercially produced by a ring-opening metathesis polymerization.[6] The adoption of metathesis in pharmaceuticals has emerged in recent years as various types of metathesis catalysts have been developed for improving functional group tolerances and increasing catalyst stability.[7,8]

Among metathesis catalysts, a family of N-heterocyclic carbene-coordinated ruthenium complexes originally described by Grubbs is well known for their high activity and stability.[9] Studies to understand the mechanisms for the catalyzed reaction and deactivation of catalysts have aimed at determining structures and identities of the

---

ruthenium-bound intermediate species. Species such as Ru-alkylidene (Ru=CH(R), R stands for H) can be stabilized by introducing a large excess of inhibitors or catalyst precursors. Using these methods, compounds similar to those produced during the catalytic reaction can be observed.[10–13] However, the actual intermediates arising in the reaction may be unstable, which prevents their isolation. Using *in situ* reactions, it is possible to observe such compounds by NMR spectroscopy, albeit often without the possibility to determine their identity or structure.

Here, we apply stopped-flow NMR of hyperpolarized reagents to characterize an intermediate in the ring-closing metathesis (RCM) reaction of diethyl diallylmalonate (DEDAM) catalyzed by Grubbs' third generation (G3) catalyst. Hyperpolarization by dissolution dynamic nuclear polarization (D-DNP) enhances NMR signals by more than three orders of magnitude in the liquid state.[14] It is achieved by first freezing the sample at a temperature of ~1 K, and irradiating with microwaves in the presence of a magnetic field. The sample incorporates target molecules and free radicals in a matrix that forms a glass at a low temperature. Under these conditions, a high electron spin polarization from the radicals transfers to nuclear spins of interest. By rapidly dissolving the thus hyperpolarized sample in a preheated solvent, the nuclear spin polarization can be preserved for immediate use in liquid state NMR at ambient temperature. With this hyperpolarized liquid, the direct observation of transient or low-populated species in ongoing reactions can be achieved with high sensitivity.[15] Reactions that occur within a time period on the order of seconds are best suited for study using D-DNP. Within this time window determined by the longitudinal relaxation time (T_1), a high signal can be obtained by this method. The applicability of real-time D-DNP enhanced NMR to various

reactions has been demonstrated, including chemical polymerization reactions or enzyme-catalyzed conversions of biological substrates.[16–19]

Unlike most conventional NMR experiments, hyperpolarization by D-DNP creates the spin population difference that results in NMR signals only at the beginning of the experiment. This spin polarization can be used to correlate chemical shifts between reactant and reaction product, as atoms transfer from one species to another. We have previously shown that these correlations can be obtained by applying selective spin inversion pulses to one of the reactants.[18–20] The population inversion of the selectively addressed spin then transfers to the reaction product, thereby establishing the correlation. However, the fate of lowly populated intermediates, such as those arising in this metathesis reaction, cannot be followed using single inversion pulses. We now introduce a method allowing the continuous selective saturation of such an intermediate signal, while at the same time acquiring real-time NMR spectra during the entire progress of the reaction. The observation of NMR signal changes in a species formed from an irradiated precursor species is reminiscent of the technique of Chemical Exchange Saturation Transfer (CEST).[21] In CEST, however, the irradiated and observed species are in chemical equilibrium, whereas the presently described method is suitable for non-equilibrium systems. Using this method, we show that an observed signal from a metal bound intermediate transfers to a specific reaction product, ethylene. Based on this observation, we identify a Ru-alkylidene complex as the observable intermediate.

B.2. Materials and methods

B.2.1. Dynamic nuclear polarization

For hyperpolarization, a mixture of pure diethyl diallylmalonate (DEDAM) and 30 mM 2,2,6,6-tetramethylpiperidine-1-oxyl (TEMPO; Sigma-Aldrich, St. Louis, MO) in isooctane was prepared at a volume ratio of 1:1. Isooctane is a solvent, which forms an amorphous glass when frozen. Aliquots of 20 μL of this mixture were hyperpolarized on ^{1}H in a HyperSense DNP polarizer (Oxford Instruments, Abingdon, U.K.) by irradiating 94.005 GHz microwaves with 100 mW power for 15 min at a temperature of 1.4 K. The hyperpolarized sample was rapidly dissolved with 4 mL of dry toluene, which was preheated to 145 °C, and then transferred into an NMR tube located in the NMR magnet by an injection system using pressurized argon gas.[1] The tubing used for injection was purged with argon gas before each experiment. For the metathesis reactions, 50 μL of 11.3 mM dichloro[1,3-bis(2,4,6-trimethylphenyl)-2-imidazolidinylidene](benzylidene)bis(3-bromopyridine)ruthenium(II) (3rd generation Grubbs catalyst, G3 catalyst; Sigma-Aldrich) in toluene was pre-loaded in the NMR tube under dry argon atmosphere in a glovebox. The final sample concentrations after the dissolution were estimated to be 35 mM DADEM and 1.5 mM catalyst before the reaction occurred based on the volume of injected sample (~ 380 μL) and the sample recovery (~ 32 %) after the dissolution.

B.2.2. NMR spectroscopy

The hyperpolarized ^{1}H NMR spectra were acquired on a Bruker 400 MHz NMR spectrometer equipped with a broadband probe containing three pulsed field gradients (Bruker Biospin, Billerica, MA) at a temperature of 298 K. NMR measurements were

triggered after the injection of hyperpolarized DEDAM into the NMR tube for 560 ms and a stabilization time of 400 ms. The time-resolved ^{1}H NMR spectra were measured using the pulse sequence (trigger – [shaped 90° – Gz]$_{\times 3}$ – [Gz – αx – acquire]$_{\times 64}$). The pulse sequence started with three EBURP2 shaped 90º pulses, each for 10 ms, to suppress the hyperpolarized isooctane signals, followed by a randomized pulsed field gradient, Gz (35.5 G/cm, 2 ms). A small flip angle pulse with flip angle $\alpha = 16.5°$ and pulse strength $\gamma B_1/(2\pi) = 22.1$ kHz was applied for NMR detection. The pulsed field gradient was applied before this pulse to remove the residual coherence from the previous scan.

The pulse sequence designed for the selective saturation experiments was implemented with the saturation pulse scheme during acquisition using the programmatic syntax for homonuclear decoupling (HD), as described in Figure B.1a. The saturation pulses were applied with a field strength of $\gamma B_1/(2\pi) = 26.5$ Hz and at 10 % duty cycle. The cycle time for the series of saturation pulses was approximately 22 μs (Figure B.1b) The transmitter frequency was set to the resonance frequency targeted for the selective saturation. This frequency was chosen as the frequency of the observed intermediate in on-resonance experiments, and at an equal frequency difference to product peaks (= 5,631 Hz), but at the opposite end of the spectrum in off-resonance experiments. The solvent signals were saturated using the aforementioned EBUPR2 pulses before the first scan. A total of 64 spectra were acquired by applying a series of small flip angle ($\alpha = 15°$) pulses. Each scan was composed of 12,818 data points, collected for 400 ms. All NMR spectra were calibrated to the chemical shift of methyl protons of toluene at 2.11 ppm. A non-hyperpolarized NMR spectrum of styrene in toluene was acquired by saturating the

toluene resonance with continuous radio-frequency irradiation, followed by a 90° pulse for signal detection.
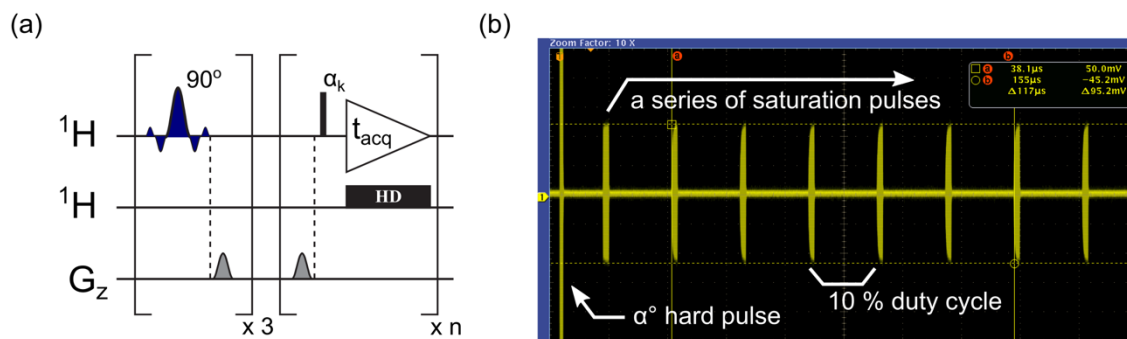
Figure B.1: (a) Selective saturation pulse sequence used for acquiring time-resolved pseudo 2D ^{1}H NMR spectra implemented with HD syntax. (b) Oscilloscope measurement of the attenuated radio-frequency pulse voltage from the HD scheme.

B.2.3. Characterization of selective saturation pulses

The capability of the selective saturation scheme to saturate the target spin during acquisition was investigated. First, the time-dependent saturation effect was assessed by varying the acquisition time, using the pulse sequence in Figure B.2a. Various acquisition times between 20 – 600 ms were tested on the methyl protons of toluene as target spins. For control experiments, the experiments were repeated with zero power for the saturation pulses. The resulting signal intensities from the on-resonance and control experiments are indicated by red and blue circles, respectively, in Figure B.2b. It can be seen that less than 10% of the signal remained when the acquisition time was 200 ms, and that less than 3% of the signal intensity remained when the acquisition time was 400 ms.
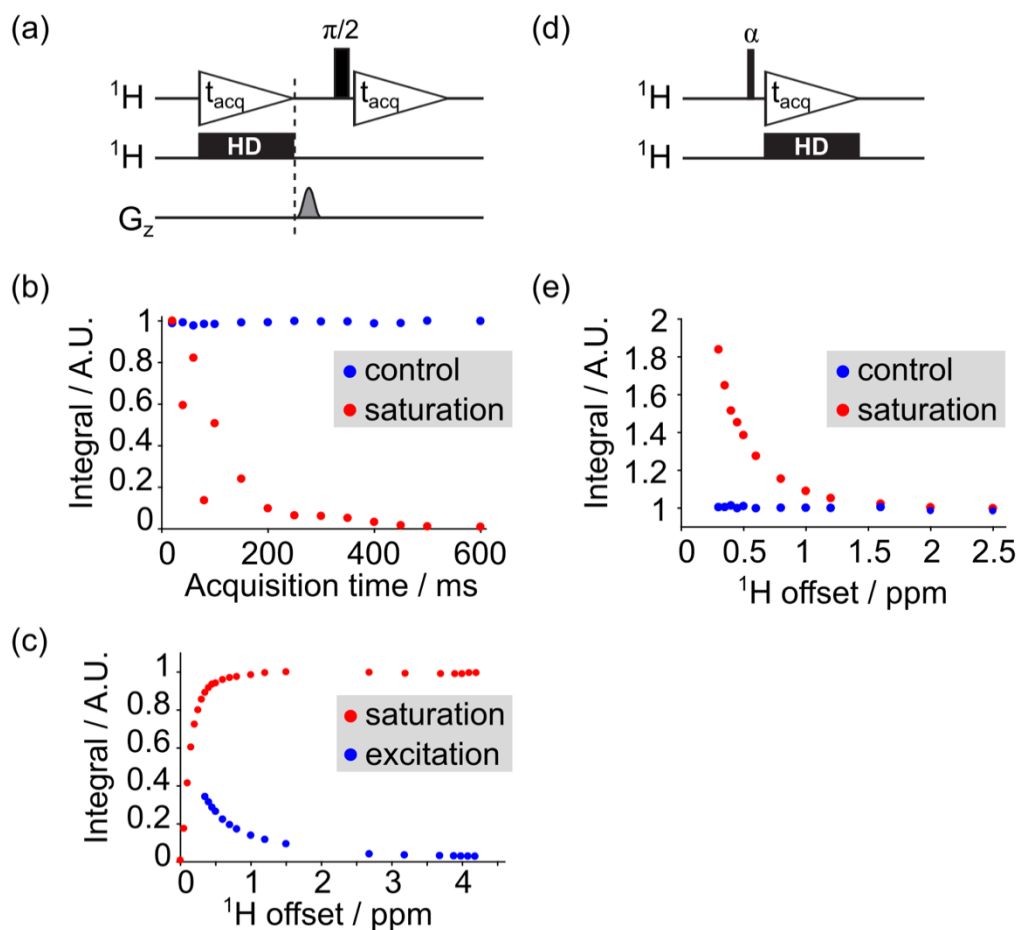
Figure B.2: (a) Pulse sequence used for measuring time-dependent saturation and saturation width (b) Resulting profile of time-dependent saturation as a function of acquisition time (c) Saturation and excitation profiles of selective saturation obtained using 400 ms saturation time (d) Pulse sequence used for measuring the combined pulse effect caused by a small flip angle (α°) hard pulse and saturation pulses. (e) Resulting profile for the combined pulse effect with 400 ms saturation time. The sample was toluene in all measurements.

Next, the saturation width was examined by applying the saturation pulses to the methyl protons with several different offsets, having 400 ms of acquisition time. The same pulse sequence was used, which allows acquiring two free induction decays (FID) from a single measurement; one from the saturation block and the other obtained immediately after a 90° pulse. It is apparent from the first FIDs that the nuclear spins can be excited by the saturation pulses. The signal intensities were normalized to the signal intensity obtained from a single 90° pulse excitation. When the offset was greater than 1.5 ppm with respect to the frequency of the target signal, less than 10 % of the signal remained (blue circles in Figure B.2c). A narrow saturation width was observed from the second FIDs (red circles in Figure B.2c). More than 98 % of the signal was obtained with an offset of 1 ppm. The full width at half maximum of the saturation profile was approximately 0.25 ppm (= 100 Hz). The combined effect from a 15° pulse followed by the selective saturation pulses was examined using the pulse sequence shown in Figure B.2d. This sequence is the same as the one used for selective saturation experiments with hyperpolarized spins, without a loop for acquiring a series of scans. The measurements were carried out at several different offsets with and without the saturation pulse power. As shown in Figure B.2e, the signal intensities were higher than those measured from the control experiments, when the offset was less than 2 ppm. This observation indicates that the spins were further excited by the saturation pulses, presumably because the hard excitation pulse was not a full 90° pulse. This effect subsided as the offset increased and became negligible when the offset was larger than 2 ppm.

B.3. Results and discussion

Figure B.3 shows the spectra acquired after rapidly mixing ^{1}H hyperpolarized

DEDAM with G3 catalyst. The reaction occurring *in situ* in the NMR spectrometer was
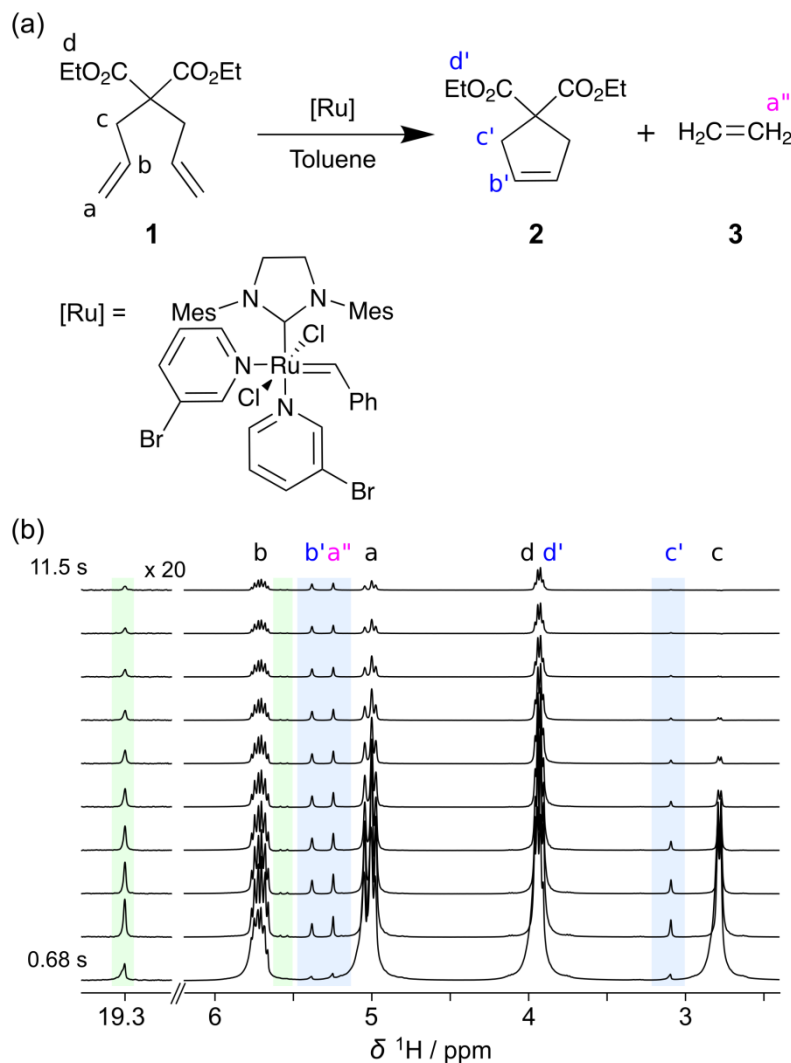
Figure B.3: (a) Reaction scheme of DEDAM metathesis. Mes = 2,4,6-tri-methylphenyl (b) Time-resolved ^{1}H NMR spectra of hyperpolarized DEDAM **1** in a reaction with G3 catalyst ([Ru]). Every third acquired spectrum is shown from a dataset with an acquisition delay of 400 ms. The first spectrum shows a larger line width due to sample settling immediately following injection.

thereby monitored in real-time by acquiring spectra every 400 ms using a small flip angle pulse (16.5° flip angle). The observed signal evolution in the series of hyperpolarized NMR spectra is the result of the combined effects of consumption or production of a species, and loss of hyperpolarization through T_1 spin relaxation. The strong signals observed at 5.00 (a), 5.72 (b), 2.78 (c) and 3.93 (d) ppm stem from the hyperpolarized reactant protons. The signals of products were detected at 5.38 (b') and 3.09 ppm (c') for diethyl 3-cyclopentene-1,1-dicarboxylate (**2**, cyclopentene) and 5.25 ppm (a'') for ethylene **3**. Additional signals, visible in the spectra, which pertain neither to the reactant nor the products **2** and **3**, include a doublet at 5.56 ppm and a singlet at 19.32 ppm. Both of these signals as well as the reaction products initially grow and decay at a later time. Considering the signal enhancements provided by hyperpolarization, all of these observable resonances are expected to stem from the originally hyperpolarized DEDAM rather than from other, non-hyperpolarized reaction components. The possible structures corresponding to these additional peaks can be found from the established reaction mechanism of the RCM.[22,23] The movement of hyperpolarized protons originating from DEDAM throughout the reaction is shown in Figure B.4a. In the figure, the first ruthenium containing species shown is Ru=CH(Ph), which stands for the activated catalyst [(H$_2$IMes)(Cl)$_2$Ru=CH(Ph)]. The G3 catalyst is one of the fastest-initiating ruthenium catalysts.[24,25] It can be assumed that the activation, which starts as soon as the hyperpolarized DEDAM is admixed, is completed before the first NMR spectrum is acquired. As displayed in the figure, the first reaction product of the hyperpolarized =CH$_2$ protons is styrene. The observed signal at 5.56 ppm, by comparing chemical shift and *J*-coupling constant to a reference, is the

proton *cis* to the phenyl ring of styrene (Figure B.4b). The *trans* protons overlap with the intense reactant peaks nearby. The *geminal* proton near 6.5 ppm is not visible in the hyperpolarized experiments. This proton originates from the non-hyperpolarized catalyst.
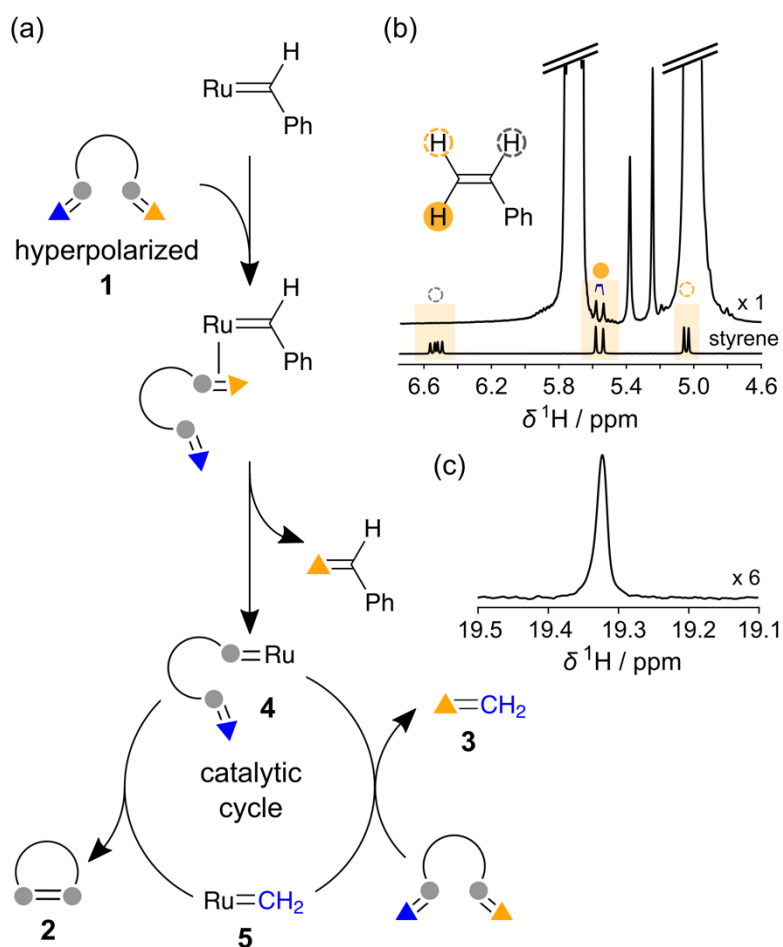
Figure B.4: (a) Mechanism of RCM reaction.[22,23] Terminal and internal olefin protons of hyperpolarized DEDAM are indicated by triangles and circles, respectively, to show the movement of these protons throughout the RCM reaction. (**4**: (H$_2$IMes)(Cl)$_2$Ru=CH(CH$_2$C(CO$_2$Et)$_2$CH$_2$CH=CH$_2$), **5**: (H$_2$IMes)(Cl)$_2$Ru=CH$_2$) (b) Part of the ^{1}H hyperpolarized NMR spectrum (Figure B.3b) containing styrene peaks. The spectrum of non-hyperpolarized styrene in toluene is displayed below for reference. Open and closed circles indicate the peak assignments. (c) Hyperpolarized ^{1}H NMR signal of Ru-alkylidene complex is from the second bottom-most spectrum in Figure B.3b.

The absence of its signal further confirms that the observed signals are from the originally hyperpolarized reactant.

The signal at 19.32 ppm, based on chemical shift, stems with a high likelihood from a Ru-alkylidene (such as **4** or **5** in Figure B.4a). In the following, we aim to establish the identity of this compound by determining the fate of the observed protons transferring to the final product molecules. A selective saturation was applied to this signal, using radio-frequency pulses interleaved with the acquisition of each successive data point of the free induction decay. Pulsing interleaved with acquisition enables a continuous and selective spin saturation of reaction intermediates. Saturation extends over the entire duration of the measurement time, which consists of multiple scans after the injection of the DNP hyperpolarized compound. This pulse scheme was implemented on the NMR spectrometer using the programmatic syntax for homonuclear decoupling (HD), although the goal of the application is different from decoupling. We tested the capability of this scheme to saturate the target spin, and thereby remove its signal from the NMR spectrum, using a stationary sample as described in the supporting information. With saturation for 400 ms at a duty cycle of 10 % and a pulse strength of $\gamma B_1/(2\pi) = 26.5$ Hz (0.12 % of the hard pulse strength), less than 5 % of the signal remained after saturation. The selective saturation showed a narrow saturation width at half height of approximately 0.25 ppm. It further partially excited the spins within $\pm$ 2 ppm, which is necessary to take account of when interpreting the data.

The selective saturation provides an effect in the spectrum similar to blocking the pathway of the saturated spins. The reaction itself is not affected; rather, the spin polarization is altered to visualize the reaction progress. One spectrum from a series of

145

scans acquired under continuous application of saturation to the species observed at 19.32 ppm is shown in Figure B.5a. This spectrum can be compared to a reference with off-resonance saturation applied at the opposite end of the spectrum. A spike observed at the frequency of selective saturation is due to the remaining electrical signal from pulsing. In the superposition of the two normalized spectra (Figure B.5b), the observed differences are shaded. It can be seen that a single product signal, that of ethylene, is noticeably affected by the saturation. In contrast, the intensities of cyclopentene or DEDAM protons are almost identical in both datasets. The effect of the saturation can be seen even more clearly in the time dependence of signal intensities from all scans of the experiments, in Figure B.5c.

The signal decays of the reactant protons and the signal buildup curves of cyclopentene in the on- and off-resonance saturation experiments are nearly identical. In the same experiments, only the signal buildup of ethylene was affected by the on-resonance saturation. The signal of ethylene in the series of spectra with on-resonance irradiation follows the off-resonance series, but shows a smaller initial increase and more rapid reduction. This indicates that the protons observed at 19.32 ppm transfer to the reaction product ethylene. This species can therefore be identified as a reaction intermediate related to Ru-alkylidene (**5**). The protons of **4** would also be in the hyperpolarized spin state, but were not observed in the spectra with or without saturation. The absence of these signals is likely due to a short lifetime of the corresponding complex **4**, which undergoes ring closure by intramolecular [2+2] cycloaddition to give **2** and regenerates **5**.
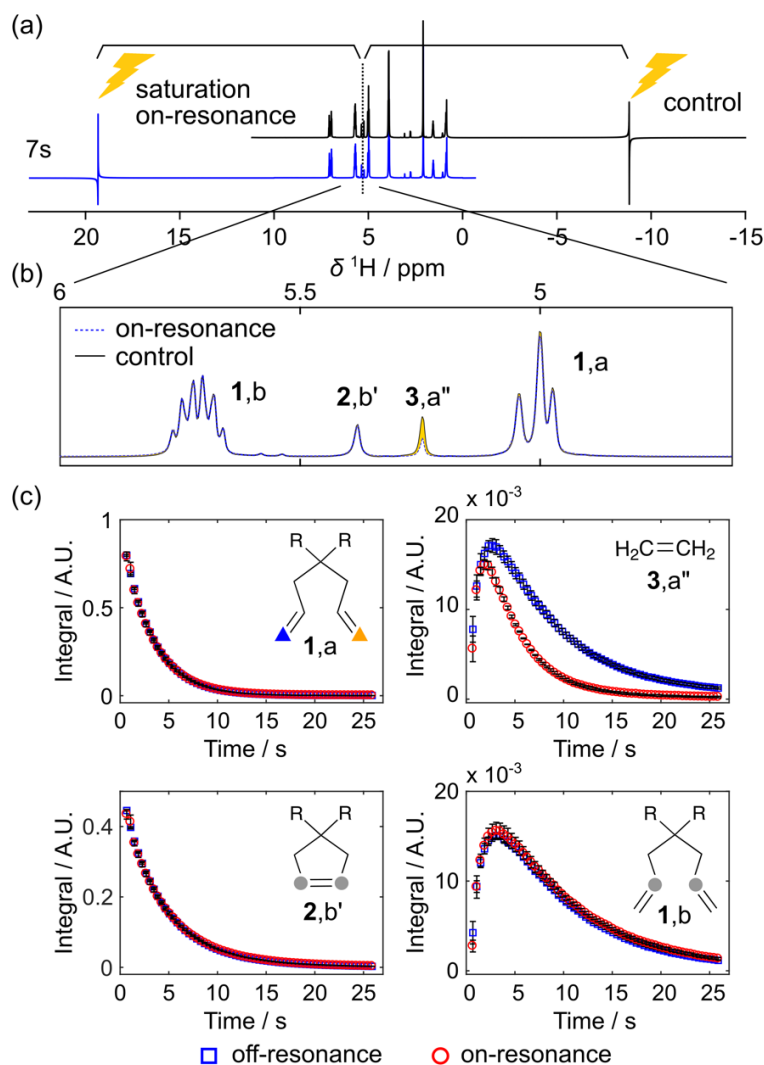
Figure B.5: Selective saturation experiment, with on-resonance irradiation of the ^{1}H signal at 19.32 ppm. A second dataset includes off-resonance saturation at an identical frequency difference to product peaks, but at the opposite end of the spectrum. The two spectra were obtained in the 17th scan, 7 seconds after injection of the hyperpolarized reactant and start of the reaction. (b) Overlay of the spectra with on- and off-resonance saturation plotted between 4.6 and 6 ppm. The shading indicates the difference between the two spectra. The peaks are assigned as labeled in Figure B.3a. (c) Signal integrals of reactant and product protons from the selective saturation experiments, obtained by fitting peaks with Lorentzian shapes. The data points represent averages and error bars indicate the standard deviations from three repetitions. For data normalization, the signal decay of terminal olefin protons of the DEDAM was fit to a single exponential, and the extrapolated intensity at $t = 0$ was scaled to unit intensity. In all datasets, the scaling factors were determined with a 2% error or less, and they varied with a standard deviation of 19%. (R $= –CO_2Et$)

The initial increase of signals contains information on initial formation rates of products. These signal buildup rates can be used to obtain kinetic information about the reaction if relaxation rates are known.[26] In the RCM reaction performed, the signal for the product **2** or **3** showed a slower buildup than that for styrene (Figure B.6). Also, considering that the doublet styrene signal corresponds to a single proton *cis* to the phenyl ring, the signal for Ru-alkylidene, likely comprising two protons, shows a slower buildup than that for styrene. This observation would be consistent with a faster initial rate of
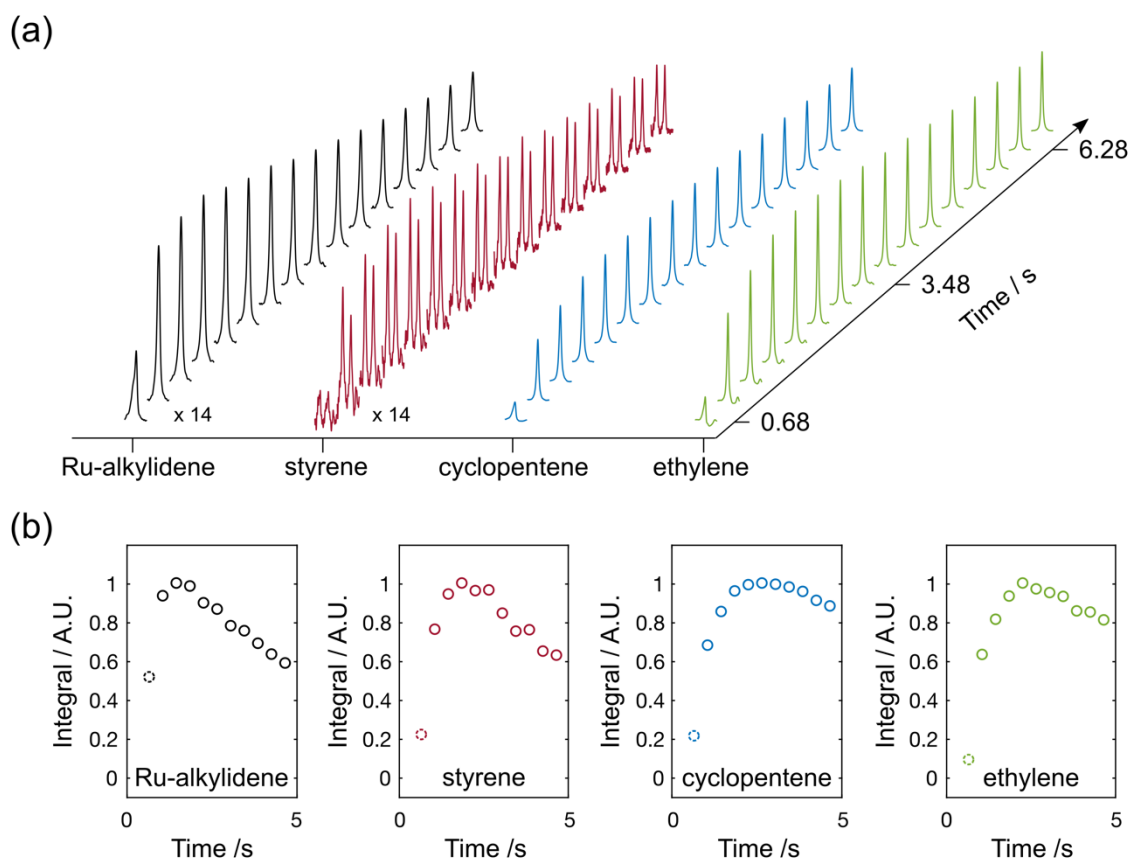
Figure B.6: (a) Time resolved ^{1}H NMR signals of reaction products from the RCM reaction. The signals were processed by applying a linear or polynomial baseline correction. (b) Signal integrals of reaction products from the spectra shown in (a). The maximum signal integral in each plot was scaled to unit intensity. The first data points are shown with dotted circles which indicate less accuracy caused by a broader line width and low signal intensity.

formation of styrene predicted from the scheme in Figure B.4a. A quantitative kinetic analysis of this multi-step reaction would, however, require knowledge of additional rates and is not attempted here.

The signal at 19.32 ppm is the only Ru-alkylidene signal observed, likely stemming from the species with the longest lifetime. Since saturation is transferred from this species to the ethylene product, it is implied that its conversion is the rate-limiting step in this branch of the reaction. The actual structure of this species cannot be determined from the single NMR signal. However, since the propagating species $(H_2IMes)(Cl)_2Ru=CH_2$ (**5**) is highly reactive,[12,27,28] it appears more likely that the observable Ru-alkylidene species is a coordination complex with an olefin or with a 3-
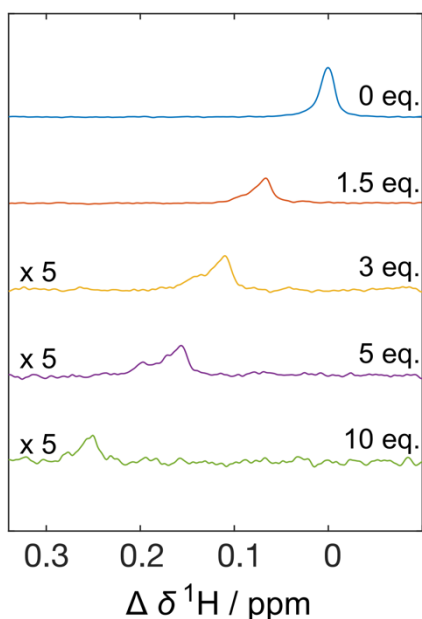
Figure B.7: The hyperpolarized ^1H NMR spectra showing the chemical shift changes of observable Ru-alkylidene complex, obtained from the third scans of a series of spectra from the RCM reaction with varying bromopyridine (**py**) concentrations. The equivalents of the added **py** in each spectrum are indicated in the figure. The chemical shifts are referenced to the CH_3 proton of toluene and shown as the change from the value in the reaction without any added **py**.

bromopyridine ligand dissociated from the precatalyst. Based on this reasoning, the effect of the addition of excess bromopyridine to the experiment was tested (Figure B.7).

This addition caused a downfield shift of the Ru-alkylidene signal, which would be consistent with a coordination/decoordination equilibrium of bromopyridine with the Ru=CH$_2$ complex (**5**). An influence of pyridine coordination to the propagating ruthenium complex has previously been reported for the related ring-opening metathesis polymerization reaction.[29,30]

B.4. Conclusions

In summary, we have demonstrated that continuous saturation interleaved with the acquisition of real-time D-DNP NMR spectra can be used to follow the conversion of a transient intermediate to the reaction product. Thereby, the destination of the saturated proton can unequivocally be identified. Applied to the ring-closing metathesis of DEDAM by G3 Grubbs catalyst, this saturation method allowed to observe a Ru-alkylidene intermediate that appears in the ethylene production pathway. Here, the intermediate signal is well separated from those of the reaction products, but the method can still be applied in other cases by accounting for pulse effects using on- and off-resonance saturation at symmetric positions with respect to the observed product. Continuous saturation can also be applied more generally to complex reactions that produce multiple intermediates, to directly observe the transfer of atoms between species. Saturation can be applied when the intermediate signal is undetectable in a spectrum due to low signal-to-noise ratio. It may therefore further be used to find resonance frequencies of unobservable intermediates to provide structural and mechanistic information pertaining to a reaction.

<center>B.5. References</center>

(1)   Hoveyda, A. H.; Zhugralin, A. R. The Remarkable Metal-Catalysed Olefin Metathesis Reaction. *Nature* **2007**, *450* (7167), 243–251.

(2)   Monfette, S.; Fogg, D. E. Equilibrium Ring-Closing Metathesis. *Chem. Rev.* **2009**, *109* (8), 3783–3816.

(3)   Hérisson, J.-L.; Chauvin, Y. Catalysis of Olefin Transformations by Tungsten Complexes. II. Telomerization of Cyclic Olefins in the Presence of Acyclic Olefins. *Macromol. Chem. Phys.* **1971**, No. 141, 161–167.

(4)   Nelson, D. J.; Manzini, S.; Urbina-Blanco, C. A.; Nolan, S. P. Key Processes in Ruthenium-Catalysed Olefin Metathesis. *Chem. Commun.* **2014**, *50* (72), 10355–10375.

(5)   Dwyer, C. L. Metathesis of Olefins. In *Metal-catalysis in Industrial Organic Processes*; Royal Society of Chemistry, 2007; pp 201–217.

(6)   Mol, J. C. Industrial Applications of Olefin Metathesis. *J. Mol. Catal. A: Chem.* **2004**, *213* (1), 39–45.

(7)   Higman, C. S.; Lummiss, J. A. M.; Fogg, D. E. Olefin Metathesis at the Dawn of Implementation in Pharmaceutical and Specialty-Chemicals Manufacturing. *Angew. Chem. Int. Ed.* **2016**, *55* (11), 3552–3565.

(8)   Grubbs, R. H.; O'Leary, D. J. *Handbook of Metathesis, Volume 2: Applications in Organic Synthesis*; John Wiley & Sons, 2015.

(9)   Vougioukalakis, G. C.; Grubbs, R. H. Ruthenium-Based Heterocyclic Carbene-Coordinated Olefin Metathesis Catalysts. *Chem. Rev.* **2010**, *110* (3), 1746–1787.

<center>151</center>

(10)   Dias, E. L.; Nguyen, S. T.; Grubbs, R. H. Well-Defined Ruthenium Olefin Metathesis Catalysts: Mechanism and Activity. *J. Am. Chem. Soc.* **1997**, *119* (17), 3887–3897.

(11)   Hong, S. H.; Wenzel, A. G.; Salguero, T. T.; Day, M. W.; Grubbs, R. H. Decomposition of Ruthenium Olefin Metathesis Catalysts. *J. Am. Chem. Soc.* **2007**, *129* (25), 7961–7968.

(12)   van der Eide, E. F.; Romero, P. E.; Piers, W. E. Generation and Spectroscopic Characterization of Ruthenacyclobutane and Ruthenium Olefin Carbene Intermediates Relevant to Ring Closing Metathesis Catalysis. *J. Am. Chem. Soc.* **2008**, *130* (13), 4485–4491.

(13)   P'Poo, S. J.; Schanz, H.-J. Reversible Inhibition/Activation of Olefin Metathesis: A Kinetic Investigation of ROMP and RCM Reactions with Grubbs' Catalyst. *J. Am. Chem. Soc.* **2007**, *129* (46), 14200–14212.

(14)   Ardenkjær-Larsen, J. H.; Fridlund, B.; Gram, A.; Hansson, G.; Hansson, L.; Lerche, M. H.; Servin, R.; Thaning, M.; Golman, K. Increase in Signal-to-Noise Ratio of > 10,000 Times in Liquid-State NMR. *Proc. Natl. Acad. Sci. U.S.A.* **2003**, *100* (18), 10158–10163.

(15)   Jensen, P. R.; Meier, S.; Ardenkjær-Larsen, J. H.; Duus, J. Ø.; Karlsson, M.; Lerche, M. H. Detection of Low-Populated Reaction Intermediates with Hyperpolarized NMR. *Chem. Commun.* **2009**, No. 34, 5168–5170.

(16)   Hilty, C.; Bowen, S. Applications of Dynamic Nuclear Polarization to the Study of Reactions and Reagents in Organic and Biomolecular Chemistry. *Org. Biomol. Chem.* **2010**, *8* (15), 3361–3365.

(17)   Meier, S.; Jensen, P. R.; Karlsson, M.; Lerche, M. H. Hyperpolarized NMR Probes for Biological Assays. *Sensors* **2014**, *14* (1), 1576–1597.

(18)   Lee, Y.; Heo, G. S.; Zeng, H.; Wooley, K. L.; Hilty, C. Detection of Living Anionic Species in Polymerization Reactions Using Hyperpolarized NMR. *J. Am. Chem. Soc.* **2013**, *135* (12), 4636–4639.

(19)   Chen, C.-H.; Shih, W.-C.; Hilty, C. In Situ Determination of Tacticity, Deactivation, and Kinetics in [Rac-(C$_2$H$_4$(1-Indenyl)$_2$)ZrMe][B(C$_6$F$_5$)$_4$] and [Cp$_2$ZrMe][B(C$_6$F$_5$)$_4$]-Catalyzed Polymerization of 1-Hexene Using ^{13}C Hyperpolarized NMR. *J. Am. Chem. Soc.* **2015**, *137* (21), 6965–6971.

(20)   Bowen, S.; Hilty, C. Temporal Chemical Shift Correlations in Reactions Studied by Hyperpolarized Nuclear Magnetic Resonance. *Anal. Chem.* **2009**, *81* (11), 4543–4547.

(21)   Goffeney, N.; Bulte, J. W. M.; Duyn, J.; Bryant, L. H.; van Zijl, P. C. M. Sensitive NMR Detection of Cationic-Polymer-Based Gene Delivery Systems Using Saturation Transfer via Proton Exchange. *J. Am. Chem. Soc.* **2001**, *123* (35), 8628–8629.

(22)   Armstrong, S. K. Ring Closing Diene Metathesis in Organic Synthesis. *J. Chem. Soc., Perkin Trans. 1* **1998**, *1* (2), 371–388.

(23)   Urbina-Blanco, C. A.; Poater, A.; Lebl, T.; Manzini, S.; Slawin, A. M. Z.; Cavallo, L.; Nolan, S. P. The Activation Mechanism of Ru–Indenylidene Complexes in Olefin Metathesis. *J. Am. Chem. Soc.* **2013**, *135* (18), 7073–7079.

(24)   Love, J. A.; Morgan, J. P.; Trnka, T. M.; Grubbs, R. H. A Practical and Highly Active Ruthenium-Based Catalyst That Effects the Cross Metathesis of Acrylonitrile. *Angew. Chem. Int. Ed.* **2002**, *41* (21), 4035–4037.

(25)   Choi, T.-L.; Grubbs, R. H. Controlled Living Ring-Opening-Metathesis Polymerization by a Fast-Initiating Ruthenium Catalyst. *Angew. Chem. Int. Ed.* **2003**, *42* (15), 1743–1746.

(26)   Zeng, H.; Lee, Y.; Hilty, C. Quantitative Rate Determination by Dynamic Nuclear Polarization Enhanced NMR of a Diels−Alder Reaction. *Anal. Chem.* **2010**, *82* (21), 8897–8902.

(27)   Eide, E. F. van der; Piers, W. E. Mechanistic Insights into the Ruthenium-Catalysed Diene Ring-Closing Metathesis Reaction. *Nat. Chem.* **2010**, *2* (7), 571–576.

(28)   Romero, P. E.; Piers, W. E. Direct Observation of a 14-Electron Ruthenacyclobutane Relevant to Olefin Metathesis. *J. Am. Chem. Soc.* **2005**, *127* (14), 5032–5033.

(29)   Walsh, D. J.; Lau, S. H.; Hyatt, M. G.; Guironnet, D. Kinetic Study of Living Ring-Opening Metathesis Polymerization with Third-Generation Grubbs Catalysts. *J. Am. Chem. Soc.* **2017**, *139* (39), 13644–13647.

(30)   Chang, A. B.; Lin, T.-P.; Thompson, N. B.; Luo, S.-X.; Liberman-Martin, A. L.; Chen, H.-Y.; Lee, B.; Grubbs, R. H. Design, Synthesis, and Self-Assembly of Polymers with Tailored Graft Distributions. *J. Am. Chem. Soc.* **2017**, *139* (48), 17683–17693.

PHYSICAL BACKGROUND OF NMR SPECTROSCOPY

C.1. Quantum mechanical description of NMR

Nuclear magnetic resonance (NMR) spectroscopy relies on a magnetic property of an atomic nucleus which arises from an intrinsic angular momentum **I** of a nuclear spin. In quantum mechanics, this spin angular momentum is characterized by a nuclear spin quantum number, I. The nuclear spins with $I \neq 0$ possess a magnetic dipole moment **μ**, which interacts with a magnetic field; in other words, the nuclear spins with $I = 0$ are not active in NMR. The relationship between **I** and **μ** can be written in terms of quantum mechanical operators:

$$\hat{\mu} = \gamma \hat{I} \tag{C.1}$$

where the corresponding operators for **I** and **μ** are denoted with "hats" and γ is the gyromagnetic ratio of a nucleus.

When the nucleus is introduced to a static magnetic field B_0, the interaction between the magnetic dipole moment and the magnetic field, called Zeeman interaction, occurs, and it breaks down a degeneracy of nuclear spin energy states. The Zeeman interaction energy is determined by the Hamiltonian operator $\hat{H}$:

$$\hat{H} = -\hat{\mu}_z \cdot B_0 = -\gamma B_0 \hat{I}_z \tag{C.2}$$

Here, the z-component of the magnetic dipole moment μ_z or spin angular momentum I_z is considered since the direction of the static magnetic field in NMR spectroscopy is typically along the z-axis. The eigenvalue of $\hat{I}_z$ is $m\hbar$ where $\hbar$ is the Plank constant

divided by 2π and m is a magnetic quantum number with $2I + 1$ values ranging from $-I$ to $+I$ in steps of one. Then, the eigenvalue of $\widehat{\mathcal{H}}$ becomes $E_m = -\gamma B_0(m\hbar)$, resulting in forming $2I + 1$ energy levels separated by $\Delta E = -\gamma\hbar B_0$ between the successive levels. For a spin one-half system ($I = \frac{1}{2}$), there exists two energy states with $E_{1/2} = -\frac{1}{2}\gamma\hbar B_0$ and $E_{-1/2} = \frac{1}{2}\gamma\hbar B_0$ since m can be $+\frac{1}{2}$ or $-\frac{1}{2}$. The eigenvectors of $\widehat{H}$ corresponding to the two energy states can be written using bra-ket notation in the form of $|I, m\rangle$:

$$|\alpha\rangle = \left|\frac{1}{2}, \frac{1}{2}\right\rangle \ and \ |\beta\rangle = \left|\frac{1}{2}, -\frac{1}{2}\right\rangle \tag{C.3}$$

In general, the nuclear spin state is represented by a superposition of the eigenvectors, and thus the wavefunction characterizing the nuclear spin state is given in a linear combination of the eigenvectors. For $I = \frac{1}{2}$,

$$|\psi\rangle = c_a|\alpha\rangle + c_\beta|\beta\rangle \tag{C.4}$$

where c_α and c_β are normalization constants satisfying $|c_a|^2 + |c_\beta|^2 = 1$. These constants are related to how much the corresponding eigenvectors contribute to the total wavefunction.

In NMR experiments, radio frequency pulses are applied to the spin system, perturbing the quantum state in a time-dependent manner. Thus, the time evolution of the wavefunction $|\psi\rangle$ changes according to the time-dependent Schrödinger equation:

$$\frac{\partial|\psi(t)\rangle}{\partial t} = -\frac{i}{\hbar}\widehat{H}|\psi(t)\rangle \tag{C.5}$$

A general solution to this equation is given by

$$|\psi(t)\rangle = \sum_{m=-I}^{I} c_m \, e^{-\frac{iE_m t}{\hbar}} |I, m\rangle \tag{C.6}$$

where c_m is a normalization constant. Given the wavefunction, it is possible to calculate the expectation value of an operator, the expected average value of the results obtained from a large number of measurements of the observable. For example, the expectation value of the x-component of magnetic moment $\langle \hat{\mu}_x(t)\rangle$ can be obtained as

$$\langle \hat{\mu}_x(t)\rangle = \langle \psi(t)|\hat{\mu}_x|\psi(t)\rangle$$

$$= \gamma \sum_{m} \sum_{m'} c_{m'}^* \, c_m \, \langle I, m'|\hat{I}_x|I, m\rangle e^{-i(E_m - E_{m'})t/\hbar} \tag{C.7}$$

The term $\langle I, m'|\hat{I}_x|I, m\rangle$ in Equation (D.7) survives when $m' = m \pm 1$ by the definition of $\hat{I}_x$ expressed in ladder operators. Under this condition, the exponential function of $\langle \hat{\mu}_x(t)\rangle$ becomes $e^{\pm i\Delta E t/\hbar}$, which is equivalent to $e^{\pm i\omega_0 t}$ since $\Delta E = -\gamma\hbar B_0 = \hbar\omega_0$. It indicates that the transverse components of $\boldsymbol{\mu}$ (both x and y components) oscillate at an angular frequency ω_0, known as the Larmor frequency, in the presence of the magnetic field. The oscillating magnetic moment in the transverse plane induces a current in an NMR coil, giving rise to an NMR signal.

For evaluating the expectation value in a bulk sample containing a large number of spins, it is convenient to introduce the density matrix formalism and treat the system as a statistical ensemble. The complete quantum state of the bulk system can be described by a statistical mixture of spin states $(\psi_1, \psi_2, \dots, \psi_n)$ weighted with a probability p_k of a spin occupying a spin state ψ_k ($\sum_{k=1}^{n} p_k = 1$). The wavefunction ψ_k is considered as a linear

superposition of eigenvectors $|I, m\rangle$, such as the one shown in Equation (C.4). Then, the equation for the expectation value of an operator $\hat{O}$ for the macroscopic system is expressed by

$$\langle \hat{O} \rangle = \sum_{k=1}^{n} p_k \langle \psi_k | \hat{O} | \psi_k \rangle = \sum_{k=1}^{n} p_k \, Tr[|\psi_k\rangle\langle\psi_k|\hat{O}] = Tr[\hat{\rho}\hat{O}] \qquad (C.8)$$

where $\hat{\rho}$ is the density operator, representing the probability distribution of the spin states in the system, defined as

$$\hat{\rho} = \sum_{k=1}^{n} p_k \, |\psi_k\rangle\langle\psi_k| \qquad (C.9)$$

and Tr is a trace operator. Each element $\rho_{mm'}$ in a density matrix, a matrix representation of the density operator, has physical meaning. Diagonal elements ($m = m'$) represent the probabilities of finding a system in the eigenvector $|I, m\rangle$, determining the relative populations of different eigenstates. Off-diagonal elements ($m \neq m'$) describe coherence superposition between two different states, which generates transverse magnetization. Thus, with knowledge of the density matrix, it is possible to describe the quantum state of the system at any particular point in the NMR measurements. The equation for the time evolution of the density matrix is given by

$$\frac{\partial \hat{\rho}(t)}{\partial t} = -\frac{i}{\hbar}[\hat{H}(t), \hat{\rho}(t)] \qquad (C.10)$$

This equation is known as Liouville-Von Neumann equation. When $\hat{H}(t)$ is time-independent, the solution for $\hat{\rho}(t)$ is $e^{-i\hat{H}t/\hbar}\hat{\rho}(0)e^{i\hat{H}t/\hbar}$.

The density matrix formalism can describe the NMR phenomena arising from both non-interacting and coupled spins in a macroscopic sample, and the expectation values

can be predicted correctly. For the case of non-interacting spins, semiclassical mechanics can be used to illustrate the motions of spin magnetization using a vector model. The semiclassical treatment provides a visual picture of how the magnetization evolves, but its application is only limited to the system where the spins are independent and the Hamiltonian includes only the Zeeman interaction. In the following sections, a semiclassical model is adopted to illustrate the behaviors of non-interacting spins such as free precession and chemical exchange.

C.2. Semiclassical treatment of NMR

When the magnetic field $\vec{B}$ is applied, individual, non-interacting spins in an ensemble start to align with the direction of the magnetic field from a randomly oriented state. This alignment occurs due to a torque exerted on the magnetic moment by the magnetic field. The magnetization vector $\vec{M}$, equal to a vector sum of all magnetic moments, develops. Equation (C.11) can describe this phenomenon:

$$\frac{d\vec{M}}{dt} = -\gamma \vec{M} \times \vec{B} \tag{C.11}$$

This equation also indicates that $\vec{M}$ will precess about the field direction since

$$\frac{dM_x}{dt} = -\gamma M_y \times \vec{B} = \omega_0 M_y \tag{C.12}$$

$$\frac{dM_y}{dt} = -\gamma M_x \times \vec{B} = -\omega_0 M_x \tag{C.13}$$

resulting in the oscillating transverse magnetization vector at the precession frequency ω_0.

For a spin one-half system, the spins align parallel or anti-parallel to the z-axis of the applied field. Two spin relaxation processes are also involved in bringing the spins

into thermal equilibrium. The spin-lattice relaxation restores longitudinal magnetization while the transverse or spin-spin relaxation fans out the transverse magnetization. By incorporating terms for the relaxation processes into Equation (C.11), the evolution of magnetization vector $\vec{M}$ can be obtained:

$$\frac{d\vec{M}}{dt} = -\gamma\vec{M} \times \vec{B} - \frac{M_x\hat{x} + M_y\hat{y}}{T_2} - \frac{(M_z - M_0)\hat{z}}{T_1} \tag{C.14}$$

where M_x, M_y and M_z are x, y, and z components of $\vec{M}$, respectively. M_0 is the z magnetization at equilibrium. T_1 and T_2 are the spin-lattice and transverse relaxation time constants, respectively. $\hat{x}$, $\hat{y}$, and $\hat{z}$ are the unit vectors in the x, y, and z directions, respectively. This equation is known as the Bloch equation.[1] In a rotating frame of reference at a frequency of ω and when a radio-frequency field $B_1 = \omega_1/\gamma$ is applied along the x-axis of the rotating frame, the Bloch equation can be transformed into:

$$\frac{d}{dt}\begin{bmatrix} M_x \\ M_y \\ M_z \end{bmatrix} = \begin{bmatrix} -1/T_2 & \omega_0 - \omega & 0 \\ -(\omega_0 - \omega) & -1/T_2 & \omega_1 \\ 0 & -\omega_1 & -1/T_1 \end{bmatrix}\begin{bmatrix} M_x \\ M_y \\ M_z \end{bmatrix} + \begin{bmatrix} 0 \\ 0 \\ M_0/T_1 \end{bmatrix} \tag{C.15}$$

When the radio-frequency field is turned off $(\omega_1 = 0)$, the solutions of the above differential equations are:

$$M_x(t) = M_0 e^{-t/T_2} \sin(\Omega t) \tag{C.16}$$

$$M_y(t) = M_0 e^{-t/T_2} \cos(\Omega t) \tag{C.17}$$

$$M_z(t) = M_0 + e^{-t/T_1}[M_z(0) - M_0] \tag{C.18}$$

where $\Omega = \omega_0 - \omega$. Time evolution of the transverse magnetization can be expressed as a complex magnetization $M_+(t) \equiv M_x + iM_y$:

$$M_+(t) = e^{-(i\Omega + 1/T_2)t} M_+(0) \tag{C.19}$$

C.3. Chemical exchange

When a spin exchanges between two environments that are magnetically inequivalent, it is described that the spin undergoes chemical exchange. The chemical exchange affects the time evolution of the spin magnetization, giving rise to detectable changes in NMR properties such as chemical shift, spin relaxation, and line broadening. By extending the Bloch equations to include kinetic parameters, the effect of the chemical exchange on an NMR signal measured in NMR experiments can be studied. As the simplest case, a first-order reversible reaction between the species A and B can be considered:

$$A \rightleftharpoons B \tag{C.20}$$

where k_1 and k_{-1} are the forward and backward rate constants. The rate equations for the concentrations of A and B can be written as:

$$\frac{d}{dt} \begin{bmatrix} [A] \\ [B] \end{bmatrix} = \begin{bmatrix} -k_1 & k_{-1} \\ k_1 & -k_{-1} \end{bmatrix} \begin{bmatrix} [A] \\ [B] \end{bmatrix} \tag{C.21}$$

The concentration parameters are equivalent to the net magnetizations, and thus the above matrix can be combined with the Bloch equations. We can consider that a 90° pulse is applied to the spin system, resulting in the net magnetizations in the transverse plane. The modified Bloch equations can then be written as:

$$\frac{d}{dt} \begin{bmatrix} M_{A+} \\ M_{B+} \end{bmatrix} = \left\{ \begin{bmatrix} -i\Omega_A - R_{2,A} & 0 \\ 0 & -i\Omega_B - R_{2,B} \end{bmatrix} + \begin{bmatrix} -k_1 & k_{-1} \\ k_1 & -k_{-1} \end{bmatrix} \right\} \begin{bmatrix} M_{A+} \\ M_{B+} \end{bmatrix} \tag{C.22}$$

where M_{A+} and M_{B+} are the transverse magnetizations for the species A and B, respectively. The precession frequency and transverse relaxation rate for A and B are denoted as Ω_x and $R_{2,x}$ (x = A or B). These equations are called the Bloch-McConnell equations. A complete set of solutions to Equations (C.22) can be found in ref 2.

An appearance of the NMR signal in a Fourier transformed spectrum is typically determined by a relative magnitude of the kinetic rate constant and the frequency difference between the two sites. One of the two extreme cases is *slow exchange* where the kinetic rate or exchange rate ($k_{ex} = k_1 + k_{-1}$) is slow compared to $\Omega_A - \Omega_B$. In this case, the solution to the total transverse magnetization $M_+ = M_{A+} + M_{B+}$ is:

$$M_+(t) = M_{A+}(0)e^{-(i\Omega_A+R_{2,A}+k_1)t} + M_{B+}(0)e^{-(\Omega_B+R_{2,B}+k_{-1})t} \qquad (C.23)$$

This equation indicates that two NMR signals appear separately at frequencies of Ω_A and Ω_B for A and B states with line broadening determined by $R_{2,A} + k_1$ and $R_{2,B} + k_{-1}$, respectively. The other extreme case is *fast exchange* where $|\Omega_A - \Omega_B| \ll k_{ex}$. Assuming fast exchange approximation, Equations (C.22) can be solved to obtain:

$$M_+(t) = M_+(0)e^{-(i\bar{\Omega}+\bar{R_2}+p_Ap_B(\Omega_A-\Omega_B)^2/k_{ex})t} \qquad (C.24)$$

Here, $\bar{\Omega} = p_A\Omega_A + p_B\Omega_B$ and $\bar{R_2} = p_AR_{2,A} + p_BR_{2B}$ where p_A and p_B are the population fractions of species A and B, respectively. The equation describes that in the fast exchange regime a single resonance is observed at the population-weighted average of the two chemical shifts. Also, the line broadening is governed by $\bar{R_2} + p_Ap_B(\Omega_A - \Omega_B)^2/k_{ex}$. By Fourier transforming $M_+(t)$, the NMR spectrum can be obtained:

$$M_+(\omega) = \int_0^\infty e^{-i\omega t} M_+(t) \, dt. \tag{C.25}$$

The absorption spectrum can be found by taking the real part of $M_+(\omega)$ under assumptions that $k_1 \gg R_{2,A}$ and $k_2 \gg R_{2,B}$:[3]

$$A(\omega) = \frac{p_A p_B (\Omega_A - \Omega_B)^2 k_{ex}}{(\Omega_A - \omega)^2 (\Omega_B - \omega)^2 + (\bar{\Omega} - \omega)^2 k_{ex}^2} M_0, \tag{C.26}$$

where M_0 is the equilibrium magnetization vector immediately after a 90° pulse. Using Equation (C.25), the NMR spectra can be calculated for a spin undergoing a two-site chemical exchange in different exchange regimes as shown in Figure C.1.
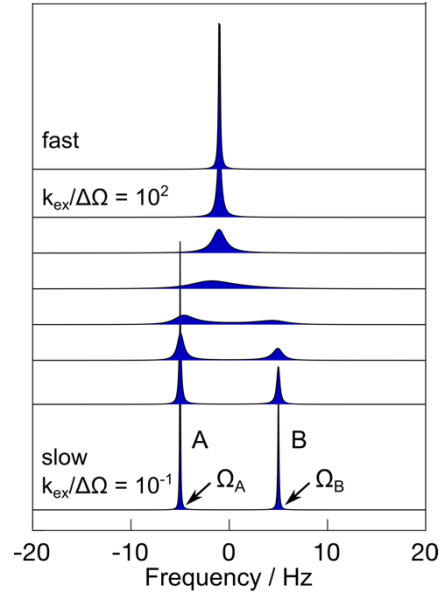

Figure C.1: NMR spectra calculated for a two-site exchange system using Equation (C.26). From bottom to top, k_{ex} varied from 10^{-1} to $10^{-0.5}$, 10^0, $10^{0.5}$, 10^1, $10^{1.5}$, 10^2, and $10^{2.5}$ s^{-1}. Other parameters involved in calculations are $\Omega_A = -15$ Hz, $\Omega_B = 15$ Hz, $p_A = 0.6$, and $p_B = 0.4$.
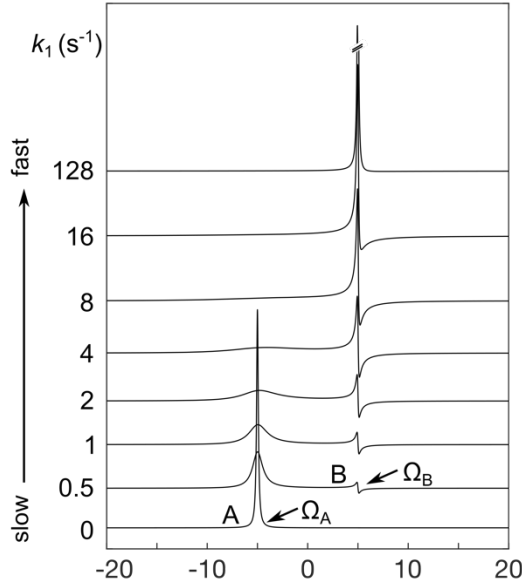
Figure C.2: NMR spectra calculated for a first-order irreversible reaction. From bottom to top, k_1 varied as indicated on the vertical axis. Other parameters involved in calculations are $\Omega_A = -15$ Hz, $\Omega_B = 15$ Hz, $R_{2,A} = R_{2,B} = 0.1$ s^{-1}, $M_{A+}(0) = 1$, and $M_{B+}(0) = 0$.

In nonequilibrium systems, such as an ongoing chemical reaction, the concentrations of species in sites A and B are time-dependent. Changes in the concentrations over the time course of signal evolution will affect the appearance of NMR signals. The signal at the site A will gain line broadening due to a limited lifetime of the species A, and a phase of the signal at the site B will be distorted due to a delayed appearance of the signal. These effects can be seen from a first-order irreversible reaction, neglecting the backward reaction in Equation (C.20). The solutions to the transverse magnetization of species A and B can be obtained from Equations (C.22) assuming $k_{-1} = 0$:[4]

$$M_{A+}(t) = M_{A+}(0)e^{-(i\Omega_A + R_{2,A} + k_1)t} \qquad (C.27)$$

$$M_{B+}(t) = M_{B+}(0)e^{-(i\Omega_B + R_{2,A})t}$$

$$+ M_{A+}(0)\frac{k_1}{i(\Omega_B - \Omega_A) + R_{2,A} - R_{2,B} + k_1} \tag{C.28}$$

$$\times \left[-e^{-(i\Omega_A + R_{2,A} + k_1)t} + e^{-(i\Omega_B + R_{2,B})t} \right]$$

A series of NMR spectra are obtained at several different k_1 values after Fourier transforming $M_+(t) = M_{A+}(t) + M_{B+}(t)$ as shown in Figure C.2. With an increasing k_1, the signal A becomes weaker and broader while the signal B becomes stronger and phase distorted.

C.4. References

(1)   Bloch, F. Nuclear Induction. *Phys. Rev.* **1946**, *70* (7–8), 460–474.

(2)   *Protein NMR Spectroscopy: Principles and Practice*, 2nd ed.; Cavanagh, J., Ed.; Academic Press: Amsterdam ; Boston, 2007.

(3)   Ven, F. J. M. van de. *Multidimensional NMR in Liquids: Basic Principles and Experimental Methods*; VCH: New York, 1995.

(4)   Kühne, R. O.; Schaffhauser, T.; Wokaun, A.; Ernst, R. R. Study of Transient Chemical Reactions by NMR. Fast Stopped-Flow Fourier Transform Experiments. *J. Magn. Reson. (1969)* **1979**, *35* (1), 39–67.